Transport in turbulent plasmas at the interface between different levels of description

by

Leopoldo Carbajal Gomez

Thesis

Submitted to the University of Warwick

for the degree of

Doctor of Philosophy

Physics

March 2015

THE UNIVERSITY OF
WARWICK

To my wife, my driver and inspiration.

Contents

Acknowledgments

Declarations

I declare that the work presented in this thesis is my own original work, unless otherwise indicated, and has not been submitted, partially or entirely, for the attainment of a degree in this or other academic institution. All the work presented here was carried out during the period from October 2012 to March 2015 under the supervision of Prof. Richard O. Dendy and Prof. Sandra C. Chapman.

Some parts of this work has been published or await to be published as indicated below:

Chapter 3

> **L. Carbajal**, R. O. Dendy, S. C. Chapman, and J. W. S. Cook. Linear and nonlinear physics of the magnetoacoustic cyclotron instability of fusion-born ions in relation to ion cyclotron emission. *Physics of Plasmas*, **21**(1):012106, 2014.

> K. G. McClements, R. O. Dendy, **L. Carbajal**, S. C. Chapman, J. W. S. Cook, R. D'Inca, R. W. Harvey, W. W. Heidbrink, and S. D Pinches. Fast particle-driven ion cyclotron emission (ICE) in tokamak plasmas and the case for an ICE diagnostic in ITER. *25th IAEA Fusion Energy Conference*, (TH/P3-28), 2014.

> K. G. McClements, R. D'Inca, R. O. Dendy, **L. Carbajal**, S. C. Chapman, J. W. S. Cook, R. W. Harvey, W. W. Heidbrink, and S. D. Pinches. Fast particle-driven ion cyclotron emission (ICE) in tokamak plasmas and the case for an ICE diagnostic in ITER. *Nuclear Fusion*, **55**:043013, 2015.

Chapter 4

L. Carbajal, S. C. Chapman, R. O. Dendy, N. W. Watkins, and J. W. S. Cook. Hybrid Simulations of Preferential Ion Heating Due to Intermittent Magnetic Fields in the Solar Wind. *Astrophysical Journal*, 2015. Submitted.

J. Rae and I. McCrea, Autumn MIST 2014. *Astronomy and Geophysics*, **56**(1):1, 2015.

<div align="right">

Leopoldo Carbajal Gomez

April 2015

</div>

Abstract

Energetic ion dynamics play an important role in magnetic confinement fusion (MCF) plasmas, as well as in the solar wind. In the former case, energetic ions such as neutral beam injection (NBI) ions and fusion-born alpha-particles, can interact with global modes in tokamak plasmas leading to instabilities that might result in loss of confinement and energy. In the latter case, ion dynamics must be taken into account in order to explain *in situ* and remote observations of heating of the solar wind, which show the occurrence of anisotropic heating of ions, as well as magnetohydrodynamics turbulence and intermittency all at the same time.

In this thesis we address two scenarios in plasma physics where ion dynamics play a key role modifying the mass and energy transport in the plasma, specifically, ion cyclotron emission (ICE) in MCF plasmas, and preferential ion heating due to intermittent magnetic fields in the solar wind. ICE results from a radiative instability, probably the magnetoacoustic cyclotron instability (MCI), driven by energetic ions in MCF plasmas. Understanding the underlying physics of ICE is important for the exploitation of ICE as a non-perturbative diagnostic for confined and lost alpha-particles in deuterium-tritium (D-T) plasmas in future thermonuclear fusion reactors [McClements et al., Nucl. Fusion, **55**, 043013 (2015); Dendy and McClements, Plasma Phys. Controlled Fusion, **57**, 044002 (2015)]. On the other hand, preferential ion heating in the solar wind, observed as the occurrence of an ion beam which drifts along the background magnetic field with a velocity close to the local Alfvén speed, is still an open problem. Despite the large amount of studies conducted in this issue, none of them included intermittency self-consistently. Therefore, the relationships between preferential ion heating and intermittency have remained unknown, until now.

We study in detail the previously mentioned scenarios through numerical simulations using the hybrid approximation for the plasma, which treat ions as kinetic particles and electrons as a neutralizing massless fluid. Our hybrid simulations of the MCI confirm predictions of the analytical theory of the MCI, and recover some features of ICE as observed in D-T plasmas in JET. Furthermore, by going deep into the nonlinear stage of the MCI, we recover additional features of ICE which are not predicted by the linear theory of the MCI but are present in the measured ICE signal, resulting in a good match between our simulation results and the measured ICE intensity in JET. On the other hand, we present the first study of preferential ion heating in the fast solar wind including intermittent electromagnetic fields in a self-consistent way. We find that the temporal and spatial dynamics of the mechanisms driving preferential ion heating in our simulations (gyrobunching and ion trapping by the electric field), the ion temperature anisotropy $T_\perp/T_\parallel$ (perpendicular temperature/parallel temperature), and the degree of correlation between velocity and magnetic field fluctuations, show strong dependence on the level of intermittency in the electromagnetic fields.

Abbreviations

AC	Alfvén Cascade
AU	Astronomical Units
CFL	Courant-Friedrichs-Lewy
D-T	Deuterium-Tritium
EICBAI	Electromagnetic Ion Cyclotron Beam Anisotropy Instability
FDL	Finite Difference Leapfrog
HPC	High Performance Computing
ICE	Ion Cyclotron Emission
ICRH	Ion Cyclotron Resonant Heating
LIM	Local Intermittency Measure
MCF	Magnetic Confinement Fusion
MCI	Magnetoacoustic Cyclotron Instability
MHD	Magnetohydrodynamics
MPI	Message Passing Interface
NBI	Neutral Beam Injection
OpenMP	Open Multi-Processing
PIC	Particle-In-Cell
PTE	Preliminary Tritium Experiment
PDF	Probability Distribution Function
REIII	Resonant Electromagnetic Ion-Ion Instability
SF	Structure Functions

TAEs Toroidal Alfvén Eigenmodes

TTCMP Transit Time Compressional Magnetic Pumping

TSC Triangular Shape Cloud

Chapter 1

Introduction

Plasma, the so-called fourth state of matter, is a system that consist of interpenetrating populations of positive ions and electrons, and is charge neutral as a whole. In a plasma, the kinetic energy of collisions exceed binding energy of electrons to nuclei. Unlike liquids and solids where the interactions between atoms are short-ranged, that is, atoms only interact with their nearest neighboring atoms; in plasmas there are large-range interactions which allow charged particles to interact with the entire plasma through electromagnetic fields. The plasma is very sensitive to external perturbations, i.e. to external electric and magnetic fields, and to changes in its parameters such as number density and temperature. As a result of these perturbations, the plasma exhibits complex behavior and collective phenomena such as oscillations and the generation of coherent structures in physical space, and under certain conditions the plasma can become unstable leading to the generation of exponentially growing electromagnetic fields that significantly modify the transport of mass and energy within the plasma.

These rich and complex dynamics of the plasma can be studied using different levels of description, which include different levels of detail in their description of the plasma. These levels of description for the plasma are presented and compared in Sec. 1.1. Then, we introduce the hybrid approximation for the plasma in Sec. 1.2, the level of description for the plasma that we use in our studies of energetic ion effects on fusion and solar-wind plasmas. Finally, in Secs. 1.3.1 and 1.4.3 we introduce some scenarios relevant to fusion plasmas of the JET tokamak experiment and to solar-wind plasmas where energetic ions play an important role modifying the whole plasma dynamics.

1.1 Levels of description for the plasma

In general, the plasma dynamics can be described using different levels of detail, depending on the temporal and spatial scales at which the phenomena under study occurs. For example, we might use a level of description for the plasma that take into account the dynamics of individual charged particles constituting the plasma when studying plasma oscillations in a vacuum tube in the laboratory with characteristic time scales up to a few milliseconds, or we might use a level of description for the plasma that treats the whole plasma as a magnetised fluid when studying plasma phenomena occurring at spatial scales as large as the solar system and temporal scales ranging from hours to days. Here, the former level of description for the plasma is known as the kinetic theory for plasmas, and the latter is know as the ideal magnetohydrodynamics (MHD) theory for plasmas. These two theories are the two extreme levels of description of the plasma used nowadays. In the kinetic theory for plasmas the dynamics of charged particles are governed by the Lorentz force

$$\frac{d\boldsymbol{x}_l}{dt} = \boldsymbol{v}_l\,, \tag{1.1}$$

$$m_l \frac{d\boldsymbol{v}_l}{dt} = eZ_l\left(\boldsymbol{E} + \boldsymbol{v}_l \times \boldsymbol{B}\right)\,, \tag{1.2}$$

where $\boldsymbol{x}_l$ and $\boldsymbol{v}_l$ are the position and velocity of trajectories of each charged particle of species l, which can be electrons or ions, m_l and Z_l are their corresponding mass and atomic number, e is the magnitude of the electron charge, and $\boldsymbol{E}$ and $\boldsymbol{B}$ are the vector electric and magnetic fields, respectively. In this theory, the electromagnetic fields are evolved self-consistently through the complete set of Maxwell's equations:

$$\nabla \cdot \boldsymbol{E} = \frac{\sigma}{\epsilon_0}, \tag{1.3}$$

$$\nabla \cdot \boldsymbol{B} = 0, \tag{1.4}$$

$$\nabla \times \boldsymbol{E} = -\frac{\partial \boldsymbol{B}}{\partial t}, \tag{1.5}$$

$$\nabla \times \boldsymbol{B} = \mu_0 \left(\boldsymbol{J} + \epsilon_0 \frac{\partial \boldsymbol{E}}{\partial t}\right), \tag{1.6}$$

where σ is the total charge density, $\boldsymbol{J}$ is the total current density vector, and ϵ_0 and μ_0 are the vacuum electric permittivity and magnetic permeability, respectively.

Solving the Eqs. (1.1) and (1.2) is equivalent to solve a continuity equation in

phase space, the so-called Vlasov equation, of the probability distribution function $f_l(\boldsymbol{x}, \boldsymbol{v}, t)$ for each plasma species l,

$$\frac{\partial f_l}{\partial t} + \boldsymbol{v} \cdot \nabla_x f_l + q_l \left(\boldsymbol{E} + \boldsymbol{v} \times \boldsymbol{B} \right) \cdot \nabla_v f_l = 0, \tag{1.7}$$

where the subindex l can refer to either electrons (e), or some ion species (j), q_l is the electric charge of species l; $q_e = -e$ for electrons, and $q_j = eZ_j$ for ion species j. In addition, $\nabla_x = \boldsymbol{x}\frac{\partial}{\partial x} + \boldsymbol{y}\frac{\partial}{\partial y} + \boldsymbol{z}\frac{\partial}{\partial z}$ is the Cartesian gradient operator in physical space, and $\nabla_v = \boldsymbol{v}_x\frac{\partial}{\partial v_x} + \boldsymbol{v}_y\frac{\partial}{\partial v_y} + \boldsymbol{v}_z\frac{\partial}{\partial v_z}$ is the gradient operator in velocity space. Eq. (1.7), together with Eqs. (1.3) to (1.6) are called the Vlasov-Maxwell equations, and represent an alternative formulation of the kinetic theory of the plasma that can be used to introduce the equations of the MHD theory for plasmas.

The ideal MHD theory describes the plasma as a magnetised single fluid whose dynamics are given by a set of equations derived from the Vlasov equations for electrons and ions. In this level of description it is assumed that the plasma is quasi-neutral, that is, the electric charge density $\sigma_e = -en_e$ is everywhere equal in magnitude to the ion charge density $\sigma_i = \sum_{j=1}^{N} eZ_j n_j$. Here the sum is over the N different ion species present in the plasma. The equations of the MHD theory establish relations between the first three statistical moments of the electron and ion distribution functions: the number density n_l, the bulk velocity $\boldsymbol{u}_l$, and the pressure rank-2 tensor $\hat{P}_l$, which are defined as:

$$n_l(\boldsymbol{x}, t) = \int f_l(\boldsymbol{x}, \boldsymbol{v}, t) d^3 v, \tag{1.8}$$

$$\boldsymbol{u}_l(\boldsymbol{x}, t) = \frac{1}{n_l(\boldsymbol{x}, t)} \int \boldsymbol{v} f_l(\boldsymbol{x}, \boldsymbol{v}, t) d^3 v, \tag{1.9}$$

$$\hat{P}_l(\boldsymbol{x}, t) = m_l \int (\boldsymbol{v} - \boldsymbol{U}_m)(\boldsymbol{v} - \boldsymbol{U}_m) f_l(\boldsymbol{x}, \boldsymbol{v}, t) d^3 v, \tag{1.10}$$

where the subindex l refers to either electrons, or any ion species, m_l is the mass of species l, and $\boldsymbol{U}_m$ is the plasma mass flow velocity defined as:

$$\rho_m \boldsymbol{U}_m = m_e n_e \boldsymbol{u}_e + \sum_{j=1}^{N} m_j n_j \boldsymbol{u}_j, \tag{1.11}$$

where $\rho_m = m_e n_e + \sum_{j=1}^{N} m_j n_j$ is the plasma mass density. In order to calculate the MHD equations for the plasma we first integrate Eq. (1.7) over the entire velocity space to obtain a continuity equation for electrons and each ion species

$$\frac{\partial n_l}{\partial t} + \nabla_x \cdot (n_l \boldsymbol{u}_l) = 0. \tag{1.12}$$

Next, we multiply each continuity equation by m_l and sum over electrons and all ions species to obtain the mass continuity equation for the plasma:

$$\frac{\partial \rho_m}{\partial t} + \nabla_x \cdot (\rho_m \boldsymbol{U}_m) = 0. \tag{1.13}$$

If we instead multiply Eq. (1.12) by the electric charge $q_l = eZ_l$, $q_e = -e$ for electrons, and sum the resulting equation of ions to that of electrons, we obtain the electric charge continuity equation, also known as the current conservation equation, for the case when there are no sources or sinks of electric charge. Using the quasi-neutrality condition for the plasma $\sigma_e + \sigma_i = 0$, where $\sigma_i = \sum_{j=1}^{N} q_j n_j$, this equation becomes

$$\nabla \cdot \boldsymbol{J} = 0, \tag{1.14}$$

where $\boldsymbol{J} = en \left(U_i - u_e \right)$ is the total current density, n refers to the total number density:

$$n \equiv n_e = \sum_{j=1}^{N} Z_j n_j \,, \tag{1.15}$$

and we have defined the total ion's bulk velocity $\boldsymbol{U}_i$ as:

$$\boldsymbol{U}_i = \frac{\sum_{j=1}^{N} \left(Z_j n_j \boldsymbol{u}_j \right)}{\sum_{j=1}^{N} \left(Z_j n_j \right)} \,. \tag{1.16}$$

To obtain the second MHD equation of the plasma, the plasma momentum equation, first we multiply the Vlasov equation by $m_l \boldsymbol{v}_l$ and integrate it over the entire velocity space. The resulting momentum equation for electrons and ions is:

$$\frac{\partial \left(m_l n_l \boldsymbol{u}_l \right)}{\partial t} + \nabla_x \cdot \hat{P}_l + \nabla_x \cdot \left(m_l n_l \boldsymbol{U}_m \boldsymbol{U}_m \right) - \sigma_l \left(\boldsymbol{E} + \boldsymbol{u}_l \times \boldsymbol{B} \right) = 0, \tag{1.17}$$

where $\hat{P}_l$ is the pressure tensor of species l defined in Eq. (1.10). After substituting Eq. (1.12) into Eq. (1.17), we sum all the resulting equations for the different plasma species l, and rearrange the terms in order to obtain the following momentum equation for the plasma:

$$\rho_m \left(\frac{\partial \boldsymbol{U}_m}{\partial t} + \boldsymbol{U}_m \cdot \nabla_x \boldsymbol{U}_m \right) = -\nabla \cdot \hat{P} + \boldsymbol{J} \times \boldsymbol{B}, \tag{1.18}$$

where $\hat{P} = \hat{P}_e + \hat{P}_i$ is the total plasma pressure. In the ideal MHD theory it is assumed that the electrons have plenty of time to follow the ion dynamics and reach thermal equilibrium. This assumption is equivalent to neglecting electron inertial effects, that is, the first term of Eq. (1.17) for electrons becomes zero. Substituting Eq. (1.12) into this equation and rearranging terms we obtain the following generalised Ohm's law:

$$\boldsymbol{E} = -\boldsymbol{u}_e \times \boldsymbol{B} - \frac{1}{en} \nabla_x \cdot \hat{P}_e. \tag{1.19}$$

Substituting $\boldsymbol{u}_e$ in terms of the total current density $\boldsymbol{J}$ and the total ion bulk velocity $\boldsymbol{U}_i$ into Eq. (1.19), along with Ampere's Law in its Darwin limit ($\partial \boldsymbol{E}/\partial t \to 0$), we obtain the following form of the generalised Ohm's law:

$$\boldsymbol{E} = \frac{1}{\mu_0 en}(\nabla_x \times \boldsymbol{B}) \times \boldsymbol{B} - \boldsymbol{U}_i \times \boldsymbol{B} - \frac{1}{en}\nabla_x \hat{P}_e. \tag{1.20}$$

Generally, it is assumed that the plasma pressure $\hat{P}$ in Eq. (1.18) is isotropic, that is, the pressure tensor becomes a scalar pressure P, which obeys an equation of state. The two common models for the plasma pressure P are the adiabatic law

$$\frac{\mathrm{d}}{\mathrm{d}t} \left(\frac{P}{\rho_m^\gamma} \right) = 0, \tag{1.21}$$

and the isothermal law

$$P = n\left(T_e + T_i\right), \tag{1.22}$$

where $\gamma = (2 + \mathcal{N})/\mathcal{N}$, with $\mathcal{N}$ being the number of degrees of freedom of the plasma, and T_e and T_i are the constant electron and ion temperatures.

In this way, the ideal MHD theory for plasmas is defined by the set of Eqs. (1.13), (1.14), (1.18), (1.20) and (1.5), along with an equation of state for the plasma pressure, which might be either Eq. (1.21), or Eq. (1.22). At this point it is important to note that, contrary to the kinetic theory, in the MHD approximation for the plasma all the detailed information of the distribution of electrons and ions in velocity space is lost.

So far, we have presented two extremes in levels of description for the plasma, namely, the kinetic theory and the ideal MHD theory. As expected, there are other levels of description of the plasma in-between these two, each including different

levels of detail for describing the dynamics of the plasma. Among the existing levels of description typically used to study fusion and solar-wind plasmas are:

Kinetic theory

This level of description is well suited for studying plasma phenomena occurring at time scales comparable to and below the electron gyro-period, and spatial scales where charge separation plays a key role in the plasma dynamics. This theory evolves the full electron and ion probability distribution function $f(\boldsymbol{x}, \boldsymbol{v}, t)$, together with the full set of Maxwell's equations.

Gyrokinetic theory

This level of description for the plasma is well suited for studying strongly magnetised plasmas where the relevant time scales are larger than the electron and ion gyro-period, and the spatial scales of the small fluctuations of the plasma parameters are comparable to the electron and ion gyro-radius, but much smaller than the size of the plasma or the variation length-scale of the equilibrium plasma parameters such as the background magnetic field and the number density of the bulk plasma in a magnetically confined fusion plasma, for example. In this theory the electron and ion dynamics are divided into the fast gyro-motion of each plasma species, and their relative slow drift motion along the magnetic field $\boldsymbol{B}$. This allows us to simplify the dynamics of the charged particles forming the plasma to the motion of their gyro-centre in physical space $\boldsymbol{R}$, together with the evolution of the parallel ($v_{\parallel}$) and perpendicular ($v_{\perp}$) components of the gyro-centre velocity with respect to the magnetic field direction [Hatzky et al., 2007; Barnes, 2009]. This theory evolves the full set of Maxwell's equations along with the gyro-centre probability distribution function for each plasma species $f(\boldsymbol{R}, v_{\parallel}, v_{\perp})$.

Hybrid theory (kinetic-fluid)

This level of description for the plasma is used to study plasma phenomena where ions play an important role modifying the entire plasma dynamics. The plasma phenomena that can be studied with the hybrid theory for the plasma must occur at spatial scales comparable to the ion gyro-radius and temporal scales comparable to the ion gyro-period [Winske and Omidi, 1993; Winske et al., 2003]. Quasi-neutrality holds everywhere for this theory. The hybrid theory for the plasma describes the full kinetic dynamics of ions, that is, evolves the full ion probability distribution function $f(\boldsymbol{x}, \boldsymbol{v}, t)$, and treat electrons as a charge-neutralising massless fluid. The electric field is advanced through a

generalised Ohm's law (Eq. (1.20)) and the magnetic field is advanced using Faraday's Law (Eq. (1.5)).

Multi-fluid theory

The multi-fluid theory for the plasma is well suited to study plasmas close to thermodynamic equilibrium where the relevant temporal and spatial scales are larger than the ion gyro-period, and larger than the ion gyro-radius, respectively [Ofman, 2010]. In this level of description, quasi-neutrality holds everywhere, the electrons are treated as a charge-neutralising massless fluid, and each ion species is treated as a different fluid. The electric field is evolved through a generalised Ohm's law and the magnetic field is advanced using Faraday's Law.

Ideal MHD theory

This level of description for the plasma is well suited to study plasma phenomena occurring at time scales well above the ion gyro-period and at spatial scales well above the ion gyro-radius, for example, to study the propagation of the solar wind through the solar system. As described in this section, the ideal MHD theory treats the plasma as a single magnetised fluid, which dynamics is given by a mass continuity equation (Eq. (1.13)), a momentum equation for the plasma (Eq. (1.18)), and an equation of state for the plasma pressure. The electric field is evolved through a generalised Ohm's law and the magnetic field is advanced using Faraday's Law.

Further details to describe the plasma can be included in these theories; for example, in the kinetic theory we might have included collisions between the different plasma species, or we might have included an equation derived from the Vlasov equation for evolving the full plasma pressure tensor $\hat{P}$ in the MHD theory. Finally, it is important to mention that there are other levels of description apart from those mentioned above which, although are not widely used, might be employed to study interesting scenarios in magnetically confined fusion plasmas. These theories are the hybrid gyrokinetic-kinetic theory for the plasma [Lin et al., 2011], which uses gyrokinetic theory for electrons and kinetic theory for ions, and the hybrid gyrokinetic-fluid theory [Mishchenko et al., 2014], which uses gyrokinetic theory for ions while electrons are treated as a fluid.

1.2 The hybrid approximation for the plasma

In this section we further discuss the hybrid approximation for the plasma introduced in Sec. 1.1. This level of description for the plasma is specially well suited for phenomena occurring about and above the ion inertial length and the ion gyro-radius, and with a duration comparable to the ion gyro-period [Winske and Omidi, 1996; Clark et al., 2013b]. This approximation enables us to address evolution of the plasma over longer time scales and larger spatial scales than the kinetic theory for the plasma, and allows the existence of low-frequency kinetic electromagnetic modes such as ion-Bernstein waves, ion-cyclotron waves and Alfvén waves.

The hybrid approximation for the plasma represents the different ion distributions as kinetic particles and the electrons as a charge-neutralising massless fluid. In this approximation the ion dynamics are governed by the Lorentz force, that is, Eqs. (1.1) and (1.2). On the other hand, the fluid electrons are modelled as an isotropic and isothermal ideal gas, $P_e = nT_e$, where n is the total number density given by Eq. (1.15), and T_e is the constant electron temperature. The electric ($\boldsymbol{E}(\boldsymbol{x},t)$) and magnetic ($\boldsymbol{B}(\boldsymbol{x},t)$) fields are linked by the generalized Ohm's law given by Eq. (1.20), and the magnetic field is advanced in time using Faraday's law (Eq. (1.5)).

The hybrid approximation for the plasma has been widely used to study plasma phenomena relevant to space and solar-wind plasmas such as electromagnetic instabilities driven by ion beams [Winske and Leroy, 1984; Mankofsky et al., 1987; Akimoto et al., 1991; Winske and Omidi, 1992], the evolution of quasi-parallel shocks at the earth's bow shock [Thomas et al., 1990], magnetic reconnection [Krauss-Varban and Omidi, 1995; Nakamura and Fujimoto, 1998; Yin and Winske, 2012], the interaction of the solar wind with small comets in high Mach number flows [Hopcroft and Chapman, 2001], and ion heating by Alfvén waves in solar wind [Liewer et al., 2001; Araneda et al., 2009; Matteini et al., 2011; Maneva et al., 2013]. More recently, this approximation has been used to study perpendicular collision-less shocks in laboratory plasmas [Clark et al., 2013a], as well as fusion plasma phenomena such as the formation [Gingell et al., 2014] and evolution [Gingell et al., 2012, 2013] of coherent filamentary structures, the so-called blobs, at the edge of tokamak plasmas, and the occurrence of radiative instabilities driven by fusion-born ions in deuterium-tritium fusion plasmas [Carbajal et al., 2014]. All these studies have shown that the kinetic ion dynamics played an important role in modifying the entire plasma dynamics; therefore, other levels of description that do not treat ions kinetically would be inappropriate. The following sections present some scenarios

in magnetically confined fusion plasmas and in solar wind plasmas where experimental measurements and observations show the occurrence of phenomena in which the kinetic effects of energetic ions play an important role. In Chapters 3 and 4 some of these scenarios are studied through numerical simulations using the hybrid approximation for the plasma.

1.3 Magnetically confined fusion plasmas

Thermonuclear fusion through the use of magnetically confined plasmas, the method of achieving nuclear fusion by confining very hot plasmas ($\sim 10^8$ K or 10 keV) using strong magnetic fields, represents the most promising option to exploit fusion energy in the future to cover the increasing energy demand around the world. Extensive experimental, theoretical and simulation work on this issue has been done during the past half century, which has resulted in the design of three leading concepts for experimental thermonuclear fusion reactors: tokamaks, spheromaks and stellarators. All three concepts share some common features: using the fact that charged particles stream along the magnetic field spiraling around the magnetic field lines, these three concepts use strong magnetic fields to confine the hot plasma; however, the spatial configuration of such fields is different in each case. Also, the shape of their vacuum vessel where the plasma is kept confined by the strong magnetic fields is topologically equivalent to a torus in all cases.

Tokamaks represent the most successful (and studied) concept of a modern thermonuclear fusion reactor. This concept has been thoroughly studied in machines such as DIII-D, JT-60, Tore Supra, ASDEX-Upgrade, TFTR, and the Joint European Torus (JET), which is the largest tokamak in operation nowadays. In Fig. 1.1 we show a schematic representation of the main components of a tokamak: the toroidal vacuum vessel, where the hot plasma (purple) is confined, the toroidal magnetic field coils, which generate the main toroidal magnetic field (green), and the external poloidal magnetic field coils, which generate the poloidal magnetic field (green) used to shape and position the plasma in the vacuum vessel. At the centre of the tokamak are the inner poloidal magnetic field coils which, through transformer action, generate an electric current within the plasma (red arrow) that produces additional poloidal magnetic fields that provide enhanced plasma confinement. The toroidal and poloidal magnetic fields combine and produce a set of nested toroidal surfaces of twisted magnetic field lines (yellow).

Theoretical calculations and experimental observations of the stability properties of tokamak plasmas have shown that by reducing the aspect ratio of a tokamak $A = R/a$, where R and a are the major and minor radius of the toroidal plasma in a tokamak, the stability of the plasma considerably increases. This result has been used in the design of spheromaks such as START, NSTX and MAST spheromaks, also known as spherical tokamaks, which have smaller aspect ratios ($A \sim 1.2$) than typical tokamaks ($A \sim 2.5$). This is achieved by modifying the design of the toroidal magnetic field coils. While in a tokamak, the toroidal magnetic field is produced by
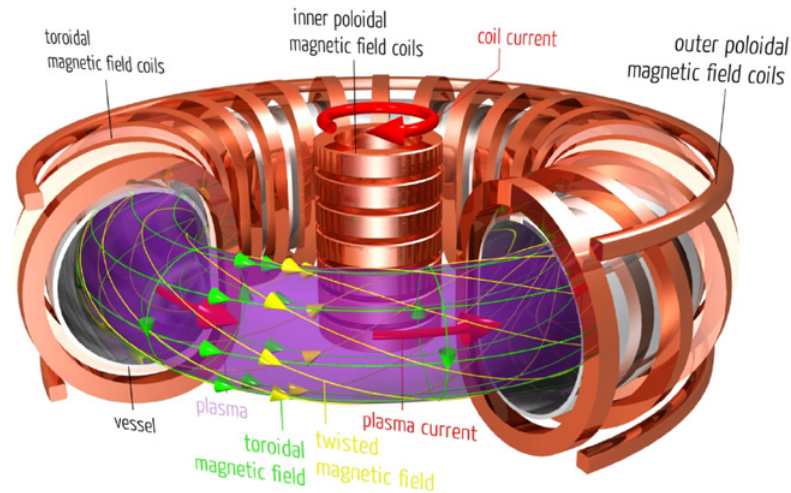
Figure 1.1: Schematic representation of a Tokamak. The very hot plasma (purple) is confined by the twisted magnetic field (yellow) resulting from combining the toroidal and poloidal magnetic fields, which are generated by external coils and the internal plasma current (red arrow), which in turn is generated through transformer action by the inner poloidal magnetic field coils. Source: Public relations department, Max Planck Institute for Plasma Physics.

a series of individual ring-like magnets passing through the hole of the centre of the reactor, in a spheromak the toroidal magnetic field is produced by a set of half-ring shaped magnets connected to a central conductor post passing by the centre of the reactor. This concept for a fusion reactor, though having good stability properties, has not been studied as much as tokamaks.

On the other hand, stellarators are another fusion reactor concept that was invented at the same time than tokamaks. Contrary to tokamaks where the poloidal magnetic field is mainly produced by internal plasma currents induced by external magnetic coils, in a stellarator the poloidal magnetic field is generated by external helical magnetic coils placed around the vacuum vessel. Stellarators such as HSX, Wendelstein 7-X and LHD have shown that this concept of a fusion reactor possesses better plasma stability than tokamaks; however, their three-dimensional nature makes them very complicated to design and model.

Furthermore, the way the plasma is generated varies from device to device, in all cases the plasma must be initially heated by external means, for example, using neutral beam injection (NBI) and external electromagnetic fields; this is necessary to reach optimum temperatures at which fusion reactions start to occur. After this initial stage, the fusion-born ions resulting from these fusion reactions are meant

to provide all the plasma heating needed to achieve self-sustained nuclear burning, the stage at which no external input power is needed to continue operating the reactor. It is planned that the first generation of thermonuclear fusion reactors will operate with a mix of deuterium-tritium as fuel. In this scenario the most probable fusion reaction is that in which nuclei of deuterium and tritium fuse and produce an alpha-particle and a neutron, that is,

$$D + T \rightarrow (3.56 \text{ MeV}) \text{ He}^{++} + (14.03 \text{ MeV}) \ n. \tag{1.23}$$
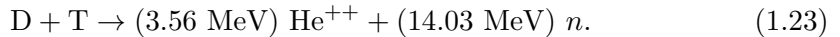
In the following sections we discuss some scenarios where the interaction between the 3.5 MeV fusion-born alpha-particles and the broad range of electromagnetic waves occurring in magnetically confined fusion plasmas might lead to plasma instabilities that not only modify the mass and energy transport in the plasma, but also might be used to diagnose the evolution of the fusion-born alpha-particles distribution in the plasma.

1.3.1 Fusion-born ion effects in magnetically confined fusion plasmas

In the last few years there have been significant advances in the detection and understanding of instabilities driven by energetic ions in magnetically confined fusion plasmas. Most of these instabilities are Alfvénic in nature, and can be roughly classified as: perturbative or frequency locked instabilities, and non-perturbative or frequency sweeping instabilities [Sharapov et al., 2013]. In both cases, the energetic particles excite unstable Alfvén modes through wave-particle interactions. However, in the case of perturbative instabilities the energetic particles determine the exponential growth rate of these unstable modes, but do not significantly affect their properties, which are determined by the bulk plasma. In contrast, for the case of non-perturbed instabilities all the properties of the unstable modes are determined by the energetic particle distribution in phase space, which changes faster than the plasma equilibrium.

Understanding the underlying physics of the frequency locked and frequency sweeping instabilities in magnetically confined thermonuclear plasmas allow us to infer the plasma parameters at which these instabilities occur. This means that these instabilities can be used to diagnose some plasma parameters indirectly. This is done, for example, in deuterium-tritium (D-T) plasmas of TFTR, where specific plasma parameters and distributions of fusion-born alpha-particles are inferred by identifying Alfvén cascade (AC) modes and toroidal Alfvén eigenmodes (TAEs)

[Nazikian et al., 2003]. Fig. 1.2 illustrates examples of spectrograms of the magnetic field in JET (panel a)) and MAST (panel b)). Panel a) shows the occurrence of Alfvén modes in JET, namely, TAEs, excited by frequency locked (perturbative) instabilities driven by ion cyclotron resonant heating (ICRH). Panel b) shows the occurrence of chirping Alfvén modes driven by neutral beam injection (NBI) in MAST. The properties of these latter Alfvén modes, such as their frequency, evolve in time as the NBI energetic ions are rapidly redistributed in phase space. In contrast, the properties of the TAEs in JET change much slower as the equilibrium plasma bulk parameters evolve over time.
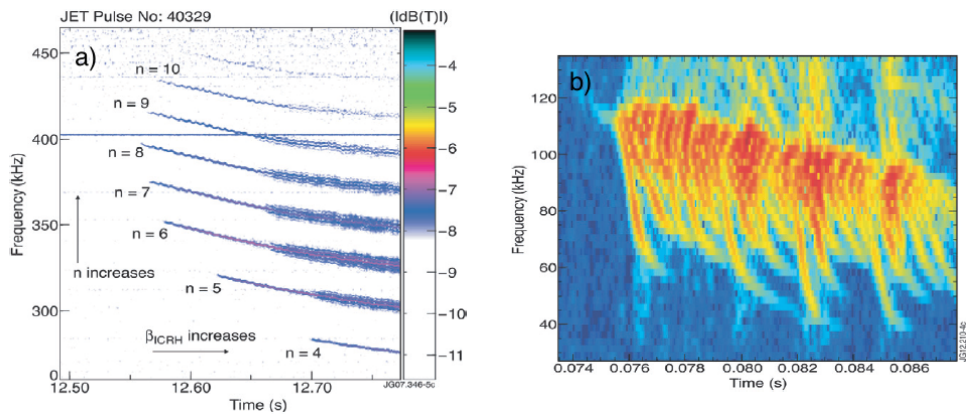
Figure 1.2: Examples of spectrograms of the magnetic field in JET and MAST. Panel a): Spectrogram of the magnetic field in JET discharge #40329 showing (perturbative) ICRH-driven TAEs. Panel b): Spectrogram of the magnetic field in MAST discharge #27177 showing (non-perturbative) chirping Alfvén modes driven by NBI energetic ions. Reproduced from Sharapov et al. [2013].

As previously mentioned, fusion-born alpha-particles will provide all the plasma heating needed to achieve self-sustained nuclear burning in future thermonuclear fusion devices. In Thomas et al. [1998] and Thomas et al. [2001] the authors studied in detail the electron and ion heating driven by fusion-born alpha-particles during the DTE1 campaign of JET in 1997, where different mixtures of D-T were used as sources of the NBI heating system. In these plasmas, instabilities driven by energetic alpha-particles such as TAEs were not present [Thomas et al., 1998], allowing a detailed study of the process of trapping and slowing down of alpha-particles born within the core plasma, only in the presence of MHD instabilities. The observed plasma heating by fusion-born alpha-particles was higher than the theoretical predictions. This surprisingly efficient plasma heating still remains unexplained. Knowledge about the distribution of alpha-particles in phase space might shed some light into the mechanisms driving this heating by alpha-particles.

No diagnostics for alpha-particles were available during this experiment.

Summarising, perturbative and non-perturbative instabilities driven by energetic ions can be used to diagnose bulk plasma parameters and detailed information about the distribution of these energetic ions in phase space. New and more precise diagnostics for this purpose are needed if we want to correctly predict and, at a certain level, control the behaviour of fusion-born alpha-particles in the next generation of thermonuclear fusion reactors. The next section introduces the ion cyclotron emission (ICE), an electromagnetic instability driven by non-thermal distributions of fusion-born alpha-particles in deuterium-tritium plasmas with great potential for being used to diagnose the evolution of the distribution of fusion-born alpha-particles in future fusion reactors [McClements et al., 2015].

1.3.2 The Ion Cyclotron Emission

Fusion-born alpha-particles resulting from thermal D-T fusion (Eq. 1.23), will play a key role in future magnetically confined plasmas. These ions must provide most of the plasma heating required to achieve self-sustained nuclear burning. It is possible that the efficiency of this heating process may be reduced, to some extent, by the occurrence of velocity-space instabilities that take place on fast timescales, which are shorter than the timescale on which the fusion-born particles deliver their energy to the plasma through collisional processes [Heidbrink and Sadler, 1994]. For this reason, it is essential to develop diagnostics to monitor the confinement and evolution of the fusion-born alpha-particles in D-T plasmas of future thermonuclear fusion reactors, such as ITER. As mentioned in Sec. 1.3.1, some instabilities driven by energetic ions might be used to diagnose the plasma and to follow the evolution of the distribution of energetic ions itself, given that there is a theoretical basis that provides interpretation of such instabilities. A potential instability in this category gives rise to the experimentally observed ion cyclotron emission (ICE). This phenomenon involves the emission, from spatially localised regions of tokamak plasmas, of intense suprathermal radiation which is spectrally peaked at sequential ion cyclotron harmonics. This radiation appears to result from a collective instability that is driven by a velocity distribution of energetic ions that approximates to a drifting ring-beam, which can arise naturally, through drift orbit excursions, in the outer edge plasma. ICE was the first collective radiative instability driven by confined fusion-born ions that was observed in tokamak plasmas when Ohmic heating and hydrogen neutral-beam injection (NBI) were used to heat the plasma [Cottrell and Dendy, 1988; Schild et al., 1989]. Figure 1.3 shows the first detections of ICE in pure deuterium JET plasmas.
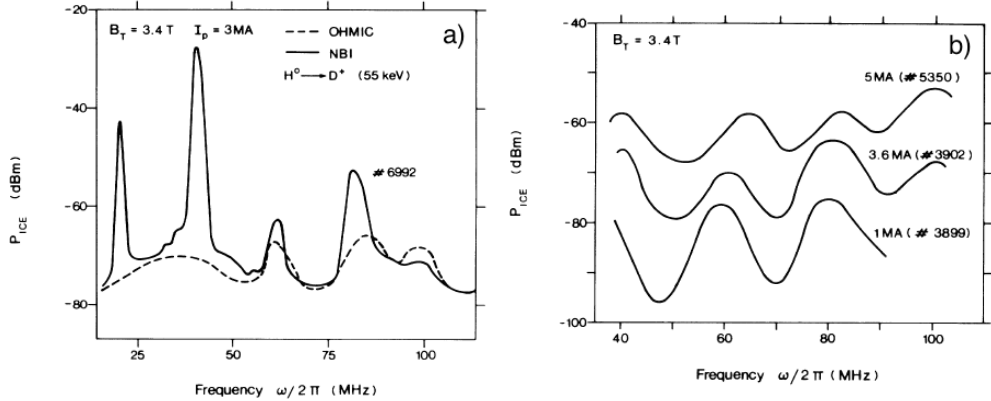
Figure 1.3: First detections of ICE in pure deuterium plasmas in JET. Panel a): ICE power spectrum before (dashed line) and during (solid line) hydrogen NBI injection into a pure deuterium limiter plasma in JET. Panel b): ICE power spectrum from three Ohmical pure deuterium limiter plasmas in JET. Reproduced from Cottrell and Dendy [1988].

ICE was the only instability driven by confined fusion-born alpha-particles that was observed both in JET and TFTR from deuterium-tritium plasmas [Cottrell et al., 1993; Cauffman et al., 1995; Dendy et al., 1995; McClements et al., 1996, 1999]. In these tokamaks, the ICE intensity showed linear scaling with the measured neutron flux and with alpha-particle concentration [Cottrell et al., 1993; Dendy et al., 1995; McClements et al., 1996]. Figure 1.4 shows the scaling of properties of the ICE intensity with neutron flux and alpha-particle concentration for pure deuterium plasmas and D-T plasmas in JET.

During the first studies of ICE in JET, a strong correlation between ICE and MHD activity was observed [Schild et al., 1989; Cottrell et al., 1993]. More recently, ICE has been used in the DIII-D tokamak to diagnose energetic ion loss due to MHD activity [Watson and Heidbrink, 2003; Heidbrink et al., 2011]. This suggests that ICE might be exploited as a complementary diagnostic for MHD activity, as well as for fusion-born alpha-particle dynamics, in future D-T plasmas in JET and ITER [McClements et al., 2014, 2015]. Studies of ICE in the JT-60U [Ichimura et al., 2008; Sato et al., 2010] and ASDEX-Upgrade [D'Inca et al., 2011] tokamaks have extended the understanding of the dependence of ICE on the different plasma parameters and on NBI parameters. Notably, in ASDEX-Upgrade, three different types of ICE have been identified [D'Inca, 2014] :

- Edge ICE, driven by fusion-born ions and ICRH-accelerated ions that reach the outer edge plasma. The typical duration of edge ICE driven by fusion-born ions ranges from 50 μs to 10 ms; whereas the duration of ICE driven ICRH-accelerated ions can be up to 1 s.
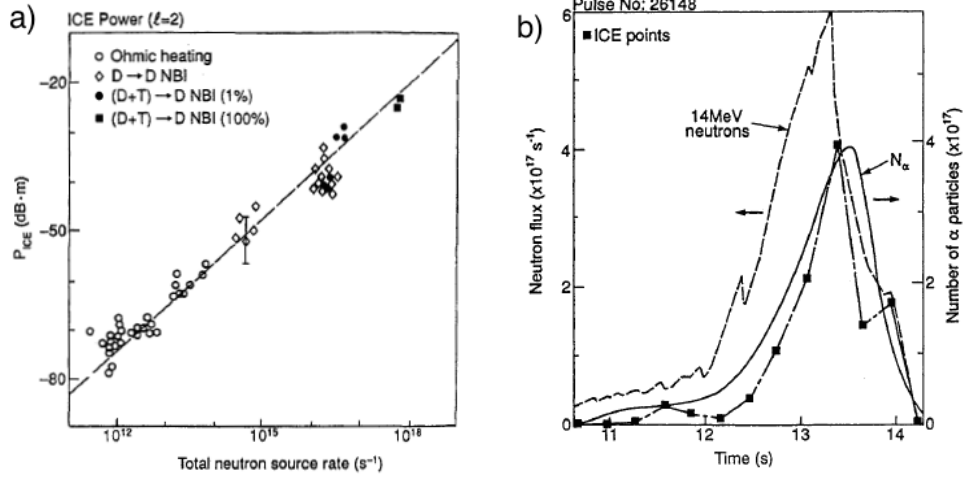
Figure 1.4: Scaling of the measured ICE intensity in JET P_{ICE} with neutron flux and alpha-particle concentration. Panel a): correlation between the ICE intensity P_{ICE} and the measured neutron flux in pure deuterium plasmas and D-T plasmas in JET. Linear scaling of P_{ICE} with the measured neutron flux is observed in all cases. Panel b): time evolution of the neutron flux (dashed line), P_{ICE} (squares), and the calculated population of alpha-particles at the outer edge plasma (solid line) in a D-T plasma in JET. Reproduced from Dendy et al. [1995].

- ICE driven by NBI. This type of ICE is steady and continuous in time.

- Central ICE originating at the core plasma. The driving source for this type of ICE is still unknown, but parallel NBI is needed. The typical duration of this kind of ICE is about 100 ms.

In the next section we introduce the magnetoacoustic cyclotron instability, the leading candidate instability driving edge ICE in JET and TFTR tokamaks.

1.3.3   The Magnetoacoustic Cyclotron Instability in fusion plasmas

Understanding the physics of the ICE emission mechanism provides a specific observational test of the theory and interpretation of energetic particle effects in magnetic confinement fusion (MCF) plasmas in an operationally important parameter regime. The analytical theory of ICE was originally developed in terms of the linear magnetoacoustic cyclotron instability (MCI) [Belikov and Kolesnichenko, 1976], for which the analytical theory was developed and applied to scenarios relevant to JET and TFTR soon after the experimental observations in these tokamaks Dendy et al. [1992, 1993, 1994b]; Fülöp and Lisak [1998]. This appears to capture some key observed features of the ICE measurements in TFTR and JET experiments. In particular, the linear MCI gives rise to: simultaneous excitation of fast Alfvén waves

16

at sequential multiple cyclotron harmonics of the alpha-particles [Cottrell et al., 1993]; strong growth rates for waves propagating nearly perpendicular to the magnetic field; linear scaling of the growth rate with alpha-particle concentration; and doublet splitting of the spectral lines (c.f. Fig. 11 of Dendy et al. [1995]).

In the analytically tractable formulation of the linear MCI relevant to edge ICE in JET and TFTR, the local fusion-born alpha-particle population is modelled as a drifting ring-beam distribution in velocity space, with a delta function distributed perpendicular velocity, and a Maxwellian distribution of velocities parallel to the magnetic field, that is,

$$f(v_\parallel, v_\perp) = \frac{1}{2\pi^{3/2} u_\perp v_r} \exp\left(-\frac{(v_\parallel - v_d)^2}{v_r^2}\right) \delta(v_\perp - u_\perp), \qquad (1.24)$$

where $v_\parallel$ and $v_\perp$ are the parallel and perpendicular velocity of the fusion-born alpha-particles, v_d and v_r are the average drift along the background magnetic field and the parallel velocity spread of the alpha-particles distribution, and $u_\perp$ is the magnitude of the initial perpendicular velocity of the alpha-particles corresponding to the energy of 3.5 MeV at which alpha-particles are born in D-T fusion reactions. This probability distribution function reflects the naturally occurring population inversion in the velocity distribution of centrally-born alpha-particles at the outer mid-plane edge, which have undergone large excursions from the core to the edge plasma in JET and TFTR [Cottrell et al., 1993; Dendy et al., 1995]. A typical orbit of such fusion-born alpha-particles is shown in Fig. 1.5.
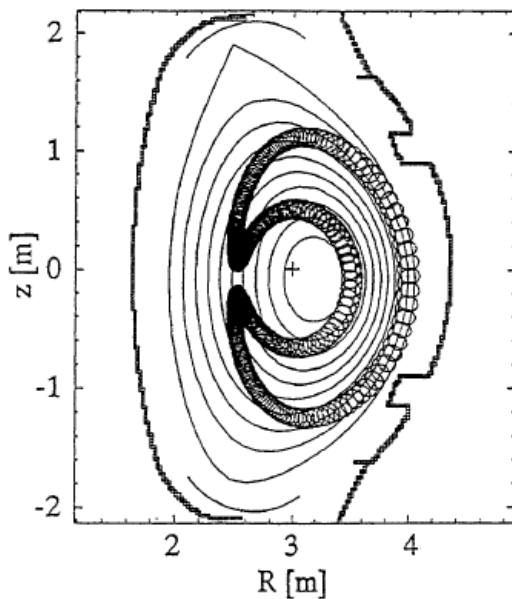
Figure 1.5: Poloidal projection of a typical orbit of an alpha-particle born at the core plasma and undergoing drift excursions to the outer edge plasma in JET. Reproduced from Dendy et al. [1995].

17

In the context of space plasmas, radiation similar to ICE, driven by energetic ions with drifting ring-like velocity distributions, has also been interpreted in terms of the MCI [Dendy and Mcclements, 1993; Mcclements and Dendy, 1993]. Most recently, the power spectrum of the downstream turbulence obtained from kinetic simulations of reforming perpendicular shocks in space plasmas, shows clear spectral peaks at consecutive ion cyclotron harmonics, suggesting the occurrence of ICE in the region behind the front shock [Rekaa et al., 2014].

1.4 Solar-wind plasma

Solar wind plasma, which is tenuous, multi-component, non-uniform, and mostly not at thermal equilibrium, serves as the main communication channel between the sun and the earth, which allows the propagation of energetic particles and disturbances, such as coronal mass ejections, that might pose a threat to modern electronic devices on earth. Therefore, it is of great importance to gain a deeper understanding of the origin and evolution of solar wind in order to lessen, and at a certain level prevent, the negative impact of space weather on modern life as it is known. The region between the solar corona (the nearest region surrounding the sun) and the heliosphere at 1 AU (the distance from the sun to the earth) spans a wide range of spatio-temporal scales and plasma parameters, such as number density and magnetic field strength. Therefore, it represents a naturally-occurring laboratory to study complex plasma phenomena over a wide range of scales and plasma parameters. For example, *in situ* observations of solar wind unveil the occurrence of ion heating driven by wave-particle interactions [Marsch, 2006], at the same time that large-scale MHD turbulence develops in solar wind [Bruno and Carbone, 2013]. Unfortunately, the disparity between the different temporal and spatial scales at which plasma phenomena occur, hinders the formulation of an "all-inclusive" model for solar wind.

A wide range of remote and *in situ* observations of solar wind carried out during the past three decades have provided important insights into the origin and dynamics of solar wind. These observations have permitted the classification of solar wind according to its parameters into two types: the energetic, low-density fast solar wind, which streams at ~ 800 km s^{-1} as it radially propagates away from the sun; and the dense, less energetic slow solar wind, which streams at ~ 400 km s^{-1} as it expands into the heliosphere. Observations of solar wind by the Ulysses spacecraft reveal that during the solar minimum, which is characterised by a few magnetically active regions around sunspots or coronal holes, the solar wind speed is a function of the latitude; with the fast solar wind emerging from coronal holes at high-latitudes, whereas the slow solar wind is confined to equatorial regions. However, this situation changes throughout a 11-years solar cycle, with a different scenario at solar maximum, when the coronal holes confined to high-latitudes at solar minimum now reach lower latitudes. In this case, solar wind speed is no longer a function of the latitude, and this new configuration produces a mix of slow and fast solar wind over all solar corona. Figure 1.6 shows a polar plot of solar wind speed as measured by the Ulysses spacecraft at solar minimum (left), and at solar maximum (right). The bottom panel of this figure shows the number of sunspots or

coronal holes as a function of time; the 11-year solar cycle is clearly observed.
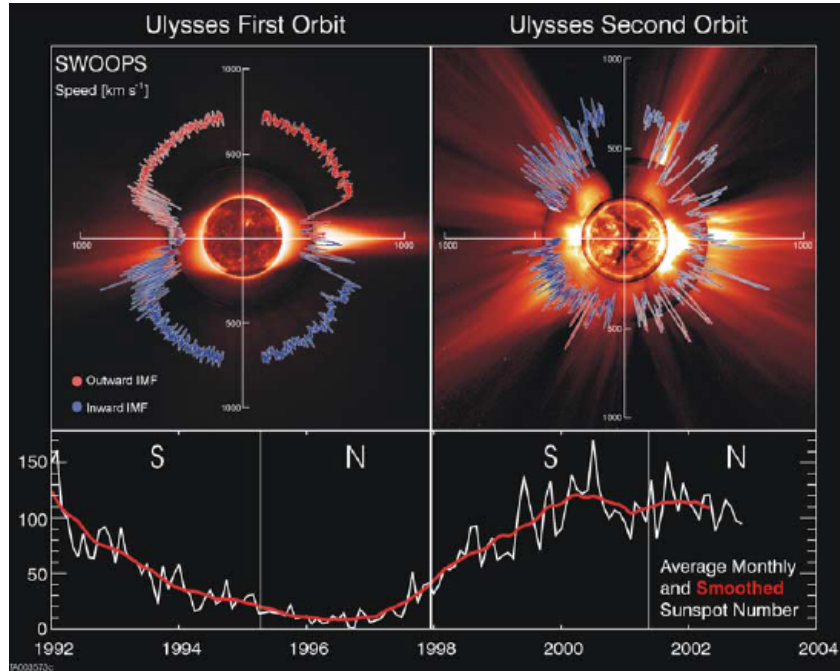
Figure 1.6: Composite image of the sun showing polar plots of solar wind speed as a function of the latitude as measured by Ulysses spacecraft at solar minimum (left), and at solar maximum (right). The vertical and horizontal axis in the top panels are solar wind speed in km s^{-1}. At solar minimum (left), solar wind speed has a clear dependence with latitude; whereas at solar maximum (right), the slow solar wind dominates, with sources of fast solar wind scattered over the whole solar corona. Bottom panel: number of sunspots or coronal holes as a function of time; the 11-year solar cycle is clearly observed. Reproduced from McComas et al. [2003].

Despite the exact origin of solar wind is still not well understood, there is some evidence [Tu et al., 2015] that fast solar wind might originate within coronal holes due to magnetic reconnection of initially-closed small flux tubes with open flux tubes located at coronal holes; whereas slow solar wind might originate in the surrounding area of coronal holes during magnetic reconnection of initially-closed larger flux tubes with open flux tubes located at the border of the coronal holes [Schwadron and McComas, 2003].

Once solar wind originates in solar corona, it starts to expand into the heliosphere, streaming radially outwards away from the sun. *In situ* measurements of solar-wind plasma parameters, such as number density, temperature and magnetic field strength, show that they are different for the fast and the slow solar wind: while the slow solar wind is relatively dense ($\sim$ 15 cm^{-3}) and cold ($\sim$ 5 $\times$ 10^4 K), the

fast solar wind is less dense (~ 4 cm^{-3}) and hotter ($\sim 2 \times 10^5$ K). Furthermore, the number density and magnetic field strength are more steady in the case of the fast solar wind; whereas for the case of the slow solar wind, these parameters fluctuate more. Figure 1.7 shows some plasma parameters of solar wind as measured by the Helios 2 spacecraft around day 75 of its first mission to the sun when it was ~ 0.5 AU away from the Sun. A clear transition region between slow solar wind (left-hand side of the plot) and fast solar wind (right-hand side of the plot) can bee seen in these plots in-between days 74 and 75.
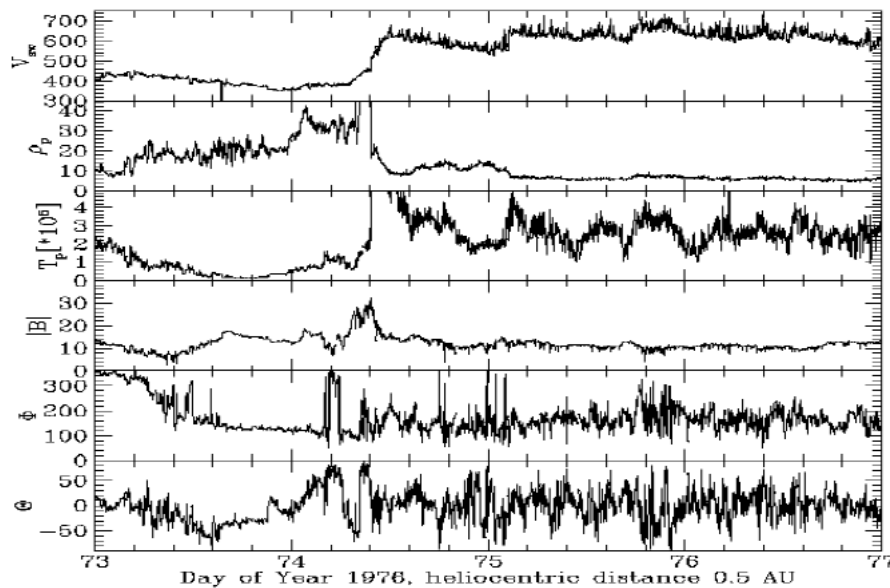
Figure 1.7: Solar-wind plasma parameters as measured by Helios 2 spacecraft around the day 75 of its first mission to the Sun when the spacecraft was ~ 0.5 AU away from the Sun. Panels from top to bottom: solar wind speed, proton number density, proton temperature, magnetic field strength, azimuthal angle, and elevation angle. Slow wind on the left-hand side of the plot, fast wind on the right hand side, and the fast-slow solar wind interface in between, can be clearly seen. Reproduced from Bruno and Carbone [2013].

In early [Belcher and Leverett, 1971; Belcher and Solodyna, 1975; Bruno et al., 1985] and recent [De Pontieu et al., 2007; Bruno and Carbone, 2013] studies of solar wind, strong correlations between fluctuations of the magnetic field $\delta\boldsymbol{B}$ and fluctuations of solar wind velocity $\delta\boldsymbol{U}$ of the form

$$\boldsymbol{\delta U} = \pm \frac{\delta \boldsymbol{B}}{\sqrt{\mu_0 n m_p}}, \tag{1.25}$$

have been seen for long periods of time; this equation is the so-called Walen's relation. Here, μ_0 is the vacuum magnetic permeability, n is the plasma number density,

and m_p is the proton mass. A strong correlation between the magnetic field fluctuations and solar wind velocity indicates the presence of Alfvén waves permeating solar-wind plasma. The minus (plus) sign in Eq. (1.25) refers to pure Alfvénic waves propagating parallel (anti-parallel) to the ambient magnetic field. Figure 1.8 shows the time evolution of the fluctuations of the magnetic field and solar wind velocity as measured by Mariner 5 spacecraft in its mission to Venus in 1967. During the 24 hours of measurements shown in this figure, a strong correlation between the magnetic field and solar wind velocity can be observed, which indicates the presence of Alfvén waves permeating solar wind [Belcher and Leverett, 1971; Belcher and Solodyna, 1975].
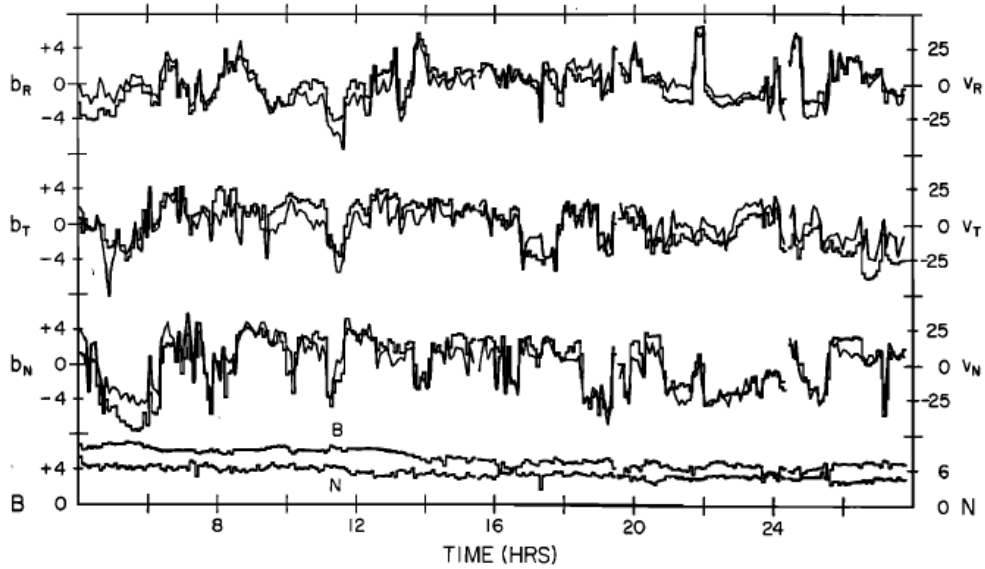
Figure 1.8: Time evolution of solar polar components (RTN) of the magnetic field and solar wind velocity as measured by Mariner 5 spacecraft. The top six curves show the magnetic field (horizontal and vertical lines) and solar wind velocity (diagonal lines) components. The two bottom lines show the magnetic field strength B and proton number density N. Strong correlation between the magnetic field and solar-wind velocity is observed, which indicates that solar wind is mainly permeated by outward-propagating Alfvén waves. Reproduced from Belcher and Solodyna [1975].

As previously mentioned, solar wind is a complex system in which plasma phenomena arise at multiple spatial and temporal scales. In general, the dynamics and properties of solar wind are different for the fast and slow solar wind, and they evolve as solar wind expands into the heliosphere. In the next sections some properties of solar wind are presented, namely, turbulence, intermittency, and preferential ion heating; whose mutual interactions will be studied in detail in Chapter 4.

1.4.1 Solar wind turbulence

Power spectra of the fluctuations of solar wind parameters exhibit inverse power laws in frequency domain, resembling those observed in turbulent flows in hydrodynamics. In the case of fast solar wind, at higher frequencies, there is an inertial range of fully developed turbulence $\sim f^{-5/3}$ [Marsch and Tu, 1990; Goldstein et al., 1995; Bruno and Carbone, 2013], and at low frequencies a region $\sim 1/f$ whose origin is coronal [Matthaeus and Goldstein, 1986; Bruno et al., 2009; Verdini et al., 2012]. In contrast, the slow solar wind appears to be close to a state of fully developed turbulence; that is, the slow solar wind spectra only shows an inertial range $\sim f^{-5/3}$ [Marsch and Tu, 1990; Bruno and Carbone, 2013]. This situation is clearly illustrated in Fig. 1.9, which shows power spectra of the magnetic field obtained from solar wind observations by the Ulysses and Helios 2 spacecrafts at different radial distances from the sun in the ecliptic plane. As can be seen, the break frequency (blue dot) at which the $1/f$ and the $f^{-5/3}$ regions separate, is a function of the heliocentric distance, that is, the break frequency moves to lower frequencies as the heliocentric distance increases. It is found that the functional dependence of the break frequency in the ecliptic plane with heliocentric distance is $\sim R^{-1.5}$, where R is the heliocentric distance. In Horbury et al. [1996] the authors found that the dependence with heliocentric distance of the break frequency for the case of the fast solar wind in the polar heliosphere is $\sim R^{-1.1}$, that is, the turbulence evolution in the polar wind is slower than the one in the ecliptic. This dependence of the break frequency on heliocentric distance seems to be an indication of non-linear interactions between non-adjacent scales in solar wind [Bruno and Carbone, 2013].

In Bruno et al. [1999], and more recently Salem et al. [2009] the authors showed that intermittency, that is, occasional large-amplitude fluctuations, or bursts, in the time series of solar wind parameters, can significantly modify the spectral properties of solar wind in its inertial range; producing anomalous scaling and departures from theoretical predictions of MHD turbulence models. In the next section we discuss how intermittency is observed in solar wind, and how intermittency affects solar wind properties.
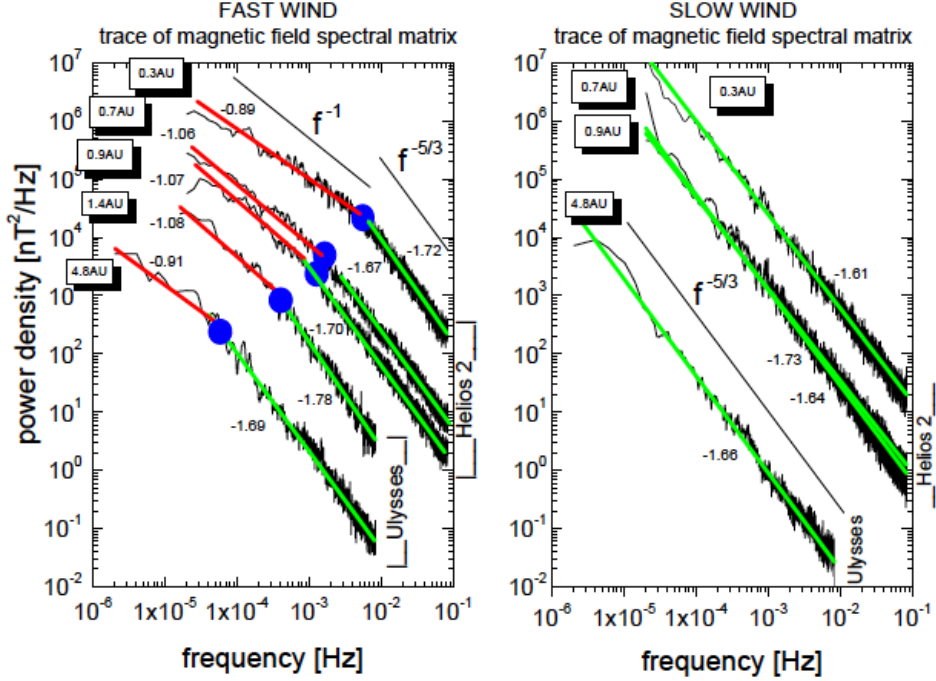
Figure 1.9: Power spectral density of the fluctuations of solar-wind magnetic field in the ecliptic plane at several heliocentric distances. Left panel: power spectral density of the fast solar-wind magnetic field fluctuations observed by Helios 2 between 0.3 and 1 AU during its first mission to the Sun in 1976, and by Ulysses between 1.4 AU in August of 2007 and 4.8 AU by the end of 1997. The break frequency separating the $1/f$ and $\sim f^{-5/3}$ regions of the power spectra shows a dependence with heliocentric distance R as $\sim R^{-1.5}$. Right panel: corresponding power spectra of the slow solar-wind magnetic field fluctuations. In contrast to the case for the fast solar wind, the slow solar wind spectra only show an inertial range $\sim f^{-5/3}$, independent of the heliocentric distance. Reproduced from Bruno and Carbone [2013].

1.4.2 Observations of intermittency in solar wind

There is evidence that solar wind inertial range fluctuations incorporate intermittent turbulence, that is, the occurrence of occasional large-amplitude fluctuations of solar wind parameters [Hnat et al., 2002; Bruno et al., 2007; Chapman and Hnat, 2007; Osman et al., 2012; Alexandrova et al., 2013; Wu et al., 2013]. In addition, intermittency is also seen in fluctuations at lower frequencies in the $1/f$ range of the fast solar wind [Hnat et al., 2003; Horbury et al., 2005]. Intermittency in solar wind, as in the case of intermittency in hydrodynamics [Frisch, 1995], can be defined in terms of either multifractal scaling of the structure functions of solar wind fluctuations [Hnat et al., 2007; Kiyani et al., 2007; Leonardis et al., 2013], or non-Gaussian

probability distribution functions of solar wind fluctuations [Hnat et al., 2002, 2003; Nicol et al., 2009; Wu et al., 2013; Subedi et al., 2014]. Both formalisms allow us to characterise solar wind turbulence by means of their statistical properties. Theoretical models of fully developed turbulence in the absence of intermittency, predict that the structure functions of pth order $(S_p(\tau))$ of the measured parameter $f(t)$ should exhibit scaling with the temporal scale τ, that is,

$$S_p(\tau) \equiv \langle |f(t+\tau) - f(t)|^p \rangle \sim \tau^{\zeta(p)}, \tag{1.26}$$

where $\langle \rangle$ is an average over time t, and $\zeta(p) = p/3$ in the case of fully developed turbulence in fluids [Frisch, 1995], and $\zeta(p) = p/4$ in the case of fully developed MHD turbulence [Kraichnan, 1965]. However, the scaling properties of the structure functions of the magnetic field $(f(t) = B(t))$ and solar wind velocity $(f(t) = U(t))$ show significant departures from the predictions of hydrodynamics and MHD turbulence theories [Burlaga, 1991; Marsch and Tu, 1997; Horbury and Balogh, 1997], which are signatures of intermittency [Merrifield et al., 2005, 2006, 2007]. In Fig. 1.10 the exponents $\zeta(p)$ of Eq. (1.26) up to $p = 6$ for the magnetic field and solar wind velocity as measured by the Wind spacecraft in 1995 are plotted. As can be seen from this figure, $\zeta(p)$ shows a nonlinear dependence with p, which indicates the presence of intermittency in solar wind.

Intermittency in solar wind also can be studied via the probability distribution functions (PDFs) of the fluctuations of solar wind parameters [Nicol et al., 2009; Osman et al., 2011, 2014]. Roughly speaking, in the case of fully developed turbulence in the absence of intermittency, the PDFs of the increments of $f(t)$, that is, $\delta f(t, \tau) \equiv f(t+\tau) - f(t)$, should be Gaussian for all τ. Therefore, any PDF of $\delta f(t, \tau)$ different from a Gaussian distribution, would indicate the occurrence of intermittency at scale τ. Fig. 1.11 shows the PDFs of the magnetic field increments $\delta B(t, \tau)$ of the fast (left) and slow (right) solar wind. Significant departures from Gaussianity are observed at time scales $\tau < 23.04$ hr, which indicates the presence of intermittency in the magnetic field.

Alternatively, intermittency can be defined in terms of phase coherence of the modes comprising the solar wind fluctuations. Phase coherence in solar wind has been observed in the form of coherent structures of the solar wind magnetic field [Stasiewicz et al., 2003]. Despite there is some work studying intermittency in solar wind from both points of view [Koga et al., 2007]: statistical (structure functions and PDFs) and phase coherence; there is no straightforward direct link between phase coherence and statistical intermittency properties.
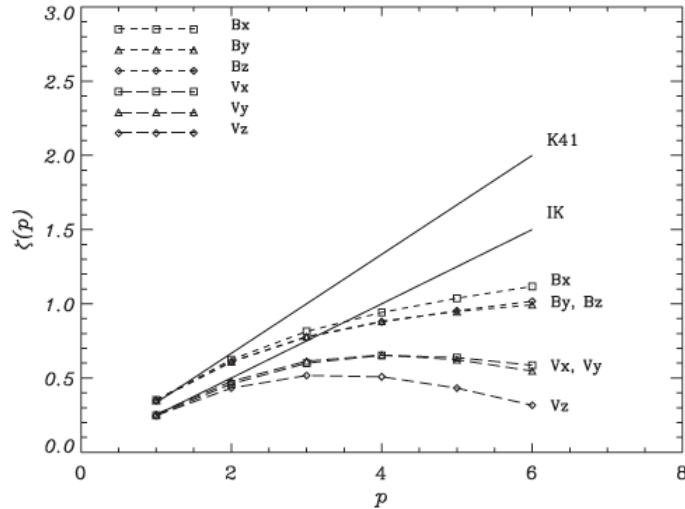
Figure 1.10: Scaling exponents of the structure functions of the magnetic field and solar wind velocity components as measured by Wind spacecraft in 1995. The solid lines show the theoretical predictions for fully developed fluid turbulence (K41), and magnetically-dominated fully developed turbulence (IK). Clear departures of $\zeta(p)$ from theoretical predictions can be seen, which indicates the presence of intermittency in solar wind. Reproduced from Salem et al. [2009].

Structure functions and probability distribution functions of the fluctuations of solar wind parameters, only can be used when very large time series of solar wind observations are available; this is necessary in order to obtain reliable estimates of $S_p(\tau)$ and $\mathrm{PDF}(\delta f(t, \tau))$. When the amount of data from observations is limited, there are few other methods that can be used. One example of such a method is the local intermittency measure (LIM), a method based on wavelet analysis [Torrence and Compo, 1998], first introduced in Farge [1992] to study the dynamics of coherent (bursty) structures in solar wind and to measure their contribution to the energy spectrum. This method is explained in detail in Sec. 4.3.4, where it is presented in the context of intermittency in hybrid simulations of preferential ion heating driven by intermittent electromagnetic fields.

1.4.3 Preferential ion heating in fast solar wind

Observations of solar wind typically show the existence of preferential heating of protons and alpha-particles along the local magnetic field. This preferential ion heating is observed in the reconstructed velocity probability distribution functions of protons and alpha-particles, which have long tails along the local magnetic field [Hundhausen et al., 1967; Gurnett et al., 1979; Marsch et al., 1982a,b; Marsch, 2006].
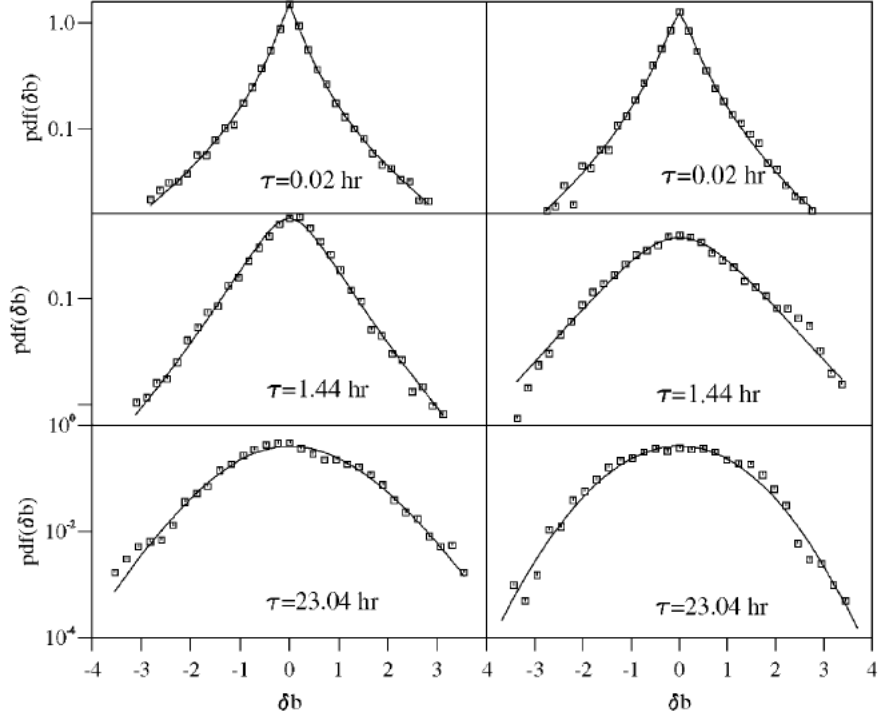
Figure 1.11: Probability distribution function of the magnetic field increments $\delta B(t, \tau)$ of the fast (left) and slow (right) solar wind as observed by Helios 2 spacecraft in 1976. Significant departures of a Gaussian distribution are observed at time scales $\tau < 23.04$ hr. Reproduced from Sorriso-Valvo et al. [2001].

Figs 1.12 and 1.13 show the reconstructed velocity probability distribution functions of protons and alpha-particles as a function of solar wind speed and heliocentric distance. In these figures the dashed line indicates the direction of the local magnetic field. As can be seen from Fig. 1.12, the velocity distribution of protons of the slow solar wind (left column) is anisotropic, but the occurrence of long tails along the local magnetic field are barely visible. For solar wind speeds ≥ 460 km s^{-1}, however, preferential ion heating of protons is clearly observed. Another feature of these reconstructed proton velocity distribution functions is that the initially tenuous proton beam along the local magnetic field at small heliocentric distances (≤ 0.39 AU), becomes more and more dense as the heliocentric distance increases. Furthermore, an elongation along the perpendicular direction to the local magnetic field of the core of the proton velocity distribution functions is also visible, which seems to be more evident at small heliocentric distances.

In a similar way, the reconstructed velocity probability functions of alpha-particles are observed to be highly anisotropic, with the formation of a beam of alpha-particles approximately parallel to the local magnetic field. This is shown in Fig. 1.13.
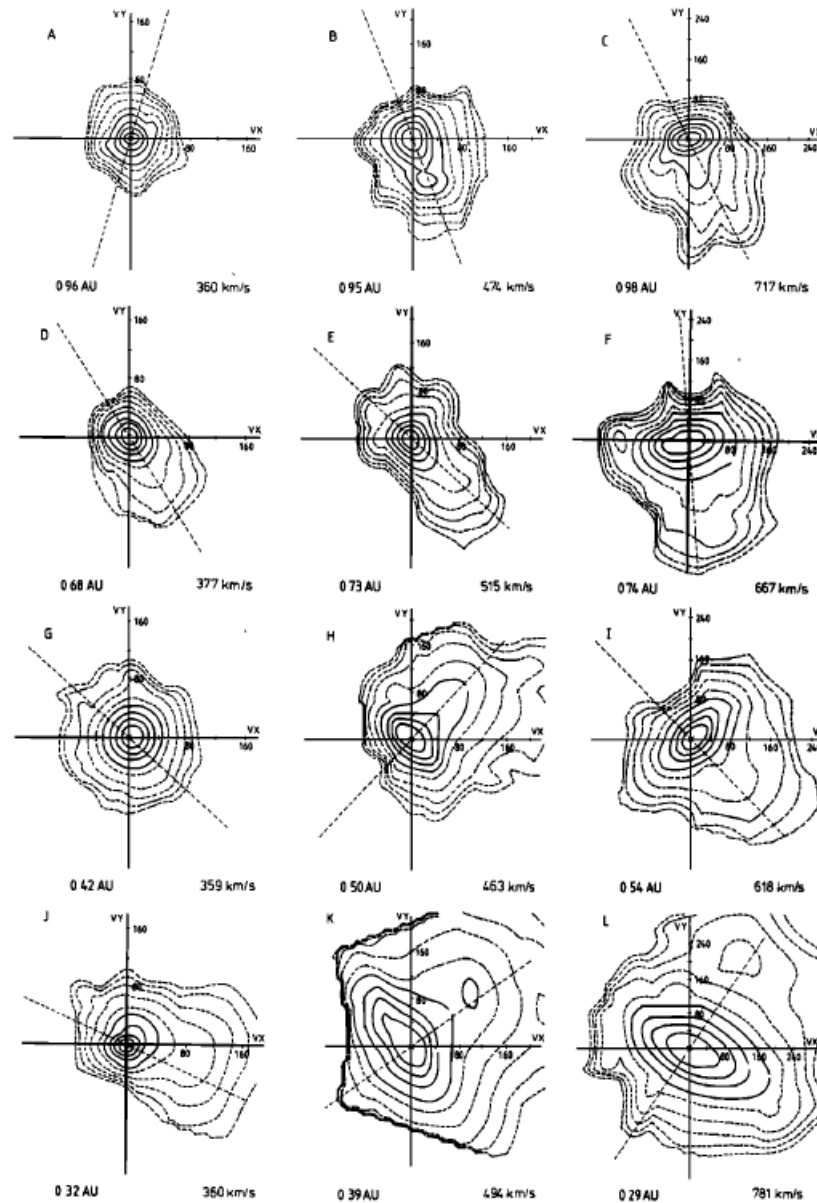
Figure 1.12: Reconstructed velocity probability distribution function of protons as measured by Helios 2 spacecraft for several solar wind speeds and heliocentric distances. The dashed lines indicate the direction of the local magnetic field. Reproduced from Marsch et al. [1982b].
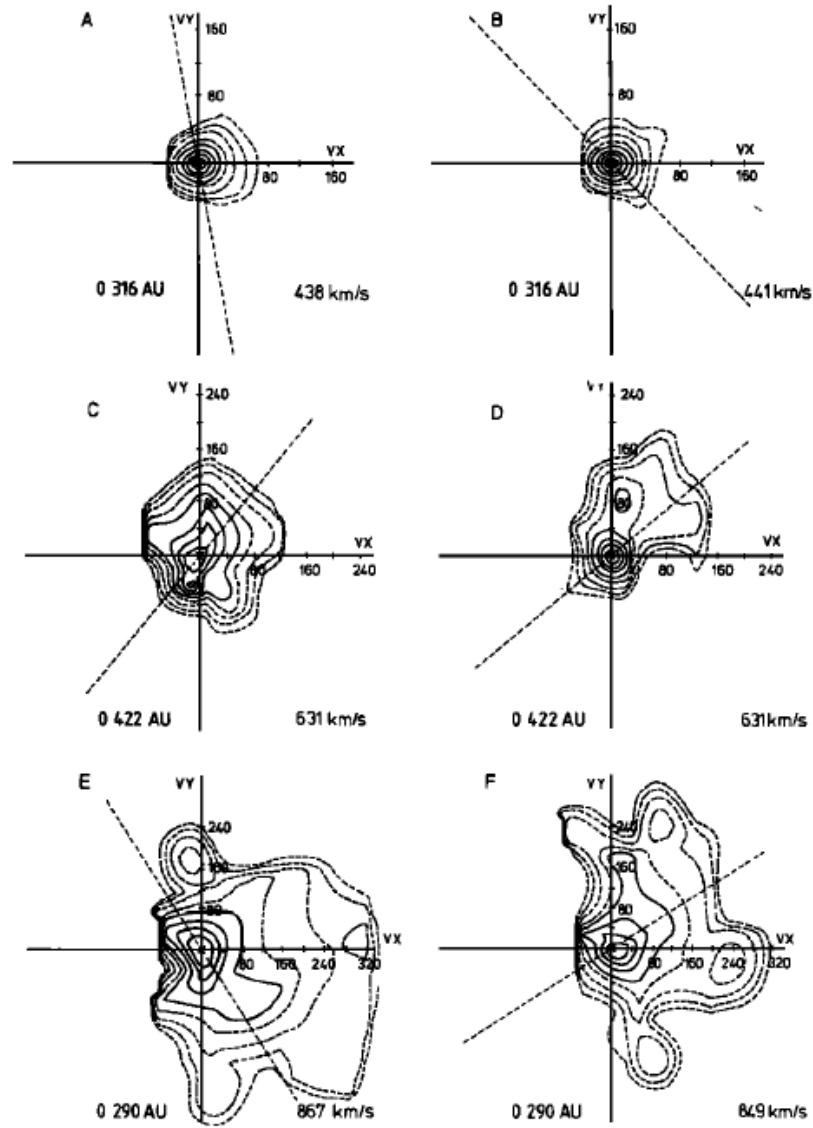
Figure 1.13: Reconstructed velocity probability distribution function of alpha-particles as measured by Helios 2 spacecraft for several solar wind speeds and heliocentric distances. The dashed lines indicate the direction of the local magnetic field. Reproduced from Marsch et al. [1982a].

Another parameter of solar wind that is usually measured is the ion temperature, which can be decomposed in its parallel ($T_{\parallel}$) and perpendicular ($T_{\perp}$) components with respect to the local magnetic field. In this way, a temperature anisotropy ratio $T_{\perp}/T_{\parallel} \neq 1$ can provide information about the occurrence of preferential ion heating in solar wind. Fig. 1.14 shows the probability distribution function of $T_{\perp}/T_{\parallel}$

as measured by the Wind spacecraft at ~ 1 AU for protons (left) and alpha-particles (right) as a function of the parallel ion beta $\beta_i = 2\mu_0 n_i k_B T_\parallel / B_0^2$, where μ_0 is the vacuum magnetic permeability, n_i is the ion number density, k_B is the Boltzmann constant, and B_0 is the local magnetic field strength. As can be observed, the values of $T_\perp/T_\parallel$ for protons and alpha-particles range from $T_\perp/T_\parallel = 0.1$ to $T_\perp/T_\parallel = 10$, but the more frequent values of $T_\perp/T_\parallel$ at ~ 1 AU for protons [Marsch et al., 1982b] and alpha-particles [Marsch et al., 1982a] are $T_{p\perp}/T_{p\parallel} < 1$ and $T_{\alpha\perp}/T_{\alpha\parallel} \lesssim 1$, respectively.

The mechanisms driving the observed preferential ion heating in solar wind are still not well understood. Significant theoretical and simulation work has been done in order to explain preferential ion heating in solar wind, see Marsch [2006] and Matteini et al. [2011] for a review on recent studies on preferential ion heating. All these studies provide mechanisms and configurations of solar wind plasmas that might underlie the observed preferential ion heating, but the intermittent character of the solar wind is not included in their models. In Chapter. 4 we present the first study of preferential ion heating driven by $1/f^\gamma$ broadband spectra of Alfvén waves including intermittency in a self-consistent way.
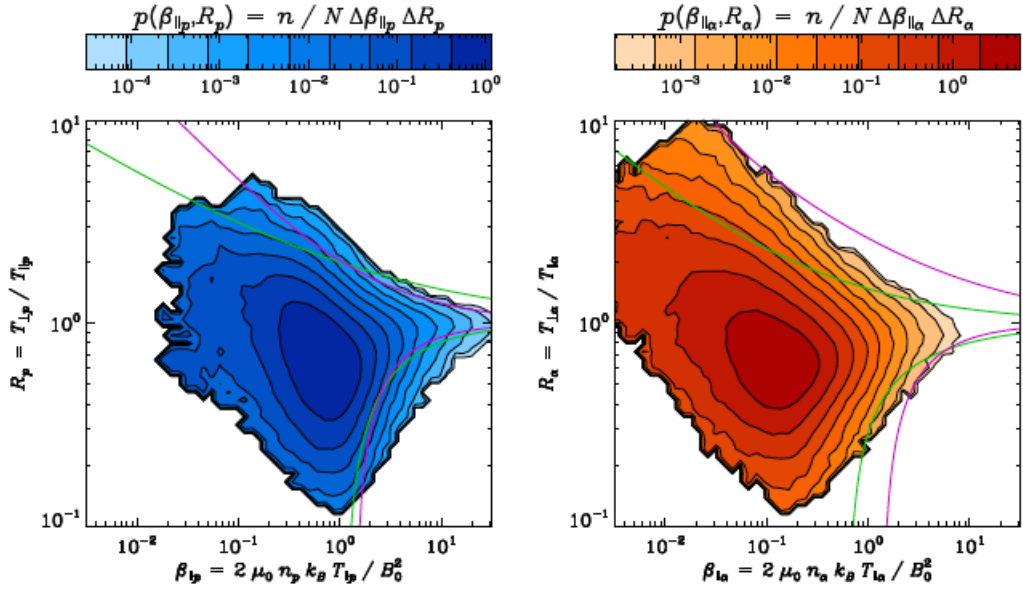
Figure 1.14: Probability distribution function of $T_\perp/T_\parallel$ as measured by the Wind spacecraft at ~ 1 AU for protons (left) and alpha-particles (right) as function of the parallel ion beta $\beta_i = 2\mu_0 n_i k_B T_\parallel / B_0^2$. Dark tones of blue and red indicate more frequent observations of the temperature anisotropy $T_{i\perp}/T_{i\parallel}$ for a given β_i. Reproduced from Maruca [2012].

Chapter 2

PROMETHEUS++: The 1.5D hybrid code

A new code has been developed [Carbajal et al., 2013] to study the full self-consistent dynamics of energetic ions in fusion and space plasmas using the hybrid approximation for a plasma of Sec. 1.2. This code, named PROMETHEUS++, uses paradigms from high performance computing (HPC) that allow us to evolve the full velocity space distributions of different ion populations by following an ensemble of super-particle trajectories in phase space, while the dynamics of the fluid electrons and electromagnetic fields are solved on a fixed grid in physical space. Our 1.5D simulations evolve the full 3D vector electromagnetic fields with variation in one spatial direction and time. PROMETHEUS++ allows us to simulate a wide range of plasma conditions with plasma beta values ranging from $\beta \sim 10^{-4}$, for fusion plasma conditions, to $\beta \sim 1$, for astrophysical plasma conditions.

In this chapter, the structure of PROMETHEUS++ and the numerical schemes used to solve the equations of the plasma in its hybrid approximation is described. Next, we present the results of the benchmark of PROMETHEUS++ using three well understood problems in plasma physics: the warm plasma dispersion relation, the resonant electromagnetic ion-ion instability and the electromagnetic ion cyclotron beam anisotropy. Finally, the benchmark results, limitations and future work to further develop PROMETHEUS++ are discussed.

2.1   Overview of PROMETHEUS++

PROMETHEUS++ code is written in C++, allowing us to use object-oriented programming to provide PROMETHEUS++ with a modular structure. This means

that the functionality of each module of the code is independent of other modules, allowing us to plug or unplug modules without modifying the rest of the code; this way of self-contained data and functions within each module is known as encapsulation in C++ programming. Each module is a C++ library made of one or several C++ classes that communicate with other modules by passing standardized data structures through the main function of the code. PROMETHEUS++ has two main data structures to keep track of data relevant to each ion species and electromagnetic fields: *ionSpecies*, which keeps ions' parameters such as charge, mass, positions and velocities; as well as bulk variables of each ion species such as the number density n_j and the ion bulk velocity $\boldsymbol{u}_j$. Similarly, the data structure *electromagneticFields* keeps the data of the electric and magnetic fields. In addition, the data structure *inputParameters* contains all the simulation parameters that define the plasma parameters in the simulations, and specific control parameters of each module of the code. These simulation parameters are loaded from two input files at the beginning of the simulation.

Figure 2.1 shows a diagram with all the modules forming PROMETHEUS++. The modules *mpi_main*, *types* and *structures*, together with the main function are the core of the code. The other modules shown in orange contain the numerical solvers for the ions and electromagnetic fields, as well as additional modules in charge of the input/output operations during each simulation. The modules *alfvenic* and *generalFunctions* shown in blue, are optional modules that can be unplugged or replaced by new modules according to the requirements of the simulation set-up. The module *alfvenic* includes Alfvén waves into the initial condition of the simulations, and the module *generalFunctions* contains specific functions and diagnostics for some specific set-ups. Additional modules can be plugged to PROMETHEUS++ to include further physics, diagnostics, or to set up specific initial conditions.

In Fig. 2.2 we show the simulation process of PROMETHEUS++, which consists of two stages: an initialisation stage, where the simulation parameters are loaded, the initial conditions for ions and electromagnetic fields are set up, and the simulation variables are normalised; followed by the simulation stage, where ions and fields are advanced in space and time. Any additional initialisation such as the inclusion of plasma waves is done before the normalisation of the simulation variables.

We have used geometric decomposition as the parallel programming paradigm of PROMETHEUS++, which is shown schematically in Fig. 2.3. This paradigm consists of dividing the entire one-dimensional domain into sub-domains which communicate with each other through a Message Passing Interface (OpenMPI). Ad-
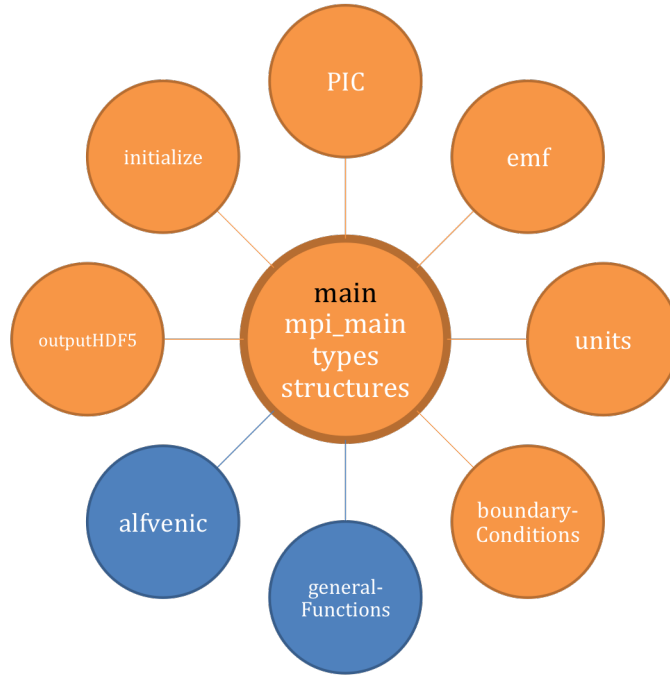
Figure 2.1: Modules of PROMETHEUS++. The modules *mpi_main*, *types* and *structures* together with the main function are the core of the code, the rest of the modules communicate amongst themselves by passing standardized data structures through the main function. The modules that contain the numerical solvers for the ions and electromagnetic fields, as well as the input/output functions of the code are shown in orange. Optional modules that can be unplugged or modified for specific purposes are shown in blue.

ditionally, within each sub-domain we use shared memory parallel programming (OpenMP). In this way, each sub-domain represents an MPI process [Gropp et al., 2014] with its own copy of the code, which in turn is divided into several OpenMP threads within each sub-domain [Chapman et al., 2008]. During the initialisation process each MPI process (sub-domain) is assigned a set of ions, for which dynamics will be solved by its corresponding MPI process for the duration of the simulation; that is, the link between each set of ions and its corresponding MPI process is fixed during the entire simulation. Importantly, this hybrid parallel programming method (OpenMP+OpenMPI) can only be used in clusters made of multi-core nodes that have their own shared memory.

Finally, the simulation outputs, which contain all the relevant data and parameters for the post-processing process, are stored in multiple HDF5 files. The number of HDF5 files is the same as the number of MPI processes used in the simulations. The HDF5 format is a standard used in high-performance computing (HPC) with excellent capabilities for managing large sets of data and allows us to
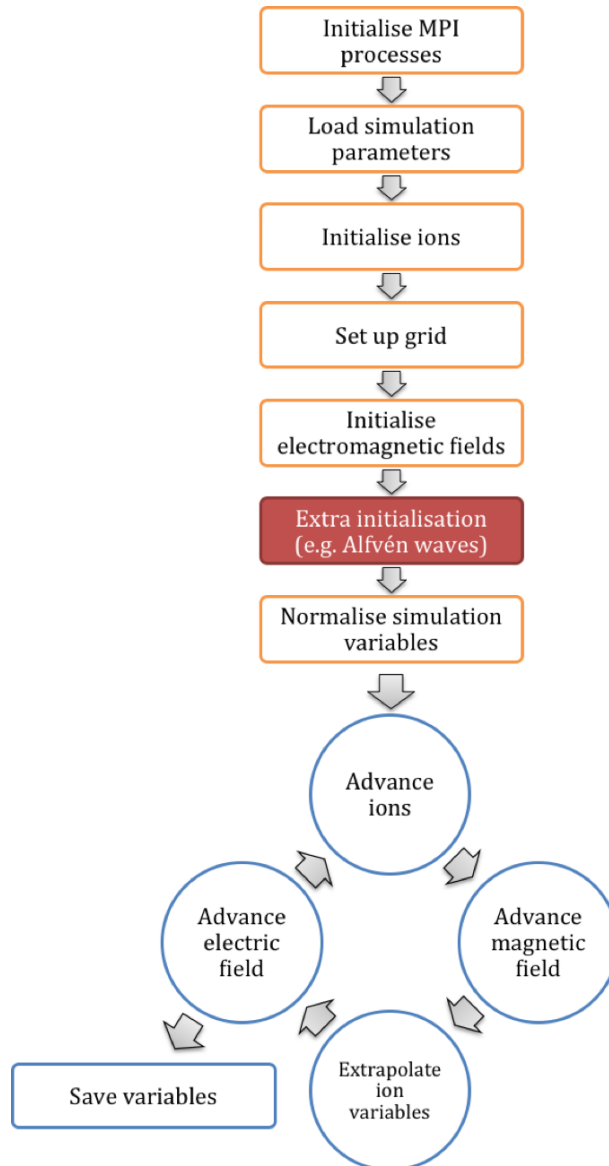
Figure 2.2: Simulation process of PROMETHEUS++. The whole simulation process consist of two stages: an initialisation stage, in orange, followed by the simulation stage, in blue. Any additional initialisation (in red) is done before the normalisation of the simulation variables.

perform the post-processing process using any software that supports the HDF5 format such as Matlab and Python. Further development will allow the outputs of PROMETHEUS++ to be inputs of visualization software.
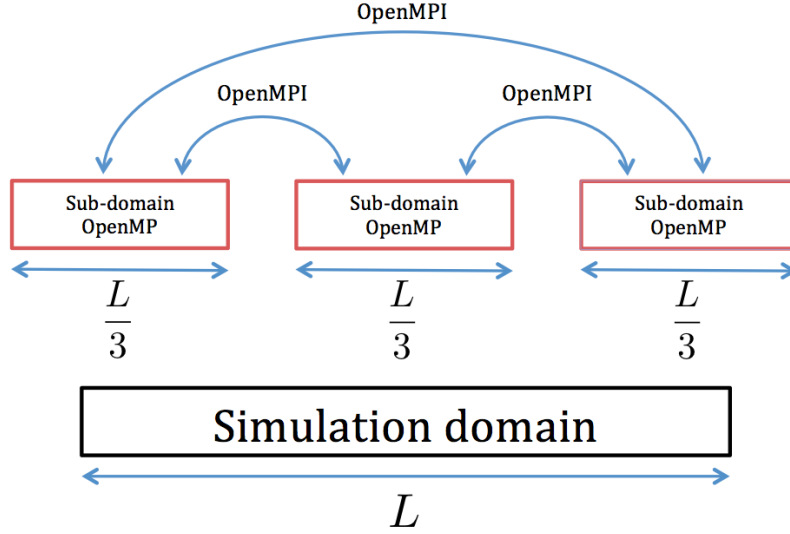
Figure 2.3: Hybrid parallel programming method. We use a geometry decomposition paradigm to divide the entire simulation domain into sub-domains which communicate with each other through OpenMPI. Additionally, within each sub-domain we use shared memory parallel programming (OpenMP).

2.1.1 Units and normalisation

The input and output files of PROMETHEUS++ have physical units, all in SI units. The normalisation of the simulation variables is needed to reduce round-off errors by combining large and small numbers, and is carried out within the code during the initialisation stage of each simulation. In Table 2.1 we show the characteristic plasma parameters used to normalise the simulation variables [Winske and Omidi, 1993].

Table 2.1: Characteristic plasma parameters used to normalise the simulation variables.

Length	d_i	ion skin depth
Time	ω_i^{-1}	Inverse of ion plasma frequency
Velocity	c	Light speed in vacuum
Mass	$\bar{m}_i$	Average ion mass
Charge	$\bar{q}_i$	Average ion charge
Number density	n_e	Electron number density (c.f. Eq. (1.15))
Electric field	$\omega_i \bar{m}_i c / \bar{q}_i$	
Magnetic field	$\omega_i \bar{m}_i / \bar{q}_i$	
Temperature	$\bar{m}_i c^2 / k_B$	k_B is the Boltzmann constant

2.2 Numerical schemes

In this section the numerical schemes used in PROMETHEUS++ to solve the equations of the plasma in its hybrid approximation are presented. First, the spatial discretisation of the simulation domain used to solve the electromagnetic fields is presented, followed by the description of the charge assignment and force interpolation scheme that self-consistently couple the different populations of ions with the electromagnetic fields. Next, the temporal discretisation used to advance in time the ions and electromagnetic fields is presented. Finally, the model of numerical diffusion used in PROMETHEUS++ that provides better numerical stability is described.

2.2.1 Spatial discretisation

We use a first-order forward finite differences on an one-dimensional staggered grid [Yee, 1966; Buneman, 1993] with periodic boundary conditions to solve the electromagnetic fields in physical space. The first-order forward finite difference scheme approximates the spatial derivative of a function $f(x)$ with respect to x as follows:

$$\frac{df(x)}{dx} = \frac{f(x + \Delta x) - f(x)}{\Delta x}, \tag{2.1}$$

where Δx is the width of each grid cell along the x-axis. Figure 2.4 shows a three-dimensional staggered grid, which is a generalisation of three spatial dimensions of the one-dimensional staggered grid used in PROMETHEUS++. The components of the magnetic field $\boldsymbol{B}(\boldsymbol{x})$ (shown as $\boldsymbol{H}(\boldsymbol{x})$ in this figure) are located at the centre of the faces of each grid cell. Conversely, the components of the electric field $\boldsymbol{E}(\boldsymbol{x})$ are located at the middle of the edges of each grid cell. The use of a staggered grid allows us to calculate $\nabla \times \boldsymbol{E}$ at the location of the magnetic field $\boldsymbol{B}$, while $\nabla \times \boldsymbol{B}$ will be correct at the location of the electric field $\boldsymbol{E}$ when a finite differences scheme is used. Furthermore, the staggered grid transforms Eq. (2.1) from a forward difference with an error of order Δx to a central difference operator with an error of order $O(\Delta x^2)$.

Following Buneman [1993], the number density and ions' bulk velocity of Eq. (1.16) and (1.15) are defined at the positions where the electric field components are located. In the next section we introduce the method that allows us to both define the number density and ions' bulk velocity on the grid, and to extrapolate the value of the electromagnetic fields from the grid to the ions' positions.

36
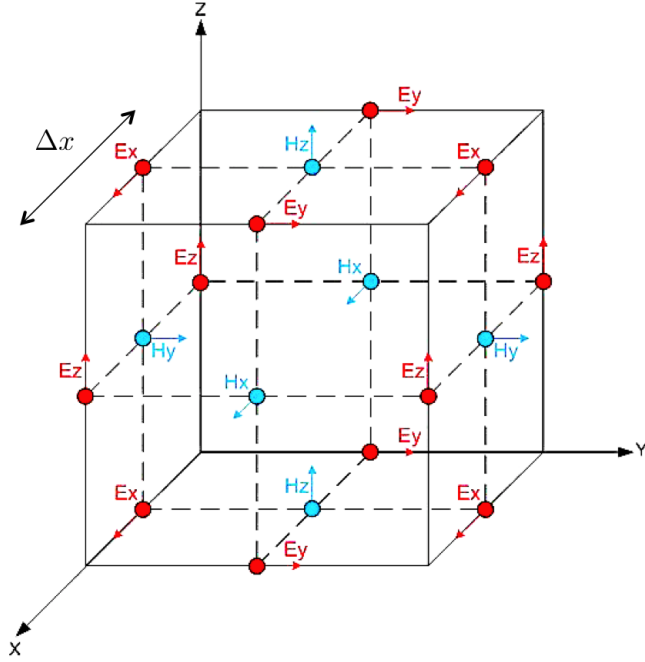
Figure 2.4: One grid cell of a cuboidal staggered grid used for solving the electric and magnetic fields in physical space. A one-dimensional version of this grid is used in PROMETHEUS++. The components of the magnetic field (shown as $\boldsymbol{H}$ in this figure) are located at the centre of the faces of each grid cell (blue dots and vectors). Similarly, the components of the electric field are located at the middle of the edges of each grid cell (red dots and vectors).

2.2.2 Charge assignment and force interpolation scheme

The hybrid approximation for the plasma treats ions as kinetic particles, each governed by the Lorentz force. Typical values of the ion number density of solar wind plasmas, $n \sim 10^6$ m^{-3}, and fusion plasmas, $n \sim 10^{19}$ m^{-3}, imply that one should solve an equivalent number of equations of motion for all the ions within the plasma, representing a big challenge even for current computer clusters. One solution to this problem is to use the super-particle representation for kinetic ions, as it is done in usual particle-in-cell (PIC) plasma simulations [Hockney and Eastwood, 1989]. The super-particle representation for plasmas assumes that the ion populations consist of computational particles (super-particles) made of N_j ions of species j, which are assumed to be strongly correlated so that their trajectories in phase space are approximately described by the equations of motion of the super-particle's centre of mass

$$\frac{d\boldsymbol{x}_j}{dt} = \boldsymbol{v}_j \,, \tag{2.2}$$

$$M_j \frac{d\boldsymbol{v}_j}{dt} = eZ_j N_j \left(\boldsymbol{E} + \boldsymbol{v}_j \times \boldsymbol{B} \right) \,, \tag{2.3}$$

where $M_j = m_j N_j$ is the mass, and $\boldsymbol{x}_j$ and $\boldsymbol{v}_j$ are the position and velocity of the centre of mass of the super-particle of ion species j, respectively.

The super-particle representation for ions assumes that the super-particles have a finite size in physical space. In computational plasma physics, the super-particle shape in physical space is defined by the assignment function shape $W(x)$ [Hockney and Eastwood, 1989]. In order to have a smooth and continuous representation of ion bulk variables such as the number density n and ion bulk velocity U_i in the hybrid simulations, the Triangular Shape Cloud (TSC) assignment function has been used. This shape also ensures that the first derivative of n and U_i is also continuous. In Fig. 2.5 the TSC assignment function used in PROMETHEUS++ is shown.
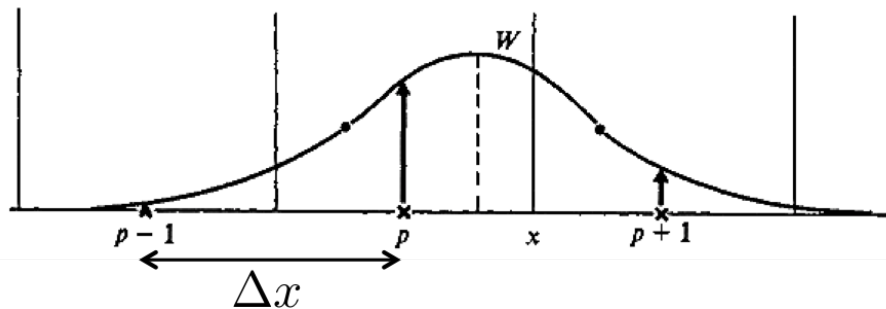
Figure 2.5: Super-particle shape in physical space given by the TSC assignment function. Figure reproduced from Hockney and Eastwood [1989]. The fraction of each super-particle variable (e.g. charge and ion velocity) that corresponds to a given grid point p (marked with crosses) is given by the value of the TSC assignment function shape W at that point (c.f. Eq. (2.4)).

The TSC assignment function is defined as follows:

$$W(x_j) = \begin{cases} \frac{3}{4} - \left(\frac{x_j}{\Delta x}\right)^2 & |\ x_j\ | \leq \frac{\Delta x}{2} \\ \frac{1}{2}\left(\frac{3}{2} - \frac{|x_j|}{\Delta x}\right)^2 & \frac{\Delta x}{2} \leq |\ x_j\ | \leq \frac{3\Delta x}{2} \\ 0 & \text{otherwise} \end{cases} \tag{2.4}$$

where Δx is the grid cell width, and x_j is the position of the super-particle centre of mass along the x-axis. Through this function we can define the bulk ion variables

on the grid, and extrapolate the electromagnetic fields from the grid to the super-particles' position. For example, the number density of super-particles of species j at an arbitrary position x is defined as:

$$n_{\mathrm{sp}j}(x) = \sum_l^N \delta\left(x - x_{jl}\right), \tag{2.5}$$

where N is the total number of super-particles of ion species j in the simulation, and x_{jl} is the position of the lth super-particle of species j. Therefore, the number density of ion species j at the grid point located at x_p (c.f. Fig. 2.5) is given by

$$n_j(x_p) = N_j \int n_{\mathrm{sp}j}(x')W(|x_p - x'|)dx', \tag{2.6}$$

where W is the TSC assignment function (Eq. (2.4)), and N_j is the number of ions within each super-particle. Here, the integral goes along the entire simulation domain. Other bulk ion variables, e.g. the ions' bulk velocity, can be defined on the grid in a similar way.

Furthermore, the electromagnetic fields are extrapolated from the grid point located at x_p to the lth super-particle position x_{jl} as follows

$$A(x_{jl}) = \int A(x')W(|x_{jl} - x'|)dx', \tag{2.7}$$

where $A(x')$ can be any component of the electric or magnetic field. In this way, Eqs. (2.4) to (2.7) completely define how ion dynamics are self-consistently coupled to the electromagnetic fields located on the discrete staggered grid.

2.2.3 Temporal discretisation

In this section, we discuss the methods used to discretise in time the equations of the plasma. We use a time-centered finite difference leapfrog (FDL) method [Hockney and Eastwood, 1989; Winske and Omidi, 1993] to advance in time fields and ions in the hybrid simulations of the plasma. This method consists of approximating the time derivative of a function $f(t)$ as

$$\frac{df(t)}{dt} \approx \frac{f(t + \Delta t) - f(t)}{\Delta t}, \tag{2.8}$$

where $\Delta t = t_{tot}/N_t$ is the time step used to advance ions and fields in the code. This time step, which results from dividing the total simulation time t_{tot} into N_t small time steps, must be small enough in order to fulfill the Courant-Friedrichs-Lewy (CFL) condition for numerical stability [Press, 2007; Pritchett, 2000]. The

CFL condition sets a limit for the size of the time step Δt used in each simulation to ensure there exists enough time resolution to follow in detail the electromagnetic fields and ions as they move along the simulation domain.

In the FDL method, positions and fields are defined at integral times $t_l = l\Delta t$, while velocities are defined at half-integral times $t_{l+\frac{1}{2}} = (l + 1/2)\Delta t$. This is shown schematically in Fig. 2.6. Here, $l = 1, 2, \ldots, N_t$. In this way, the super-particle equations of motion, Eqs. (2.2) and (2.3), become

$$\boldsymbol{x}_j^{l+1} - \boldsymbol{x}_j^l = \Delta t \boldsymbol{v}_j^{l+\frac{1}{2}}, \tag{2.9}$$

$$\boldsymbol{v}_j^{l+\frac{1}{2}} - \boldsymbol{v}_j^{l-\frac{1}{2}} = \frac{eZ_j N_j \Delta t}{M_j}\left(\boldsymbol{E}^l(\boldsymbol{x}_j^l) + \boldsymbol{v}_j^l \times \boldsymbol{B}^l(\boldsymbol{x}_j^l)\right), \tag{2.10}$$

where the superscripts indicate the time at which the super-particle variables and electromagnetic fields are evaluated. Here, $\boldsymbol{E}^l(\boldsymbol{x}_j^l)$ and $\boldsymbol{B}^l(\boldsymbol{x}_j^l)$ refer to the electric and magnetic field as evaluated at the position of the super-particle $\boldsymbol{x}_j^l$ at time $t_l = l\Delta t$, which are obtained through Eq. (2.7). In Eq. (2.10) the super-particle velocity $\boldsymbol{v}_j^l$ evaluated at the integer time step $t_l = l\Delta t$ is approximated as $\boldsymbol{v}_j^l = (\boldsymbol{v}_j^{l-\frac{1}{2}} + \boldsymbol{v}_j^{l+\frac{1}{2}})/2$.
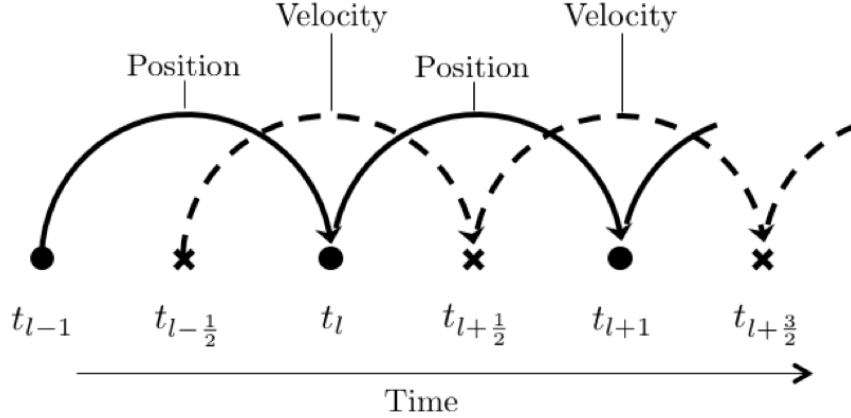
Figure 2.6: Time-centered finite differences approximation leapfrog method to advance ions and fields in time.

The time evolution of the electric field is solved through the generalised Ohm's law:

$$\boldsymbol{E}^l = \frac{1}{\mu_0 e n^l}(\nabla \times \boldsymbol{B})^l \times \boldsymbol{B}^l - \boldsymbol{U}_i^l \times \boldsymbol{B}^l - \frac{1}{en^l}\nabla P_e^l. \tag{2.11}$$

As before, the superscripts in this equation indicate the time at which the variables

40

are evaluated. Notice that all the quantities in Eq. (2.11) are calculated at the grid points where the electric field is located. Furthermore, the value of the ions' bulk velocity $\boldsymbol{U}_i$ at the integer time step t_l is calculated using a 4th order Bashford-Adams extrapolation [Winske et al., 2003]:

$$\boldsymbol{U}_i^l = 2\boldsymbol{U}_i^{l+\frac{1}{2}} - \frac{3}{2}\boldsymbol{U}_i^{l-\frac{1}{2}} + \frac{1}{2}\boldsymbol{U}_i^{l-\frac{3}{2}} . \tag{2.12}$$

On the other hand, the magnetic field is advanced in time using Faraday's law. We use a 4th-order Runge-Kutta scheme [Terasawa et al., 1986; Winske et al., 2003] to discretise Faraday's law in time, which provides numerical stability by reducing high-frequency noise in the simulations. This method, also known as subcycling, consists of dividing the original time step Δt into N_{RK} smaller time steps $\Delta t' = \Delta t/N_{RK}$. In this way, the magnetic field is advanced from t_l to $t_{l+s} = l\Delta t + s\Delta t'$ as follows

$$\boldsymbol{B}^{l+s} = \boldsymbol{B}^l + \frac{\Delta t'}{6}\left(\boldsymbol{K_1}^l + \boldsymbol{K_2}^l + \boldsymbol{K_3}^l + \boldsymbol{K_4}^l\right), \tag{2.13}$$

$$\boldsymbol{K_1}^l = -\nabla \times \boldsymbol{E}(\boldsymbol{B}^l), \tag{2.14}$$

$$\boldsymbol{K_2}^l = -\nabla \times \boldsymbol{E}(\boldsymbol{B}^l + \frac{\Delta t'}{2}\boldsymbol{K}_1^l), \tag{2.15}$$

$$\boldsymbol{K_3}^l = -\nabla \times \boldsymbol{E}(\boldsymbol{B}^l + \frac{\Delta t'}{2}\boldsymbol{K}_2^l), \tag{2.16}$$

$$\boldsymbol{K_4}^l = -\nabla \times \boldsymbol{E}(\boldsymbol{B}^l + \Delta t'\boldsymbol{K}_3^l), \tag{2.17}$$

where $s = 1, \ldots, N_{RK}$, and the electric field $\boldsymbol{E}$ in Eq. (2.14) to (2.17) is calculated using Eq. (2.11) with all the right-hand side terms as evaluated at t_l except for the magnetic field, which is replaced by $\boldsymbol{K}$ calculated in Eqs. (2.14) to (2.17).

In this way, Eq. (2.8) to (2.17) completely define the time discretisation used in PROMETHEUS++. The order of how ions and electromagnetic fields are advanced in time is shown in Fig. 2.7.

2.2.4 Numerical stabilisation method

In general, a stabilisation method is needed in plasma simulations using the hybrid approximation for the plasma because in this approximation the plasma cannot self-consistently damp short-wavelength high-frequency modes, which are normally damped by electron kinetic effects. If these modes are not artificially damped, they will grow unbounded, generating non-physical effects in the simulations.

We include some numerical diffusion to the electromagnetic fields, $\boldsymbol{E}$ and $\boldsymbol{B}$,
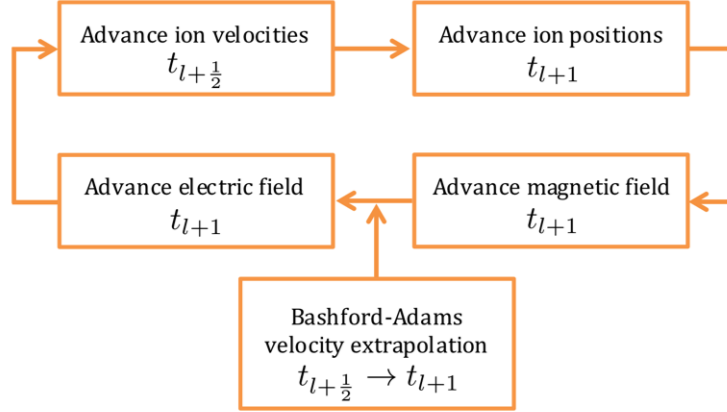
Figure 2.7: Cycle of a time iteration of PROMETHEUS++. First, ion velocities are advanced in time, followed by their positions (c.f. Eq. (2.9) and (2.10)). Then, the magnetic field is advanced using a 4th order Runge-Kutta scheme (c.f. Eq. (2.13) to (2.17)). Finally, the electric field is advanced in time using a 4th order Bashford-Adams extrapolation for the ions' bulk velocity (c.f. Eq. (2.11) and (2.12)).

and ion bulk variables, n_j and $\boldsymbol{u}_j$ (c.f. Eq. (1.15) and (1.16)), each time iteration in order to attenuate short-wavelength modes. This method allows the existence of small amplitude short-wavelength modes in comparison to methods similar to low-pass filtering that set to zero all modes below a given wavelength threshold value [Gilboa, 2013]. Regarding energy conservation, we find that numerical diffusion provides much better energy conservation in comparison to low-pass filtering. The numerical diffusion method we include in PROMETHEUS++ is similar to a high order Laplace operator when a finite differences method is used to discretise the equations of the plasma in its hybrid approximation [Müller et al., 2011]. This method consists of two steps: if $\mathcal{A}_p$ is an arbitrary plasma variable located at grid point p, during the first step the following weighted average of $\mathcal{A}_p$ is calculated:

$$\bar{\mathcal{A}}_p = \frac{1}{4}\mathcal{A}_{p-1} + \frac{1}{2}\mathcal{A}_p + \frac{1}{4}\mathcal{A}_{p+1}, \tag{2.18}$$

where $\mathcal{A}_{p-1}$ and $\mathcal{A}_{p+1}$ is the value of the plasma variable $\mathcal{A}$ at the grid point $p-1$ and $p+1$, respectively. The second step involves a second weighted average that gives the final value of $\mathcal{A}_p$

$$\mathcal{A}_p = (1 - \alpha_s)\mathcal{A}_p + \alpha_s\bar{\mathcal{A}}_p. \tag{2.19}$$

Here, α_s is known as the smoothing parameter, and controls the level of diffusion used to stabilise the simulations [Müller et al., 2011].

2.3 Benchmark tests

In order to assess the quality of the numerical schemes used in PROMETHEUS++, hybrid simulations of well understood plasma phenomena that can be studied using one-dimensional plasma simulations were performed. The following sections present the results of benchmarking PROMETHEUS++ against three well known problems in plasma physics: the warm plasma dispersion relation, the resonant electromagnetic ion-ion instability and the electromagnetic ion cyclotron beam anisotropy.

2.3.1 Warm plasma dispersion relation

In the absence of external perturbations, the plasma should remain stable and only natural modes of the plasma should occur due to small thermal fluctuations within the plasma. We study two scenarios for an electron-proton plasma where these natural modes occur, namely, when these transverse electromagnetic waves propagate perpendicular ($\boldsymbol{k} \perp \boldsymbol{B}_0$) and parallel ($\boldsymbol{k} \parallel \boldsymbol{B}_0$) to the background magnetic field. Here, $\boldsymbol{k}$ and $\boldsymbol{B}_0$ are the wavevector (also known as propagation vector) and background magnetic field, respectively. In the strictly perpendicular propagation case the modes that naturally occur in the plasma are: the magnetosonic wave and cyclotron waves [Goldston and Rutherford, 1995; Stix, 1992]; while in the strictly parallel propagation case are: the ion cyclotron wave and the whistler wave [Goldston and Rutherford, 1995; Stix, 1992].

We perform hybrid simulations of an electron-proton warm plasma in order to recover the natural modes of the plasma for each case discussed above. For both simulations we use the following plasma parameters: electron plasma beta $\beta_e \equiv 2\mu_0 n_0 T_e / B_0^2 = 1$, proton plasma beta $\beta_p \equiv 2\mu_0 n_0 T_p / B_0^2 = 0.01$, background magnetic field $B_0 = 1.37 \times 10^{-7}$ T, and plasma density $n_0 = 10^{10}$ cm^{-3}.

Regarding the simulation parameters, we have used 1000 super-particles per cell in each case, with a simulation domain of length $L = 102.4 d_p$ divided into 1024 grid cells for the parallel propagation case, and a simulation domain length $L = 51.2 d_p$ divided into 1024 grid cells for the perpendicular propagation case. Here, $d_p = c/\omega_p$ is the proton skin depth, c is the light speed in vacuum, and ω_p is the proton plasma frequency. This means that the width of each grid cell is $\Delta x = r_p$ for the case with $\boldsymbol{k} \parallel \boldsymbol{B}_0$, and $\Delta x = 0.5 r_p$ for the case with $\boldsymbol{k} \perp \boldsymbol{B}_0$. Here, $r_p = d_p \sqrt{\beta_p}$ is the proton gyro-radius. For these simulations, the smoothing parameter is set to $\alpha_s = 7.5 \times 10^{-3}$ and $\alpha_s = 10^{-3}$, for $\boldsymbol{k} \parallel \boldsymbol{B}_0$ and $\boldsymbol{k} \perp \boldsymbol{B}_0$, respectively. For the parallel and perpendicular propagation cases we ran the corresponding simulation for 47 proton gyro-times ($t\Omega_p = 47$) and 50 proton gyro-times ($t\Omega_p = 50$), respectively.

In Fig. 2.8(a) the power spectral density in the frequency-wavenumber space of the electric field component E_y for the hybrid simulation with $\boldsymbol{k} \perp \boldsymbol{B}_0$ is shown. We observe the excitation of the magnetosonic wave along with cyclotron waves up to the sixth proton cyclotron harmonic ($\omega/\Omega_p = 6$). Similarly, in Fig. 2.8(b) we show the power spectral density of E_y for the hybrid simulation with $\boldsymbol{k} \parallel \boldsymbol{B}_0$. In this case, we identify the excited electromagnetic waves as the whistler wave and ion cyclotron wave.
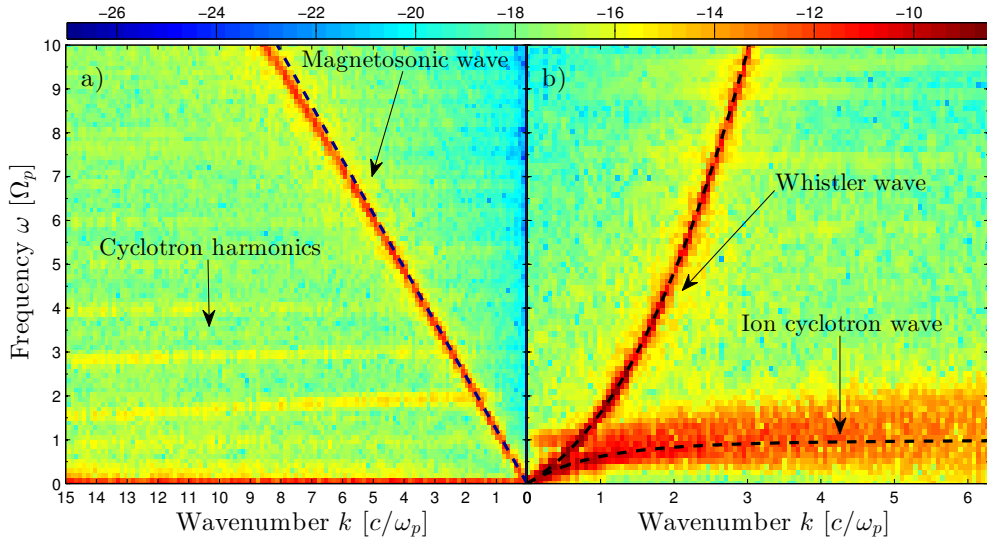
Figure 2.8: Dispersion relation of a warm electron-proton plasma. Panel a): power spectral density of the electric field component E_y for the hybrid simulation with $\boldsymbol{k} \perp \boldsymbol{B}_0$. We identify the excited electromagnetic waves as the magnetosonic and cyclotron waves up to the sixth proton cyclotron harmonic. Panel b): same as panel a) for the simulation with $\boldsymbol{k} \parallel \boldsymbol{B}_0$. In this case, we identify the excited electromagnetic waves as the whistler wave and ion cyclotron wave. The dashed lines in both panels show the analytic dispersion relation of a cold electron-proton plasma with the same plasma parameters used in the simulations.

Regarding energy conservation, both hybrid simulations show a transient phase where the plasma finds its equilibrium and continues to self-consistently evolve. After this transient time, the total energy of the simulation with $\boldsymbol{k} \perp \boldsymbol{B}_0$ oscillates and grows by 2.3% of its initial value by the end of the simulation. For the simulation with $\boldsymbol{k} \parallel \boldsymbol{B}_0$ we find a similar behavior, in this case the total energy grows by 2% of its initial value, this time due to intense short-wavelength (whistler) waves that would otherwise be damped by electron inertia effects, which are not included in the hybrid approximation for the plasma; instead, these short-wavelength modes are damped using numerical diffusion in our simulations (c.f. Sec. 2.2.4).

2.3.2 Resonant electromagnetic ion-ion instability

Resonant electromagnetic ion-ion instability (REIII) occurs when a low-density beam of ions streams along the background magnetic field $\boldsymbol{B}_0$ with respect to the slower background ions, with relative velocity $V_r > V_A$. Here, $V_A = B_0/\sqrt{\mu_0 n_0 m_i}$ is the Alfvén velocity, m_i is the mass of the background ions, $n_0 = Z_i n_i + Z_b n_b$ is the total ion density, n_b and n_i are the beam and background ion number density, and Z_i and Z_b are the atomic numbers of the beam and background ion species, respectively. When there is no net current in the system and we consider a frame of reference where the neutralizing electron background is at rest, the ion beam velocity is given by

$$\frac{\boldsymbol{V}_b}{V_A} = (1 - f) V \hat{\boldsymbol{b}}. \tag{2.20}$$

where $f = n_b/n_0$, $\hat{\boldsymbol{b}} = \boldsymbol{B}_0/B_0$ is the unit parallel vector, and $V = V_r/V_A$. In this frame of reference the background ions drift with mean velocity

$$\frac{\boldsymbol{V}_i}{V_A} = -\frac{f}{1 - f} V \hat{\boldsymbol{b}}. \tag{2.21}$$

The linear dispersion relation for electromagnetic waves propagating along the background field in the cold plasma limit is [Sharer and Trivelpiece, 1967]

$$\omega^2 - k^2 c^2 - \sum_j \frac{\omega_j^2 (\omega - kV_j)}{\omega - kV_j \pm \Omega_j} = 0, \tag{2.22}$$

where $\omega = \omega_r + i\gamma$ is the complex wave frequency, k is the wavenumber, $\omega_j^2 = n_j q_j^2/m_j \epsilon_0$ and $\Omega_j = q_j B_0/m_j$ are the plasma and cyclotron frequencies, c is the speed of light in vacuum, and $q_j = e Z_j$ is the electric charge of species j, where j can refer to electrons (e), beam ions (b) or background ions (i). Here, the $+(-)$ sign refers to right (left) hand polarized waves, respectively.

It is found that the REIII occurs when right hand polarized waves propagating along $\boldsymbol{B}_0$ resonate with the ion beam, that is,

$$\omega - kV_b + \Omega_b \approx 0. \tag{2.23}$$

Notice that in the frame of reference of the beam ($\omega = kV_b$) these waves are left hand polarized waves, that is, ion cyclotron waves; but in the electron frame of reference they are right hand polarized waves. In the limit case of a super-Aflvénic ($V_b/V_A \gg 1$), low-density ($n_b/n_0 \ll 1$) ion beam the dispersion relation of Eq. 2.22 can be solved analytically. In this limit the linear growth rate of the more unstable

mode of the REIII is approximately [Winske and Leroy, 1984]:

$$\frac{\gamma_m}{\Omega_b} \approx \left(\frac{f}{2}\right)^{1/3}, \tag{2.24}$$

occurring at wave number:

$$\frac{k_m V_A}{\Omega_b} \approx \frac{1}{V}. \tag{2.25}$$

A hybrid simulation of the REIII using PROMETHEUS++ for the case where both the ion beam and background ions are protons, that is, $Z_i = Z_b = 1$ and $\Omega_b = \Omega_i$, was performed. The plasma parameters are chosen to be the same as in Winske and Omidi [1993], that is, the ratio of the ion beam number density to the total ion density number density is $f = 0.015$, the beam velocity is $V_b/V_A = 10$, the plasma beta of each species is unity, $\beta_j \equiv 8\pi n_0 T_j/B_0^2 = 1$, and $\omega_i/\Omega_i = 10^4$. Here, T_j is the temperature of species j where $j = e, i, b$. The value of the total number density is a free parameter in this case and it is set to $n_0 = 10^{10}$ cm^{-3}. The simulation parameters are chosen such that the simulation domain has a length $L = 512d_p$ divided into 512 grid cells, that is, each cell grid has a length of d_p, where $d_p = c/\omega_i$ is the proton skin depth. We use 90 super-particles per cell for each proton population, the beam ions and the background ions, which initially are uniformly randomly distributed along the simulation domain, and have a thermalized distribution in velocity space with a drift along $\boldsymbol{B}_0$ given by V_i for the background ions, and V_b for the beam ions. In this simulation the background magnetic field $\boldsymbol{B}_0$ is parallel to the simulation domain. The smoothing parameter is set to $\alpha_s = 10^{-6}$.

The top panel of Fig. 2.9 shows the real frequency $\omega_r(k)$ and linear growth rate $\gamma(k)$ of the unstable modes of the REIII as predicted by the linear theory. For the plasma parameters used in this hybrid simulation, Eq. (2.24) and (2.25) predict that the maximum growth rate $\gamma_m/\Omega_i \approx 0.19$ peaks at wavenumber $k_m c/\omega_i \approx 0.1$. As a first numerical check for PROMETHEUS++, we calculate the power spectral density in wavenumber space of the magnetic field perturbations as function of time, this allows us to identify the excited modes in our hybrid simulation. We plot the power spectral density of the fluctuations of the magnetic field component B_z in the bottom panel of Fig. 2.9, which shows the excitation of a broadband spectrum of electromagnetic waves in the range of wavenumbers $0.05 \leq kc/\omega_i \leq 0.15$ with a peak value at $kc/\omega_i = 0.11 \pm 0.01$ (vertical dashed line of bottom panel), consistent with predictions of the linear theory of the REIII.

46
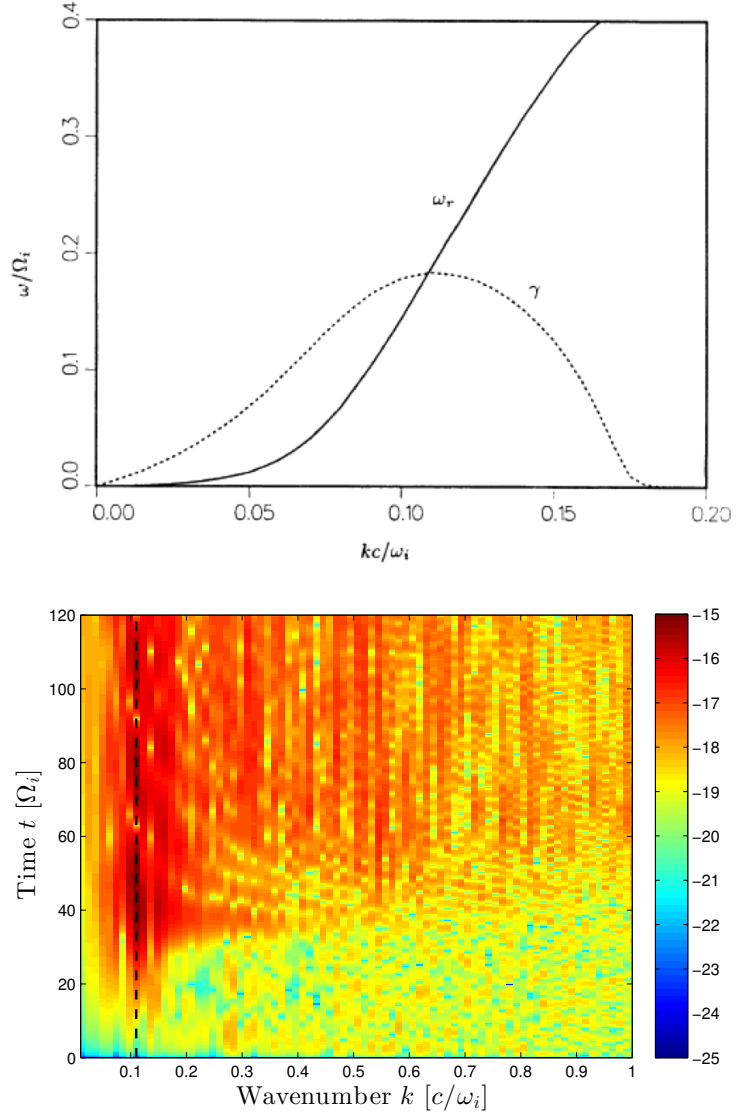
Figure 2.9: Comparison between theory and simulation results. Top panel: Figure reproduced from Winske and Omidi [1993]. Linear growth rates of unstable modes of the resonant electromagnetic ion-ion instability (REIII). The solid and dotted trace show the real frequencies ω_r and linear growth rates γ of the REIII as function of the wavenumber k, respectively. The value of the plasma parameters used for this plot are the same as the ones used in the hybrid simulation of the REIII. Bottom panel: shading indicates the $\log_{10}$ of the power spectral density in wavenumber space of the perturbations of the magnetic field component B_z as function of time. We observe the excitation of a broadband spectrum of electromagnetic waves in the range of wavenumbers $0.05 \leq kc/\omega_i \leq 0.15$ with peak value at $kc/\omega_i = 0.11 \pm 0.01$ (vertical dashed line), in good agreement with the predictions of the linear theory (top panel). Around $t\Omega_i = 35$ the nonlinear stage of the REIII takes over, at this stage modes with large amplitudes and with wavenumbers $kc/\omega_i > 0.15$ are excited.

47

Next, we calculate the linear growth rate of the most unstable mode in this hybrid simulation of the REIII. For this, we calculate the time evolution of the normalized magnetic energy density of this mode $\delta B_m^2(t)/B_0^2$, this is shown in Fig. 2.10(b). Then, we perform a linear fit of $\log_{10}\left(\delta B_m^2/B_0^2\right)$ vs t to calculate its linear growth rate γ, which is shown in Fig. 2.10(a). For this mode we find a linear growth rate of $\gamma/\Omega_i = 0.159 \pm 0.001$, which is in good agreement with the predicted value of Eq. (2.24), $\gamma_m \approx 0.19$. The difference between the predicted and the simulation value of this linear growth rate might be due to nonlinear interactions of this mode with the other unstable modes with similar amplitude excited around k_m. Additionally, we can estimate the oscillation frequency ω_r of this mode by looking at the quasi-periodic oscillations of $\delta B_m^2(t)/B_0^2$ in Fig. 2.10(b). From this figure, we estimate $\omega_r/\Omega_i \approx 0.21$, in good agreement with the linear theory (c.f. top panel of Fig. 2.9).
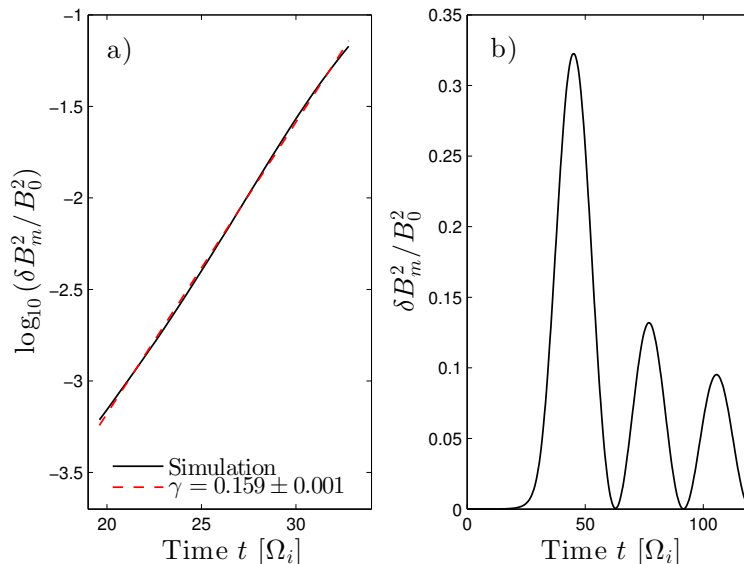
Figure 2.10: Calculation of the linear growth rate of the most unstable mode in the hybrid simulations of the REIII. Panel a): linear fit of $\log_{10}\left(\delta B_m^2/B_0^2\right)$ vs t. The solid (dashed) line shows the numerical data (linear fit). We find $\gamma/\Omega_i = 0.159 \pm 0.001$ for this mode, which is in good agreement with the linear theory. Panel b): normalised energy density of the most unstable mode in the simulation. We estimate an oscillation frequency of $\omega_r \approx 0.21$ for this mode.

Regarding the energy conservation in this simulation, the total energy oscillates between -0.4% to 0.6% of its initial value.

2.3.3 Electromagnetic ion cyclotron beam anisotropy

As a final numerical check for PROMETHEUS++, the electromagnetic ion cyclotron beam anisotropy instability (EICBAI) is studied. As the resonant electromagnetic ion-ion instability, this instability is also driven by an ion beam and can be studied as a special case of the REIII. For the case of the EICBAI the ion beam is dense ($n_b/n_0 \sim 0.1$) and streams at slower velocities ($V_b \leq V_A$) with respect to the background ions.

A hybrid simulation of the EICBAI with the following plasma parameters is performed: both ion species are protons, the ratio of the beam number density to the total ion density is $n_b/n_0 = 0.1$, the beam velocity is set to zero $V_b = 0$, $\beta_{b\parallel} \equiv 2\mu_0 n_0 T_{b\parallel}/B_0^2 = 10$, the temperature anisotropy of the beam ions is $T_{b\perp}/T_{b\parallel} = 5$, and $\beta_i = \beta_e = 1$. Here, $T_{b\parallel}$ and $T_{b\perp}$ refer to the parallel and perpendicular temperature of the beam ions, respectively. The background ions are initially thermalised. As for the simulation of the REIII, $\omega_i/\Omega_i = 10^4$ and $n_0 = 10^{10}$ cm^{-3}. On the other hand, the numerical parameters of this simulation are: a simulation domain length $L = 256 d_p$ divided into 256 grid cells, 200 super-particles per cell for each proton population. Both proton populations initially are uniformly randomly distributed along the simulation domain. The smoothing parameter for this simulation is set to $\alpha_s = 5 \times 10^{-7}$.

The top panel of Fig. 2.11 shows the theoretical prediction of the real frequency $\omega_r(k)$ and the linear growth rate $\gamma(k)$ of the unstable modes of the EICBAI for the plasma parameters used in the simulation. The bottom panel of Fig. 2.11 shows the power spectral density in wavenumber space of the fluctuations of the magnetic field component B_Z. This plot shows the excitation of a broadband spectrum of waves in the range of wavenumbers $0.1 \leq kc/\omega_i \leq 0.6$, with the most unstable mode occurring at $kc/\omega_i = 0.36 \pm 0.03$, consistent with theoretical predictions (c.f. top panel of Fig. 2.11).

Now, we calculate the linear growth rate of the most unstable mode found in our simulation of the EICBAI. For this, we use the normalized magnetic energy density of this mode $\delta B_m^2(t)/B_0^2$, which is shown in Fig. 2.12(b). Then, we perform a linear fit of $\log_{10}\left(\delta B_m^2/B_0^2\right)$ vs t, shown in Fig. 2.12(a), which gives a linear growth rate of $\gamma = 0.19 \pm 0.01$. This result is in good agreement with the linear theory of Fig. 2.11.

Regarding the energy conservation in this simulation, the total energy oscillates between -0.3% to 0.1% of its initial value.
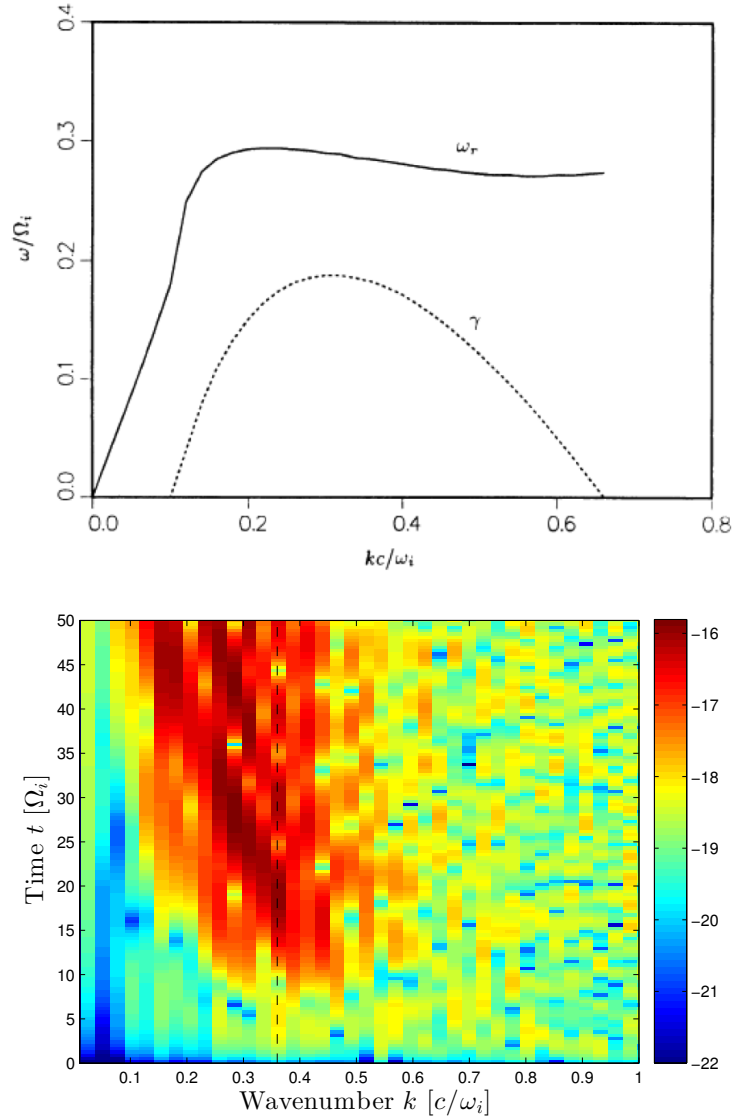
Figure 2.11: Comparison between theory and simulation results. Top panel: Figure reproduced from Winske and Omidi [1993]. Linear growth rates of unstable modes of the electromagnetic ion cyclotron beam anisotropy instability (EICBAI). The solid and dotted lines show the real frequencies ω_r and linear growth rates γ of the EICBAI as a function of the wavenumber k, respectively. The values of the plasma parameters used for this plot are the same as the ones used in the hybrid simulation of the EICBAI. Bottom panel: shading indicates $\log_{10}$ of the power spectral density in wavenumber space of the perturbations of the magnetic field component B_z as function of time. We observe the excitation of a broadband spectrum of electromagnetic waves in the range of wavenumbers $0.1 \leq kc/\omega_i \leq 0.6$ with peak value at $kc/\omega_i = 0.36 \pm 0.03$ (vertical dashed line), consistent with predictions of the linear theory (top panel).
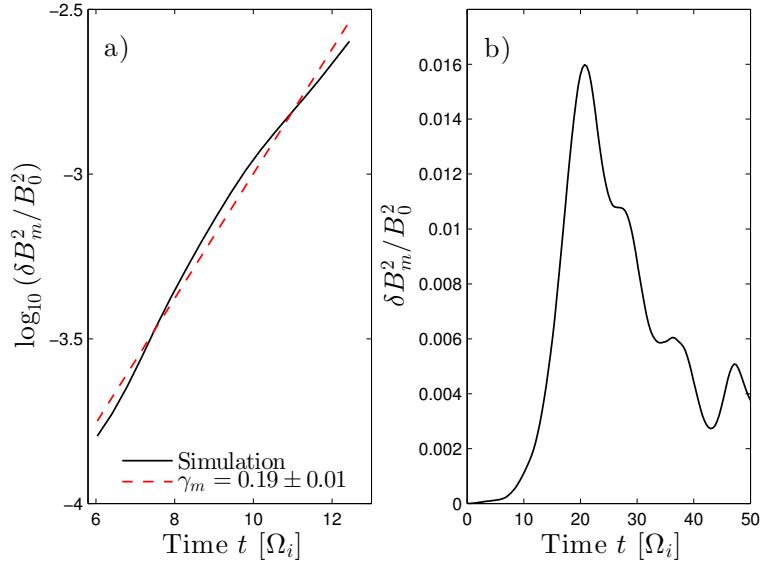
Figure 2.12: Calculation of the linear growth rate of the most unstable mode in the hybrid simulations of the EICBAI. Panel a): linear fit of $\log_{10}\left(\delta B_m^2/B_0^2\right)$ vs t. The solid (dashed) line shows the numerical data (linear fit). We find $\gamma/\Omega_i = 0.19 \pm 0.01$ for this mode. Panel b): normalised energy density of the most unstable mode in the simulation.

2.4   Discussion

This chapter has introduced PROMETHEUS++, a new parallel code written in C++ that solves the equations of the plasma in its hybrid approximation, where ions are treated as kinetic particles and electrons as a charge neutralizing massless fluid. Numerical schemes used to solve the equations of the plasma are presented, as well as the charge assignment and force interpolation scheme used to self-consistently couple the computational particles (super-particles) to the electromagnetic fields.

The accuracy and stability of PROMETHEUS++ was tested by performing simulations of three well known phenomena in plasma physics: the warm plasma dispersion relation, the resonant electromagnetic ion-ion instability and the electromagnetic ion cyclotron beam anisotropy. The results of these benchmark tests can be summarised as follows: first, in the simulations of quiet warm plasma the natural modes of the plasma arising due to small thermal fluctuations of the plasma were recovered; namely, the ion cyclotron and whistler waves, when the the propagation vector of these waves is parallel to the background magnetic field; and the magnetosonic and cyclotron waves, when the propagation vector is perpendicular to the background magnetic field. Second, in the simulation of the resonant electromagnetic ion-ion instability we found good agreement between the predictions of the

51

linear theory and the simulation of this instability, specifically, the localisation in frequency and wavenumber space of the most unstable mode of this instability is in agreement with the linear theory. Finally, we simulated the electromagnetic ion cyclotron beam anisotropy for which simulations results, as in the previous benchmark test, match well to the predictions of the linear theory. In all the simulations we observed an energy conservation within the range of -0.4% to 2.3% of the initial energy. These results suggest that PROMETHEUS++ is robust and can be used with confidence to study the dynamics of energetic ions in fusion and space plasmas.

Future work for further developing PROMETHEUS++ includes the extension to three dimensions in physical space, and the inclusion of toroidal geometry for performing more realistic simulations of magnetic confinement fusion plasmas. We anticipate that the latter will require the development of new numerical schemes for solving the electromagnetic fields and for the charge assignment and force interpolation scheme, as well as the inclusion of non-periodic boundary conditions.

Chapter 3

Hybrid simulations of the MCI in relation to ICE in D-T JET plasmas

3.1 Introduction

Fusion power from magnetically confined plasmas will rely on self-sustained nuclear burning, where the output power is greater than the power used to confine and heat the plasma. This will require fusion-born ions produced primarily in the core plasma to deliver their energy to the thermal plasma through collisional processes, while remaining magnetically confined [Heidbrink and Sadler, 1994]. For this reason, it is important to develop diagnostics for monitoring the confinement and evolution of the fusion-born ions population in future deuterium-tritium (D-T) plasma experiments in JET and ITER. Among the leading candidates for this role [McClements et al., 2015] is ion cyclotron emission (ICE), which is a collective radiative instability driven by fusion-born ions, or by other energetic ion populations. ICE was initially observed in pure deuterium plasmas in JET when Ohmic heating and hydrogen neutral-beam injection (NBI) were used to heat the plasma [Cottrell and Dendy, 1988; Schild et al., 1989]. Subsequently, ICE was observed from D-T plasmas in the tokamak experiments JET and TFTR [Cottrell et al., 1993; Dendy et al., 1995; Cauffman et al., 1995; McClements et al., 1999], where ion cyclotron heating antennas in receiver mode and radio frequency probes were used to detect ICE, respectively. In both cases, a local minority population of fusion-born alpha-particles, super-Alfvénic in JET and sub-Alfvénic in TFTR, provided the free energy to drive the emission. The measured ICE spectra showed strong peaks at consecutive ion

cyclotron harmonics of alpha-particles, as evaluated at the outer mid-plane edge. Furthermore, the ICE intensity in JET and TFTR showed linear scaling with the measured neutron flux and with alpha-particle concentration [Cottrell et al., 1993; Dendy et al., 1995; McClements et al., 1996]. In the first studies of ICE in JET, a strong correlation between ICE and MHD activity was observed [Schild et al., 1989; Cottrell et al., 1993], and ICE is used in the DIII-D tokamak to diagnose energetic ion loss due to MHD activity [Watson and Heidbrink, 2003; Heidbrink et al., 2011]. This suggests that ICE might be exploited as a complementary diagnostic for MHD activity, as well as for fusion-born alpha-particle dynamics, in future D-T plasmas in JET and ITER [McClements et al., 2014, 2015]. Studies of ICE in JT-60U [Ichimura et al., 2008; Sato et al., 2010] and ASDEX-Upgrade [D'Inca et al., 2011; D'Inca, 2014] have extended the understanding of the dependence of ICE on different plasma parameters and on NBI parameters.

Future exploitation of ICE as a diagnostic will rest on fully understanding the underlying physics of the emission mechanism. The leading candidate is the magnetoacoustic cyclotron instability [Belikov and Kolesnichenko, 1976] (MCI), for which the analytical theory was developed and applied to scenarios relevant to JET and TFTR soon after the experimental observations in these tokamaks [Dendy et al., 1992, 1993, 1994b; Fülöp and Lisak, 1998]. The analytical theory of the MCI approximates the velocity distribution function of the fusion-born alpha-particles driving the instability as a drifting ring-like distribution. This reflects the naturally occurring population inversion in the velocity distribution of centrally-born alpha-particles at the outer mid-plane edge, which have undergone large excursions from the core to the edge plasma in JET and TFTR [Cottrell et al., 1993; Dendy et al., 1995]. Among the predictions of the analytical theory of the MCI in relation to ICE in JET and TFTR we can mention: the excitation of waves on the fast Alfvén-ion Bernstein branch at sequential alpha-particle cyclotron harmonics; strong linear growth rates of waves propagating almost perpendicular to the background magnetic field; and linear scaling of these growth rates with alpha-particle concentration at low cyclotron harmonics. The success of linear theory, which by construction only addresses the early stage of growth, in explaining observed ICE signal intensities, remained a paradox which has been partly resolved by the recent computational studies reported in Cook et al. [2013]. These studies were the first fully self-consistent particle-in-cell (PIC) simulations of the MCI [Cook et al., 2013], which validated the assumptions and predictions of linear theory, and showed good agreement with the properties of ICE measurements in JET. The work of Cook et al. [2013] suggested that the congruence between linear theory and the observed

signal intensities may reflect the prompt self-disruption, in velocity space, of the driving population by the waves which it excites. The full kinetics of both the electron population and the multiple ion populations was included in the PIC model of Cook et al. [2013], and the inclusion of electron spatio-temporal scales imposed computational constraints on run time.

In this chapter we report the results of numerical simulations of the MCI using the hybrid approximation for the plasma (c.f. Sec. 1.2). This approximation allows us to progress through the linear phase and far into the nonlinear phase of the MCI, which in turn allow us to unveil novel nonlinear processes of the MCI that produce a better match to observation of ICE in D-T JET plasmas. We report, in particular, significantly improved agreement between simulated and observed ICE spectra at low cyclotron harmonics, nonlinear re-energisation of the alpha-particles by waves excited early on in the simulations by the alpha-particles, and linear scaling of the MCI-generated electromagnetic field intensities with alpha-particle concentration, in agreement with the experimental observations of ICE. In addition, we find that linear growth rates inferred from hybrid simulations of the MCI at early times, show square root scaling with alpha-particle concentration in the range of frequencies $9\Omega_\alpha \leq \omega \leq 12\Omega_\alpha$, where Ω_α is the alpha-particle cyclotron frequency. The mode at $\omega = 7\Omega_\alpha$, which is marginally resolved in our hybrid simulations, shows linear scaling with alpha-particle concentration. Finally, we perform simulations of the MCI for conditions relevant to core D-T JET plasmas. We find that the MCI only can operate under these plasma conditions, heating efficiently the background deuterons, if the velocity distribution of fusion-born alpha-particles departs significantly from an isotropic velocity distribution.

3.2   Hybrid simulations of the MCI

We perform 1.5D numerical simulations of the MCI in the hybrid approximation, taking the direction of variation along the x-axis to be perpendicular to the constant background magnetic field $\boldsymbol{B}_0 = B_0\hat{\boldsymbol{z}}$. Following Cook et al. [2013], we initialise with an isotropic, thermal distribution of deuterons with initial temperature 1 keV, and a ring-like distribution of minority alpha-particles, $f_\alpha(v_\parallel, v_\perp) = \delta(v_\parallel)\delta(v_\perp - u_\perp)$ at 3.5 MeV. Here $u_\perp$ is the magnitude of the initial perpendicular velocity of the alpha-particles, and the population is randomly uniformly distributed in initial gyro-angle. This distribution function corresponds to a simplified version of the one used in the analytical theory of the MCI in McClements et al. [1996]

$$f = \frac{1}{2\pi^{3/2}u_\perp v_r} \exp\left(-\frac{(v_\parallel - v_d)^2}{v_r^2}\right)\delta(v_\perp - u_\perp), \qquad (3.1)$$

for the case where the ion distribution has zero parallel velocity, $v_\parallel = 0$, zero velocity spread, $v_r = 0$, and is centred on zero, $v_d = 0$.

In order to compare the results of our hybrid simulations with the ICE measurements, we set up values for the plasma parameters similar to those used in pulse 26148 in the preliminary tritium experiment (PTE) in JET (c.f. Table I of Cottrell et al. [1993]). The total number density in Eq. (1.15) and the electron temperature are set to $n = 10^{19}$ m^{-3} and $T_e = 1$ keV, respectively. The strength of the background magnetic field corresponds to the value at the outer midplane in JET, $B_0 = 2.1$ T. The ratio of the minority alpha-particle number density to the deuteron number density, $\xi_\alpha = n_\alpha/n_D$, which determines the growth rate of the excited waves in the linear theory of the MCI [Dendy et al., 1995], takes the value $\xi_\alpha = 10^{-3}$ unless otherwise indicated. Our simulations do not take into account the collisional slowing-down of the alpha-particles, nor replenishment by freshly born particles. Thus we focus exclusively on the fast timescale self-consistent physics of the MCI of a given energetic population, in both linear and nonlinear phases. As we shall see, our simulations reproduce the observed properties of ICE, suggesting that the relevant ion kinetic processes are captured in these simulations and in this simplified spatial topology with spatially homogeneous plasma.

The large simulation domain consists of 8192 equal grid cells, each of length equal to $r_D/\sqrt{2}$, where $r_D = v_{T_D}/\Omega_D$ is the deuteron Larmor radius, $v_{T_D}^2 = k_B T_D/m_D$ is the deuteron thermal velocity, and Ω_D is the deuteron ion cyclotron frequency. This enables us to resolve in detail the alpha-particle gyrodynamics ($r_{L_\alpha}/r_{L_D} \approx 41$), while also providing adequate coverage of the deuteron gyromotion. We obtain high resolution in wavenumber space due to the large number of modes present in the simulation domain, which enables calculation of high resolution fast Fourier transforms. For each ion species, we use 200 super-particles per grid cell, and the smoothing parameter is set to $\alpha_s = 10^{-4}$.

In Fig. 3.1(c) we show the power spectra of the hybrid simulation for the linear (black trace) and nonlinear (red trace) stages. These are calculated by integrating the frequency-wavenumber space over the positive wavenumber domain $k > 0$. For the calculation encompassing the linear (nonlinear) stage we use simulation data from the time interval $t/\tau_\alpha = 1$ to $t/\tau_\alpha = 5$ ($t/\tau_\alpha = 1$ to $t/\tau_\alpha = 10$). Here τ_α is the alpha-particle gyroperiod. In the same figure are plotted for comparison: in panel (b), linear growth rates calculated from analytical theory, Eq. (8) of
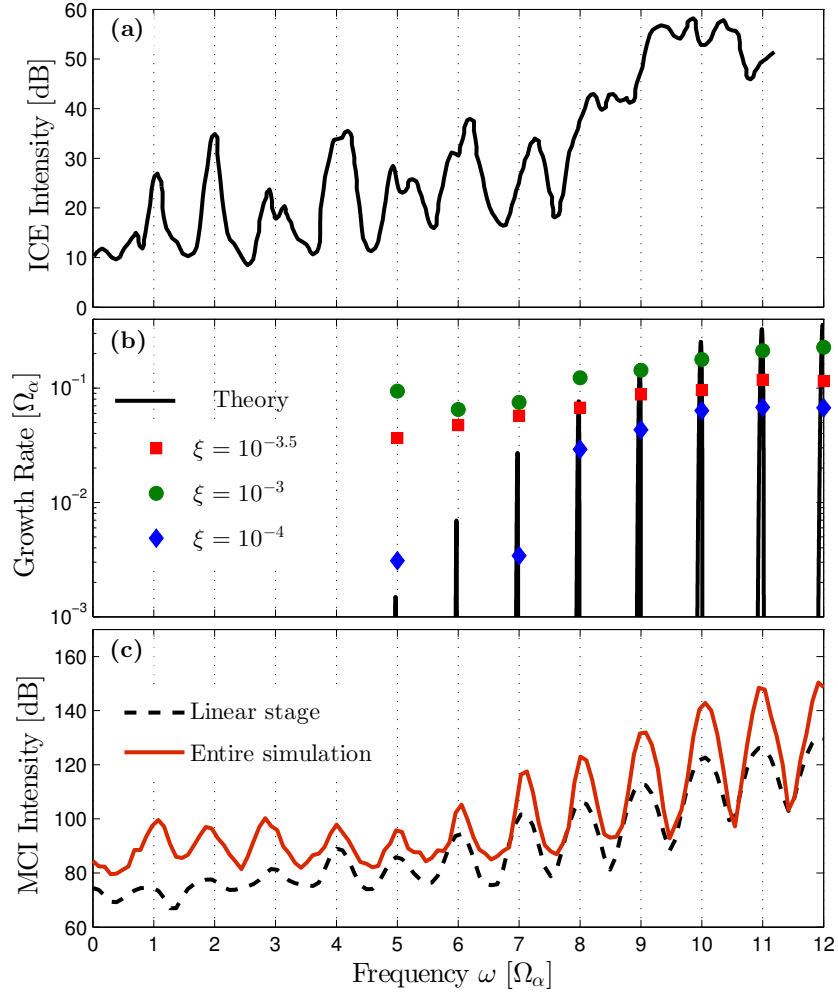
Figure 3.1: Experimental, analytical and numerical spectra. (a) measured ICE intensity from JET PTE pulse 26148 (Reproduced from Figure 1 of Dendy et al. [1995]). (b) analytical linear growth rate for the MCI for alpha-particle concentration, $\log_{10}(\xi_\alpha) = -3$, along with the corresponding results from the hybrid simulations for the three values, $\log_{10}(\xi_\alpha) = -4, -3.5, -3$. (c) intensity of the parallel perturbed magnetic field $\delta B_\parallel = B_z - B_0$ of the hybrid simulation of the MCI with $\xi_\alpha = 10^{-3}$. The dashed black (solid red) line represents the linear (nonlinear) stage of the instability.

McClements et al. [1996]; and in panel (a), the ICE intensity of pulse 26148 of the PTE in JET, which was measured using an ion cyclotron resonance heating (ICRH) antenna in receiver mode. The power spectrum of the simulation, and especially that encompassing the nonlinear phase of the MCI (red trace in Fig. 3.1(c)) recovers most of the observed features of the ICE signal Fig. 3.1(a). The intensity peaks appear at the same positions on the frequency axis, with the most intense peaks

occurring for $\omega/\Omega_\alpha \geq 8$. The dashed black trace in Fig. 3.1(c) represents the power spectrum of the linear stage of the MCI simulation, already showing several key features of the ICE signal. In this respect our hybrid simulation confirms previous analytical [Cauffman et al., 1995; McClements et al., 1996] and PIC computational [Cook et al., 2013] studies. In addition to the theoretically-predicted growth rate (Eq. (8) of McClements et al. [1996]), Fig. 3.1(b) also shows the growth rate obtained from the early phase of hybrid simulations for three different values of ξ_α. We note better agreement between these results for the harmonics $\omega/\Omega_\alpha \geq 7$ than for the lower excited harmonics in our simulations, down to $\omega = 5\Omega_\alpha$. Also, as predicted by the linear theory, the growth rates increase with the concentration of alpha-particles. The parameters used in the calculation of the analytical linear growth rate [McClements et al., 1996] are: an angle of propagation $\theta = 88°$, and a narrow spread of the parallel velocity of the minority alpha-particles, $v_r/u_\perp \approx 0.06$, which approximate the set-up of our simulations. Further hybrid simulations of the MCI for different propagation angles, $85° \leq \theta \leq 90°$, follow the predictions of the linear theory for the growth rates [McClements et al., 1996], decreasing as the propagation angle decreases whilst keeping constant the concentration of alpha-particles ξ_α.

Importantly, the fact that the hybrid model enables us to follow the MCI deep into its nonlinear phase enables this treatment to capture additional aspects of the observed ICE signal. Comparison of the two traces for the simulated MCI in Fig. 3.1(c) with the measured ICE signal in Fig. 3.1(a) shows that only the solid red trace, which encompasses the nonlinear phase, robustly captures the lower observed cyclotron harmonic peaks one to three, which appear to become unstable due to nonlinear interactions with modes excited in earlier times, as explained in the next section.

As we mentioned before, plasma heating by fusion-born ions requires the energetic alpha-particles to transfer their energy to the background electrons and ions. In Fig. 3.2 we show the time evolution of the change in particle energy density and the energy density of the excited electric and magnetic fields associated with the MCI. At $t/\tau_\alpha = 1$, the instability starts to take over. The free energy of the alpha-particles contributes to energising the background deuterons which oscillate in electromagnetic fields excited by wave-particle cyclotron resonance of the alpha-particles. This energy transfer to the deuterons peaks at $t/\tau_\alpha \approx 5$, giving way to the re-energisation of the alpha-particles which is discussed in Sec. 3.4.
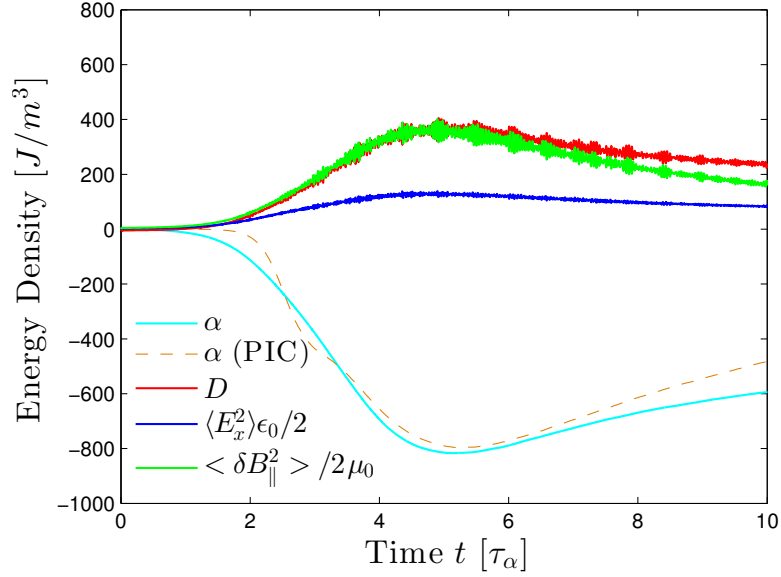
Figure 3.2: Time evolution of the change in particle energy density and energy density of the excited field components. The red (cyan) line shows the change in the kinetic energy density of the deuterons (alpha-particles) along with the energy density of the magnetic field perturbation, $\delta B_\parallel \equiv B_z(x,t) - B_0$, (green line) and the perpendicular electric field E_x (blue line). For comparison we show the change in kinetic energy density of the alpha-particles (orange dashed line) taken from a PIC simulation with the same parameters as our hybrid simulation. The temporal axis has been scaled by a factor of $1/2$ to account for the slower growth rate observed in the PIC simulations, which might be due to the fact that, opposite to our hybrid simulations, the PIC simulations include the full kinetic electron damping.

3.3 Electric and magnetic fields

We now turn to the time evolution of the electric and magnetic fields in the hybrid simulation of the MCI. Panels (a) and (d) of Fig. 3.3 plot $\log_{10}$ of the spectral density of the parallel perturbed magnetic field $\delta B_\parallel = B_z(x,t) - B_0$ in frequency-wavenumber space for the linear and nonlinear stages. The dashed lines in these panels show $\omega/k = V_A$, the dispersion relation of the fast Alfvén wave. We see that modes of the fast Alfvén wave are excited in the simulations at resonances with consecutive ion cyclotron harmonics of the alpha-particles. Panels (b) and (e) of Fig. 3.3 show a close-up of the most strongly excited modes for the linear and nonlinear stages, respectively. Here the intersection of the vertical and horizontal dashed lines indicates the maximum of the spectral density at $\omega/\Omega_\alpha \approx 11$ and $kV_A/\Omega_\alpha \approx 11.5$. Panels (c) and (f) show the time evolution in wavenumber space of the $\delta B_\parallel$ field component. This shows that the most strongly excited modes are in

the range $6 \leq kV_A/\Omega_\alpha \leq 13$, so that the characteristic length scales of these modes correspond to the initial gyroradius of the alpha-particles, $r_\alpha = u_\perp/\Omega_\alpha$.
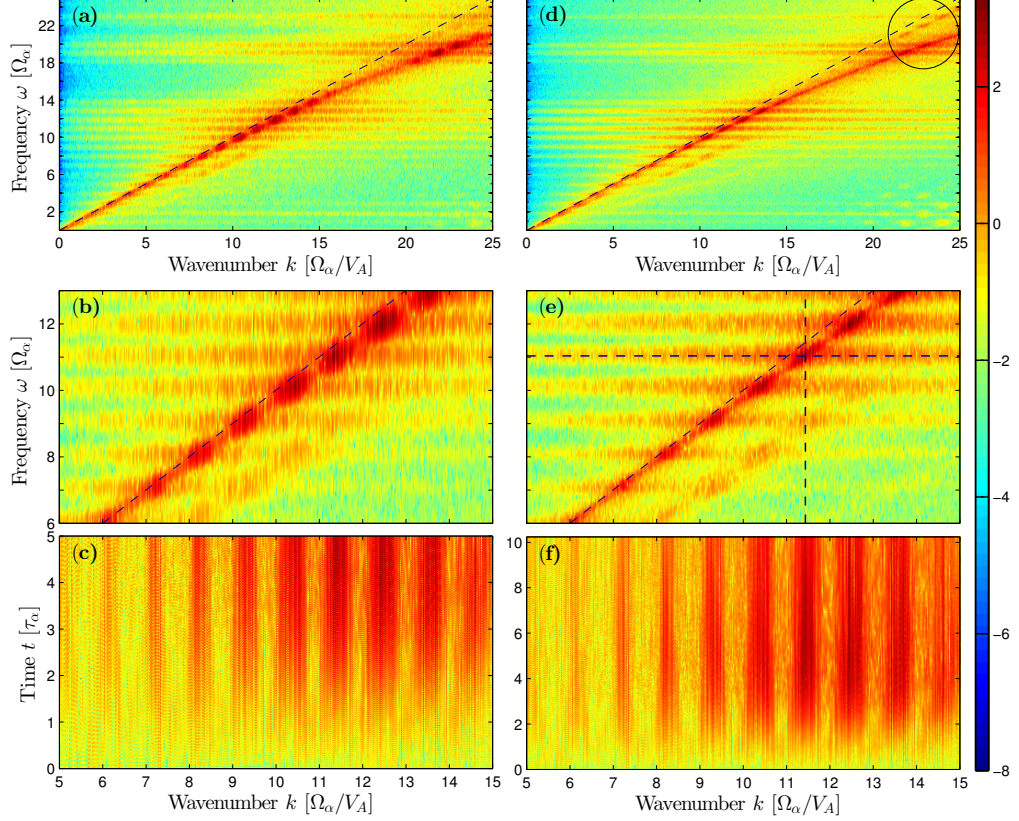
Figure 3.3: Frequency and wavenumber space for the linear (panels (a)–(c)) and nonlinear stages (panels (d)–(f)) of the MCI. Panels (a) and (d): shading indicating the $\log_{10}$ of the spectral density of the parallel perturbed magnetic field $\delta B_\parallel$ in frequency-wavenumber space. These plots show the excitation of the fast Alfvén wave with resonances at consecutive harmonics of ion cyclotron frequency, $\omega = \Omega_\alpha$. The dashed line shows, $\omega/k = V_A$, where $V_A = B_0/\sqrt{\mu_0 n_D m_D}$ is the Alfvén speed. The ellipse in (d) shows the excited modes due to the alpha-particles' re-energisation. Panels (b) and (e): close-up of the most strongly excited modes in frequency-wavenumber space. The intersection of the vertical and horizontal dashed lines in panel (e) points to the maximum of $\delta B_\parallel^2$ in frequency-wavenumber space at $\omega/\Omega_\alpha \approx 11$ and $kV_A/\Omega_\alpha \approx 11.5$. Panels (c) and (f): time evolution of the wavenumber spectra of $\delta B_\parallel$.

Figure 3.4 shows the contribution of each positive wavenumber ($k > 0$) to the energy density of the fields. Panels (a) and (b) of Fig. 3.4 plot this for the linear and nonlinear stages, respectively. For the calculation of the linear (nonlinear) stage we used simulation data from the time interval $t/\tau_\alpha = 1$ to $t/\tau_\alpha = 5$ ($t/\tau_\alpha = 1$ to $t/\tau_\alpha = 10$). We see spectra with consecutive intensity peaks in the range $6 \leq$

$kV_A/\Omega_\alpha \leq 13$, for all the the non-zero field components in our simulations. By comparing with panels (e) and (f) of Fig. 3.3, these intensity peaks can be identified with the resonances of the fast Alfvén wave at consecutive ion cyclotron harmonics of the alpha-particles. It is evident from Fig. 3.4 that $\delta B_\parallel$ contains more energy for the wavenumbers $kV_A/\Omega_\alpha < 13$ than the electric field component E_x. The inset in Fig. 3.4(a) shows the energy density of $\delta B_\parallel$ in the linear (orange) and nonlinear (green) stages in linear scale. The main difference between the linear and nonlinear stages is the higher energy of $\delta B_\parallel$ in the range $kV_A/\Omega_\alpha < 5$, which is not predicted by the linear theory of the MCI.
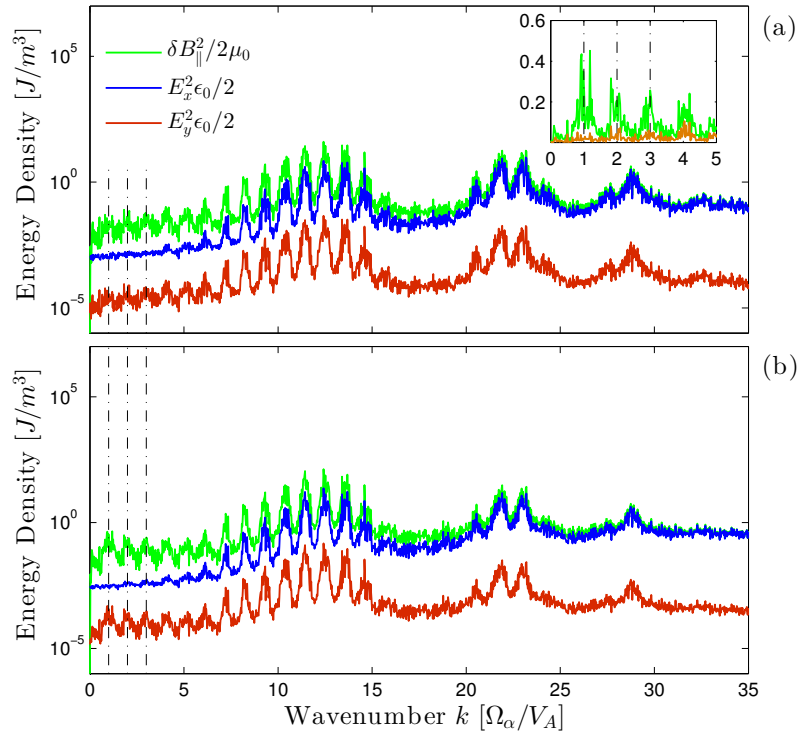
Figure 3.4: Energy density of each non-zero field component as a function of positive wavenumber ($k > 0$) in the linear (a) and nonlinear (b) stages. Strong localized peaks in the range $6 \leq kV_A/\Omega_\alpha \leq 13$ correspond to the resonances of the fast Alfvén wave at consecutive ion cyclotron harmonics of the alpha-particles. The inset in panel (a) shows the energy density of $\delta B_\parallel$ in the linear (orange) and nonlinear (green) stages in the range of wavenumbers $kV_A/\Omega_\alpha < 5$. Linear scale is used for the y-axis in this inset. The intensity peaks about $kV_A/\Omega_\alpha = 22$ are important in the re-energisation process for alpha-particles in the nonlinear stage (cf. Figs. 3.2 and 3.3(d)).

Let us now consider the interaction between the electric and magnetic fields that is mediated by the plasma. First, we calculate the spatial cross-correlation, over

an arbitrary separation Δx, between the normalised components $\delta B_\parallel(x,t)/\sqrt{2\mu_0}$ and $\sqrt{\epsilon_0/2}E_x(x,t)$

$$R(\Delta x, t) = \frac{1}{2}\sqrt{\frac{\epsilon_0}{\mu_0}} \int \delta B_\parallel(x + \Delta x, t) E_x(x,t)dx, \qquad (3.2)$$

where the integral is performed over the entire simulation domain. To construct the most appropriate corresponding phase shift, we calculate the phase shift between the field components

$$\Delta\phi = k^*\Delta x, \qquad (3.3)$$

where $k^* V_A / \Omega_\alpha \approx 11.5$ is the dominant wavenumber in our simulation. This enables us to transform from $R(\Delta x, t)$ to $R(\Delta\phi, t)$, which is plotted in Fig. 3.5. This shows that in the early stages of our simulation there is not a well defined phase shift between the electric and magnetic fields. However, as the simulation enters the nonlinear stage, the coupling between the fields produces a phase shift about $\Delta\phi \approx \pi$ for $t > 5\tau_\alpha$.
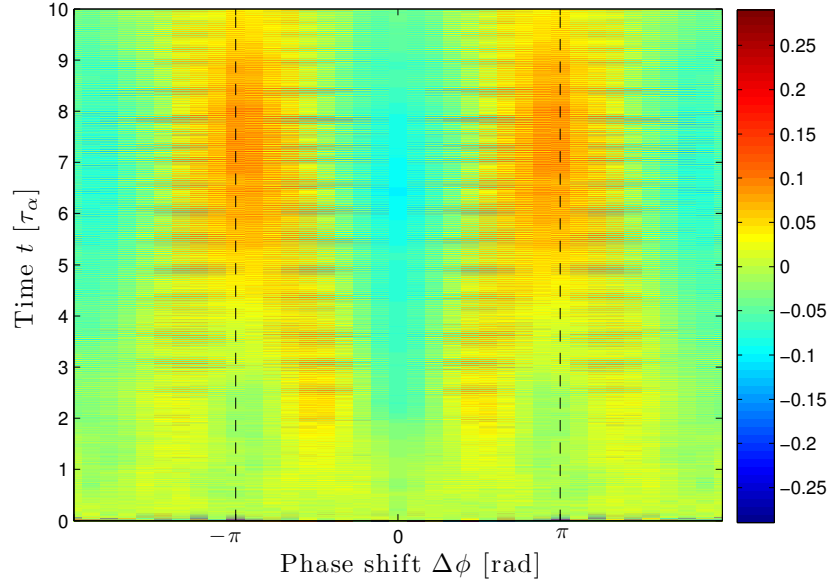
Figure 3.5: Spatial cross-correlation $R(\Delta\phi, t)$ (cf. Eq. (3.2) and (3.3)) between the normalised field components $\delta B_\parallel(x,t)/\sqrt{2\mu_0}$ and $\sqrt{\epsilon_0/2}E_x(x,t)$. The red (blue) colour indicates maxima (minima) of $R(\Delta\phi, t)$, indicating strong (lack of) correlation for the relative phase shift $\Delta\phi$. The vertical dashed lines show π and $-\pi$. The nonlinear interaction between the electric and magnetic fields produces a phase shift that remains almost constant at $\Delta\phi \sim \pm\pi$ for $t > 5\tau_\alpha$.

Let us now examine whether there is nonlinear coupling between the well-defined approximate normal modes at successive ion cyclotron harmonics that are found in the present simulation. It is of particular interest, and exploits the hybrid simulation approach, to compare any such coupling in the early and later stages of the MCI. An appropriate technique is bispectral analysis [Kim et al., 1980; Holland et al., 2002], which has been successfully applied to experimental measurements on magnetically confined plasmas as, for example, in Moyer et al. [2001] and Yamada et al. [2008]. For present purposes, this requires calculation of the non-normalised self-bicoherence of the parallel perturbed magnetic field $\delta B_\parallel$ in wavenumber space

$$b^2(k_1, k_2) = |\langle \delta\hat{B}_\parallel^*(k_1 + k_2)\delta\hat{B}_\parallel(k_1)\delta\hat{B}_\parallel(k_2)\rangle|^2, \qquad (3.4)$$

where $\delta\hat{B}_\parallel(k)$ is the Fourier transform of $\delta B_\parallel(x)$ and $\delta\hat{B}_\parallel^*(k)$ its complex conjugate. Here the average $\langle\cdot\rangle$ is taken over a small time window of width $\Delta t \sim 0.2\tau_\alpha$. We show this calculation in Fig. 3.6, where the shading indicates the intensity of coupling between different modes. The red colour indicates significant coupling between two different modes. We see strong coupling in the linear (Fig. 3.6(a)) and nonlinear (Fig. 3.6(b)) stages between modes about $(V_A/\Omega_\alpha)(k_1, k_2) = (10, 10)$ with less intense points about $(V_A/\Omega_\alpha)(k_1, k_2) = (10, 0)$ for the linear stage. However, in the nonlinear stage (cf. Fig. 3.6(b)) all the points around $kV_A/\Omega_\alpha = 10$ become equally intense, reflecting a more intense coupling between the relevant modes. These results may be extrapolated to the frequency domain by using the dispersion relation of panels (a) and (d) of Fig. 3.3.

3.4   Nonlinear stage of the MCI

Thus far, we have focused primarily on establishing congruence between our hybrid simulations of the MCI and three standards of previous research: observations of ICE [Heidbrink and Sadler, 1994; Cottrell and Dendy, 1988; Schild et al., 1989; Cottrell et al., 1993], linear analysis of the MCI [Dendy et al., 1995; McClements et al., 1996, 1999; Dendy et al., 1994b] and large scale numerical simulations of the MCI [Cook et al., 2013] using a PIC code which captures the full kinetics of ions and (unlike the hybrid model) electrons. We now turn to the key aspect of nonlinear phenomenology of the MCI, adumbrated in the preceding discussion of results, which can only be captured by a hybrid model given computational resource constraints. We focus first on the re-energisation of the alpha-particles visible in Fig. 3.2, commencing at $t/\tau_\alpha \approx 5$. In the time interval, $5 < t/\tau_\alpha < 7$, the energy of the background deuterons and the fields decreases gradually whilst the kinetic energy of the alpha-

63
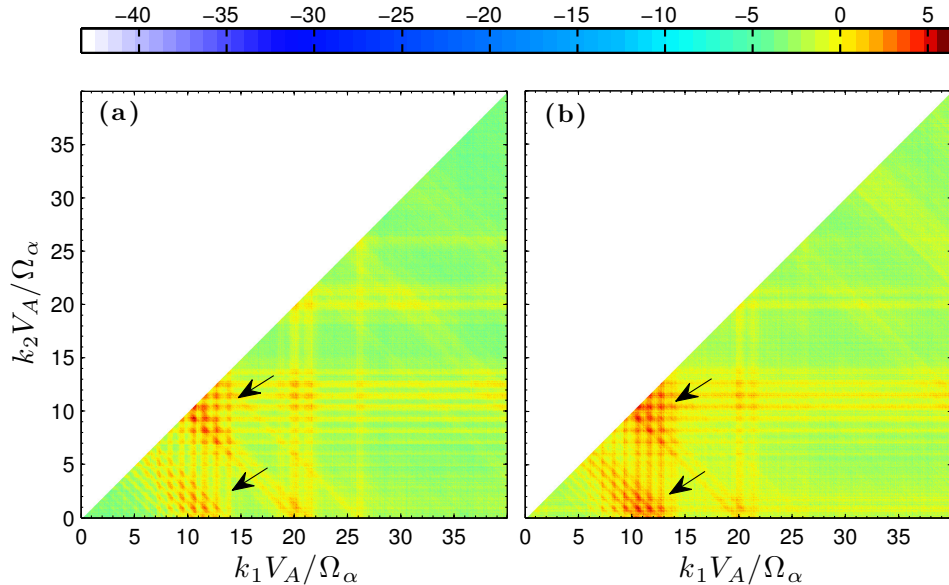
Figure 3.6: Non-normalized self-bicoherence of the parallel perturbed magnetic field $\delta B_\parallel$ in wavenumber space, plotted using a $\log_{10}$ colour scale. Only the principal domain of the self-bicoherence is shown. The red colour indicates significant coupling between different modes at k_1 and k_2. Panels (a) and (b) show the non-normalised self-bicoherence of $\delta B_\parallel$ in the linear stage at $t = 4\tau_\alpha$ and in the nonlinear stage at $t = 8\tau_\alpha$. The arrows in both panels point to areas on the $k_1 k_2$ plane which show strong coupling between different modes.

particle population reverses its previous decline. After this time, the background deuterons' energy remains approximately constant while the energy of the fields continues to decrease, being transferred to the alpha-particles as kinetic energy.

As a first step towards understanding this re-energisation process, we look at the velocity-position phase space of the alpha-particles, together with their velocity probability density function. In the right panel of Fig. 3.7 we show the smoothed, filled contours of the phase space of the alpha-particles at $t/\tau_\alpha \approx 9$, calculated by averaging over 16 windows of the phase space along the x-axis. The different colours here represent the value of $f_\alpha(x,v)$, where $v = \sqrt{v_x^2 + v_y^2}$ is the amplitude of the perpendicular velocity of the alpha-particles. Here, we do not include the parallel velocity v_z, which remains constant in time for the chosen initial condition. We compare $f_\alpha(x,v)$ with the left panel of Fig. 3.7, which shows $f_\alpha(v)$ at three different times. In the linear stage, $f_\alpha(v)$ seems to follow a biased diffusive process in velocity space, leading up to the early time at $t/\tau_\alpha \approx 5$. Then, as the instability enters the nonlinear stage, a bump in $f_\alpha(v)$ starts to build up at a velocity $v/V_A \approx 1.5$. Once this bump of re-energised alpha-particles forms, we can identify three corresponding

features in the phase space of Fig. 3.7, right panel: two phase space diffusion regions around $v/V_A \approx 1$ and $v/V_A \approx 1.5$ separated by a zone which acts as a leaky transport barrier, which produces the steep slope before the bump in $f_\alpha(v)$.
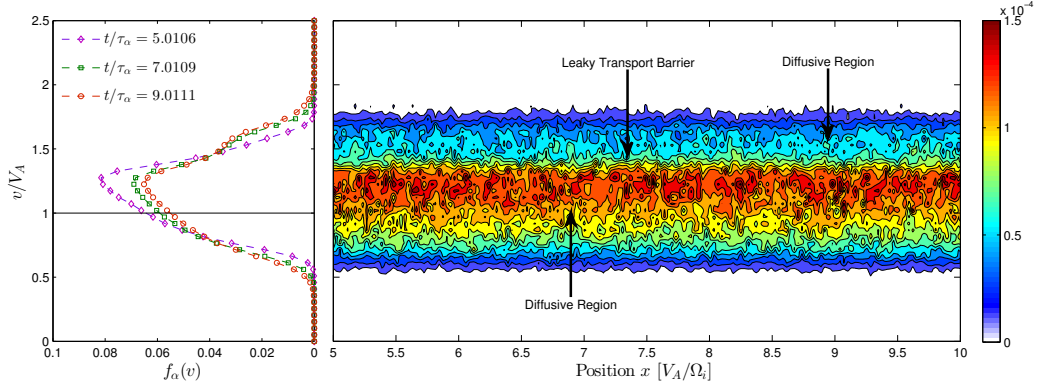
Figure 3.7: Re-energisation of the alpha-particle population during the nonlinear phase of the MCI. Left panel: probability density function of the minority alphas, $f_\alpha(v)$, as a function of the magnitude of their perpendicular velocity $v = \sqrt{v_x^2 + v_y^2}$, at three different times in the nonlinear stage of the hybrid simulation. The energisation of the alpha-particles is seen as the bump in $f_\alpha(v)$, which builds up in the nonlinear stage around $v/V_A \approx 1.5$. At this stage the particles reach velocities higher than the birth velocity $u_\perp/V_A \approx 1.2$. Right panel: filled contours representing the smoothed probability density function of the minority alpha-particles as function of position and their velocity $f_\alpha(x, v)$, at $t/\tau_\alpha \approx 9$. The temporal evolution of $f_\alpha(v)$ and $f_\alpha(x, v)$ suggests the existence of two phase space diffusive regions, where the smallest diffusion region can be identified with the bump of $f_\alpha(v)$ in the left panel, and a leaky transport barrier which produces the steep slope before the bump in $f_\alpha(v)$.

Using the data from Fig. 3.2, we calculate the fast Fourier transform of the change in the kinetic energy density of the alpha-particle population and the electromagnetic energy density associated with $\delta B_\parallel$. This calculation reveals three intense peaks at the frequencies $\omega/\Omega_\alpha = 20, 22$ and 24, of which the peak at $\omega/\Omega_\alpha = 22$ is the most intense by far. These frequencies correspond to the modes highlighted in Fig. 3.3(d) and to the peaks in Fig. 3.4 around $kV_A/\Omega_\alpha = 22$. These modes have a phase velocity close to the Alfvén speed, which suggests that the mechanism driving the re-energisation of the alpha-particles is related with the fast Alfvén wave.

3.5 Scaling properties of the MCI

In this section, we address the scaling properties with alpha-particle concentration of linear growth rates and intensity of the MCI in relation to D-T JET plasmas. In the early JET D-T experiments, high power neutral beam injection (NBI) was used to heat the plasma. By comparing plasmas where only deuterium NBI was used to those where a mixture of deuterium and tritium NBI was used, a linear correlation was identified between the measured ICE power and the measured fusion reactivity over six decades of the neutron source rate (c.f. Fig. 3 of Dendy et al. [1995]). Time resolved measurements during specific JET and TFTR D-T plasmas showed linear scaling of ICE intensity with local edge alpha-particle concentration as the time evolved (c.f. Fig. 4 of Dendy et al. [1995]). This established that the source of ICE in those plasmas was the fusion-born alpha-particles resulting from D-T fusion reactions. In this section we show that the hybrid simulations of the MCI can recover the scaling properties of ICE with respect to the concentration of energetic ions ξ_α, observed in JET and TFTR [Cottrell et al., 1993; McClements et al., 1996]. This gives further support to the MCI as the mechanism underlying ICE.

We perform hybrid simulations of the MCI with seven different values of ξ_α, ranging from $\xi_\alpha = 1 \times 10^{-4}$ to $\xi_\alpha = 1 \times 10^{-3}$, while keeping fixed all the other plasma and simulation parameters specified in Sec. 3.2. The first result drawn from these simulations is the excitation of perpendicular propagating fast Alfvén waves at consecutive cyclotron harmonics of alpha-particles for all the values of ξ_α. This is shown in Fig. 3.8(a) for the power spectra of the parallel perturbed magnetic field $\delta B_\parallel$ for $\xi_\alpha = 1 \times 10^{-4}$ (bottom black trace) and $\xi_\alpha = 1 \times 10^{-3}$ (top red trace), and in Fig. 3.8(b) for the power spectra of the perpendicular electric field component, $E_\perp = E_x$. In both cases the spectra encompass the linear and nonlinear stages of the MCI. An important difference between these simulations is the saturation time of the linear stage, being $t \approx 5\tau_\alpha$ for $\xi_\alpha = 1 \times 10^{-3}$ and $t \approx 15\tau_\alpha$ for $\xi_\alpha = 1 \times 10^{-4}$, where $\tau_\alpha = 2\pi/\Omega_\alpha$ is the alpha-particle gyro-period. After this saturation time in simulations, the linear stage gives way to the nonlinear effects which drive the lowest cyclotron harmonics peaks. Subsequently the minority alpha-particle population is re-energised [Carbajal et al., 2014].
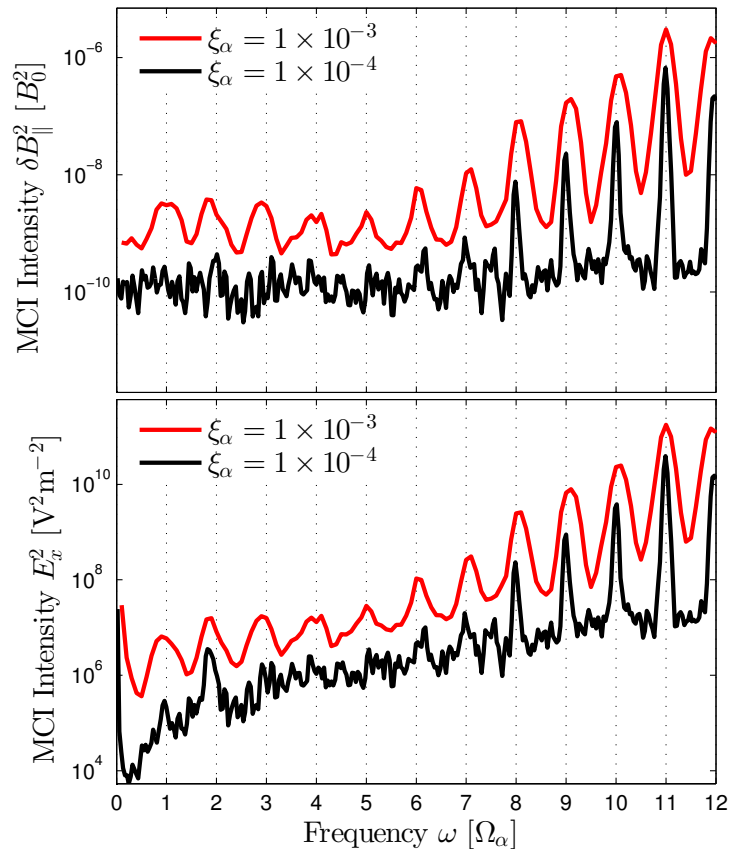
Figure 3.8: Log-normal plot of the MCI intensity: a) power density of the perturbed magnetic field of two typical hybrid simulations of the MCI with $\xi_\alpha = 1 \times 10^{-3}$ (red trace) and $\xi_\alpha = 1 \times 10^{-4}$ (black trace). b) power density of the transverse component of the electric field from the same simulations as panel a).

3.5.1 Noise levels in the hybrid simulations of the MCI

In plasma simulations using super-particles (Sec. 2.2.2) to describe the ion dynamics the electromagnetic fields, and therefore the ions' trajectories in phase space, contain errors due to the use of a finite number of super-particles [Aydemir, 1994]. These errors or noise in the simulations might produce non-physical effects such as artificial plasma heating, which in turn might drive or enhance instabilities in the simulated plasma [Hockney and Eastwood, 1989; Birdsall and Langdon, 2004]. Also, it is well known that the use of different super-particles shapes (c.f. Fig. 7.6 of Hockney and Eastwood [1989]) and different algorithms for advancing in time and space kinetic particles and electromagnetic fields contribute differently to the level of such noise (c.f. Fig. 7.7 of Hockney and Eastwood [1989]). The effect of noise on the simulations of the MCI becomes particularly important when using low alpha-

particle concentrations, where the amplitude of low-frequency (linearly unstable) modes driven by the minority alpha-particles are just above the noise levels.

Estimations of the noise level in plasma simulations using particles [Aydemir, 1994; Bottino et al., 2007] show that it depends, amongst other factors, on the number of super-particles used in the simulation N, decreasing as $1/\sqrt{N}$ as we increase N. Fig. 3.9 shows the power spectral density in frequency domain of the perturbed magnetic field $\delta B_\parallel$ (panel a)) and the transverse component of the electric field E_x (panel b)) for three hybrid simulation of the MCI with $\log_{10}(\xi_\alpha) = -4$ using three different values for the number of particles-per-cell (ppc) used for both ion species deuterons, and alpha-particles. In this figure the power spectrum of the electromagnetic fields encompass the linear and nonlinear stage of the MCI. As it can be seen, when few particles-per-cell are used in the simulation, that is, ppc = 20 (orange trace), the amplitude of the unstable modes of the MCI at alpha-particle cyclotron harmonics $\omega \geq 8\Omega_\alpha$ are marginally resolved, that is, their amplitude are just above the broadband noise in $\delta B_\parallel$ and E_x; while the modes at lower frequencies are not well resolved due to the high level of noise. As we increase the number of particles-per-cell to 200 (black trace) and 2000 (green trace), the noise levels are reduced drastically and the amplitude of all the unstable modes at alpha-particle cyclotron harmonics $\omega > 7\Omega_\alpha$ are well above the noise levels, while the mode at $\omega = 7\Omega_\alpha$ is marginally resolved. The modes $\omega \leq 6\Omega_\alpha$ are not well resolved in Fig. 3.9; even though these modes are marginally resolved in the frequency-wavenumber space, they are hidden by the noise levels when averaging along $k > 0$ to calculate the power spectrum of Fig. 3.9. This is shown in Fig. 3.10 for the numerical dispersion relation of $\delta B_\parallel$ for the simulation with $\log_{10}(\xi_\alpha) = -4$ and ppc = 2000, where modes at alpha-particle cyclotron harmonics $\omega \leq 5\Omega_\alpha$ start to be visible around wavenumbers with $k = \Omega_\alpha/V_A$ (black arrows).

From our hybrid simulations of the MCI with large alpha-particle concentration $\log_{10}(\xi_\alpha) \sim -3$, we observe that during the linear stage of the MCI the energetic alpha-particles transfer more energy to the electromagnetic fields at $\omega \geq 8\Omega_\alpha$ with respect to those simulations with $\log_{10}(\xi_\alpha) \sim -4$. Recalling that these higher frequency modes of the MCI drive unstable those at lower frequencies ($\omega < 4\Omega_\alpha$) during the nonlinear stage of the instability through wave-wave interactions (c.f. Sec. 3.3), it is expected that for simulations with $\log_{10}(\xi_\alpha) \sim -4$ these lower frequency modes will be more difficult to detect above noise levels because they have less energy with respect to the simulations with $\log_{10}(\xi_\alpha) \sim -3$; this is clearly visible in the top panel of Fig. 3.8, where we plot the power spectrum of the perturbed magnetic field $\delta B_\parallel$ for the simulations with $\xi_\alpha = 10^{-3}$ (red trace) and $\xi_\alpha = 10^{-4}$ (black trace).

To conclude, a comparison between simulations with $\xi_\alpha = 10^{-4}$ using ppc = 200 and ppc = 2000 shows convergent results for modes at alpha-particle cyclotron harmonics $\omega > 7\Omega_\alpha$, see Fig. 3.9. Therefore, all the results presented in the following sections about the scaling properties of the MCI at alpha-particle cyclotron frequencies $\omega > 7\Omega_\alpha$ are robust and well resolved by our simulations, while the results presented here for the mode at $\omega = 7\Omega_\alpha$ must be taken with caution since this mode is marginally resolved in these simulations. In the following we study the scaling properties of the MCI using hybrid simulations with ppc = 200 for both ion species given that they provide a good trade-off between numerical resolution and computational cost. Future work includes the use of more computationally intensive simulations using a larger number of particles-per-cell and low-noise methods [Sydora, 1999] to study the MCI driven by alpha-particle concentrations $\log_{10}(\xi_\alpha) \sim -4$.
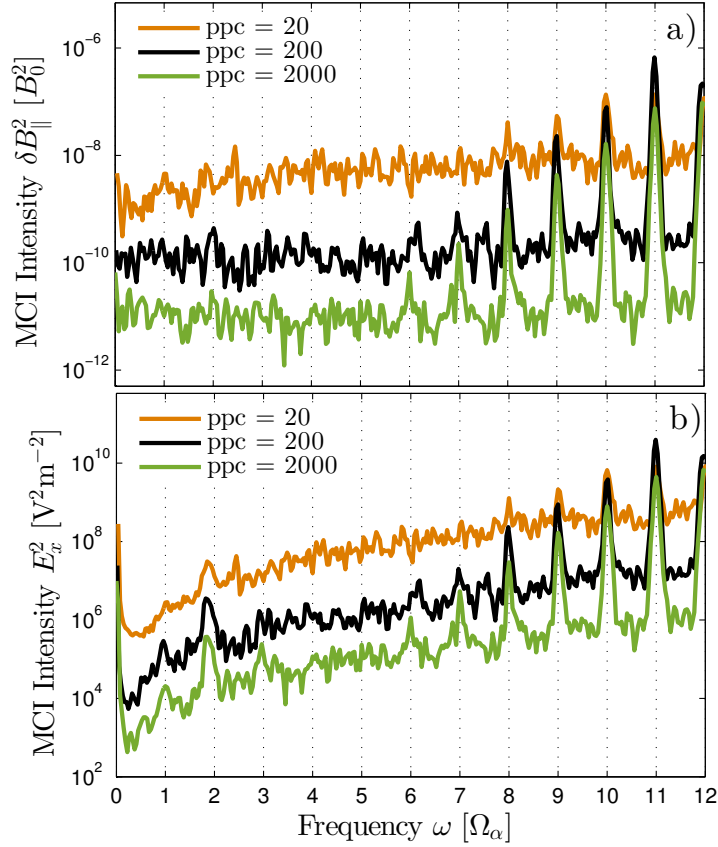
Figure 3.9: Power spectral density of the perturbed electromagnetic fields for three hybrid simulation of the MCI with $\log_{10}(\xi_\alpha) = -4$ using three different values for the number of particles-per-cell (ppc). Panel a): PSD of $\delta B_\parallel$ for simulations using ppc = 20 (orange), ppc = 200 (black) and ppc = 2000 (green). Panel b): same as panel a) for E_x. The noise level in the electromagnetic fields decreases as the number of super-particles increases.
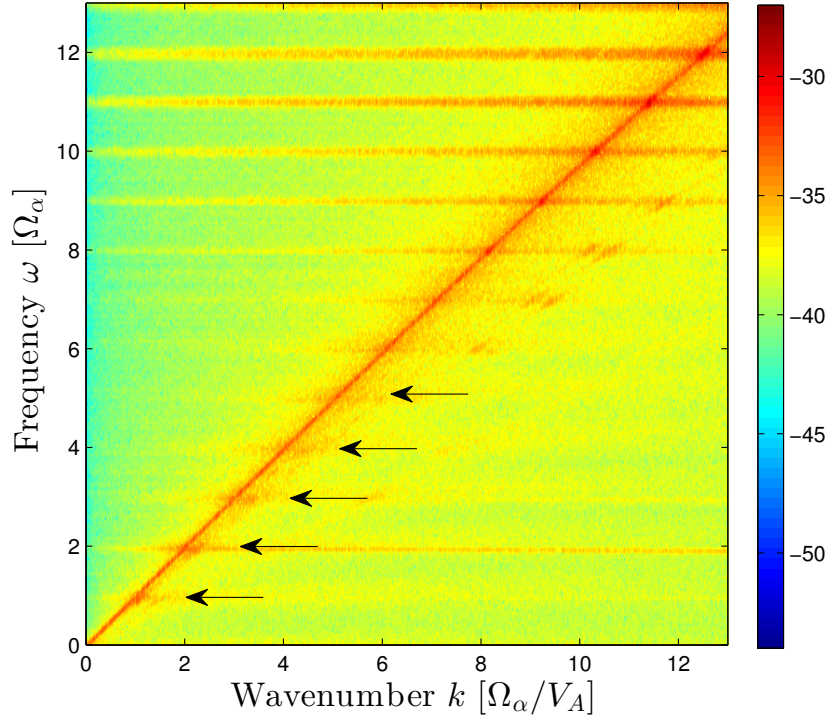
Figure 3.10: Colour shading of the $\log_{10}(\delta B_\parallel^2)$ in frequency-wavenumber for the hybrid simulation of the MCI with $\log_{10}(\xi_\alpha) = -4$ and ppc = 2000. Modes in the range $\omega \leq 6\Omega_\alpha$ (arrows) start to be visible, but they are hidden by the noise when averaging along $k > 0$ to calculate the power spectrum of Fig. 3.9.

3.5.2 Linear growth rates

Analytical calculations of the linear stability of the MCI show that the linear growth rates of low-frequency unstable modes, propagating quasi-perpendicular to the background magnetic field, scale linearly with alpha-particle concentration for plasma parameters corresponding to experiments in JET (c.f. Fig. 10 of Dendy et al. [1995]) and TFTR (c.f. Fig. 6 of McClements et al. [1996]).

This fact, on its discovery [Dendy et al., 1995; McClements et al., 1999], offered an encouraging point of contact between the theory of the MCI and the observations of ICE. However, there is no *a priori* reason to expect the characteristics of a linear growth rate to be reflected in a saturated signal. The work of Cook et al. [2013] and Carbajal et al. [2014], strongly suggests that the shared spectral properties of the linear analytical growth rates and of the ICE spectra reflect the very short timescale on which the MCI unfolds. Here we turn to the scaling of the

70

linear growth rate of the MCI, inferred from our hybrid simulations at early times, rather than from mathematical analysis, with energetic particle concentration ξ_α. In particular, we obtain the linear growth rates of the excited modes in the hybrid simulations of the MCI for the range of frequencies between $\omega = 7\Omega_\alpha$ and $\omega = 12\Omega_\alpha$. A similar study for harmonics below this range of frequencies is not possible, mainly because the linear instability for these lower modes is weak compared to the nonlinear effects which rapidly take over and drive them. First, we Fourier decompose $\delta B_\parallel$ in wavenumber space and relate each harmonic $\omega_n = n\Omega_\alpha$ to its corresponding wavenumber k_n through the numerical dispersion relation of Fig. 3.3. We then sum the contribution of the modes within the range of wavenumbers $[k_n - \delta k, k_n + \delta k]$, which are related to $[\omega_n - \delta\omega, \omega_n + \delta\omega]$, to obtain the time evolution of the excited modes of the MCI, $\delta B_\parallel (k_n \pm \delta k, t)$. The sum over the range of wavenumbers $[k_n - \delta k, k_n + \delta k]$ takes into account the finite energy exchange between the adjacent excited modes of the MCI, thus enabling better estimates of the linear growth rates. In all our calculations $\delta k V_A / \Omega_\alpha \approx 0.25$. A least-squares linear fit is then applied to the plot of $\log(\delta B_\parallel)$ versus t, in an appropriate time interval to infer the effective linear growth rate γ_n for each mode. This operation is repeated for each simulation with different alpha-particle concentration ξ_α. We fit our results to the following functional dependence of γ_n with ξ_α:

$$\gamma_n \sim \xi_\alpha^\zeta. \tag{3.5}$$

Performing a least-squares linear fit to the $\log_{10} - \log_{10}$ plot of Eq. (3.5) we can find the scaling exponent ζ. The results are shown in Fig. 3.11, where the error bars show the confidence interval for each fit. Notice that we extract linear growth rates of the MCI from hybrid simulations that evolve all modes in parallel as a nonlinear ensemble. These growth rates therefore incorporate the consequences of any coupling between modes, unlike the analytical treatment. Figure 3.11 shows square root scaling of γ_n with ξ_α for modes in the range of frequencies $\omega = 9\Omega_\alpha$ to $\omega = 12\Omega_\alpha$, and linear scaling for the mode at $\omega = 7\Omega_\alpha$. The linear theory of the MCI predicts the square root scaling of higher frequency modes in the presence of a shell-like velocity distribution of energetic alpha-particles in D-T plasmas for modes propagating perpendicular to $\boldsymbol{B}_0$ [Dendy et al., 1992], that is, modes with $k_\parallel = 0$. According to our simulations, this result seems to apply to the MCI driven by a ring-like distribution of minority alpha-particles (Eq. 3.1), too. Here $k_\parallel$ refers to the parallel component of the propagation vector $\boldsymbol{k}$, which is zero in all our simulations unless otherwise specified. In this case, the linear theory of the MCI assumes a cold background deuteron plasma $v_{T_D}/V_A \ll 1$, and that the fast Alfvén wave is only

in resonance with the minority alpha-particle population, that is $\omega = k V_A = l\Omega_\alpha$. Under this assumptions the scaling of the growth rates with ξ_α is showed to be (c.f. Eq. 36 of Dendy et al. [1992]):

$$\frac{\gamma_l}{\Omega_\alpha} = \frac{1}{\sqrt{2}} \frac{\omega_\alpha}{\omega_D} \frac{V_A}{u_\perp} \text{Imag}\left[\chi_0(z_\alpha)\right] \propto \sqrt{\xi_\alpha}\sqrt{\frac{m_D}{m_\alpha}}. \qquad (3.6)$$

Here, $\text{Imag}[x]$ is the imaginary part of x, $z_\alpha = l u_\perp/V_A$, V_A is the Alfvén speed, l is an integer, $u_\perp$ is the initial velocity of the fusion-born alpha-particles of Eq. (3.1), and m_α and m_D are the alpha-particle and deuteron mass, respectively. The full expression of $\chi_0(z_\alpha)$ is:

$$\chi_0^2(z_\alpha) = J_{2l} - \frac{i z_\alpha}{l} \frac{d J_{2l}}{d z_\alpha} + \left(1 - \frac{z_\alpha^2}{l^2}\right) J_{2l} + \frac{z_\alpha}{2l^2} \int_0^{2z_\alpha} J_{2l} dx. \qquad (3.7)$$

where $J_l(z_\alpha)$ is the Bessel function of order l. For all our simulations $v_{T_D}/V_A \sim 0.03$, where $v_{T_D}^2 = k_B T_D/m_D$ is the deuteron thermal velocity; this is consistent with Dendy et al. [1992] on the assumption of a cold background plasma. We note that square root scaling of γ_l with ξ_α is also predicted by the more general linear theory of the MCI when $\xi_\alpha \to 0$ for the case with $k_\parallel \neq 0$ [Cottrell et al., 1993].
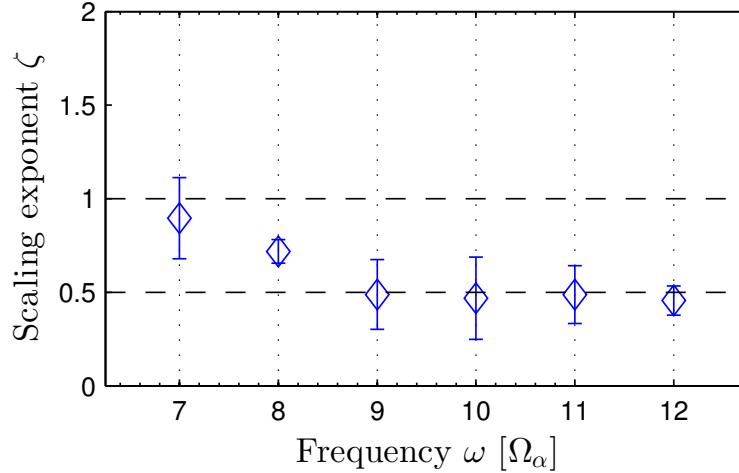
Figure 3.11: Scaling with alpha-particle concentration ξ_α of the linear growth rates γ of the MCI at successive cyclotron harmonics. The blue diamonds show the scaling exponents ζ of Eq. (3.5) obtained from the hybrid simulations of the MCI. The growth rates in the range $\omega = 9\Omega_\alpha$ to $\omega = 12\Omega_\alpha$ show square root scaling with ξ_α as predicted by Eq. (3.6), that is, $\zeta = 0.5$, while the mode at $\omega = 7\Omega_\alpha$ shows linear scaling with ξ_α, that is, $\zeta = 1$.

The fast Alfvén wave, which is a generalisation of the compressional Alfvén wave, shows strong correlation between perturbations of the number density of the

different ion species when interacting with them. This correlation allows us to measure how much the fast Alfvén wave interacts with the background deuterons and the minority alpha-particles in our hybrid simulations. We first define the perturbation of the number density of species j, δn_j as

$$n_j(x,t) = n_{0j} + \delta n_j(x,t). \tag{3.8}$$

Here n_j is the evolving number density of species j, and n_{0j} is its initial homogeneous value. Figure 3.12 shows the power spectral density in wavenumber space of the three variables $\delta B_\parallel / B_0$, δn_α and δn_D, all in the linear stage (panel a)), and in the nonlinear stage (panel b)), for the hybrid simulation with $\xi_\alpha = 1 \times 10^{-3}$. To calculate the spectra of Fig. 3.12, we first Fourier decompose $\delta B_\parallel / B_0$, δn_α and δn_D in wavenumber and frequency using data from the time interval $t/\tau_\alpha \leq 3$ and $t/\tau_\alpha \leq 10$ for the calculation encompassing the linear and nonlinear stage of the MCI, respectively; then, we integrate over the range of frequencies $0 \leq \omega/\Omega_\alpha \leq 14$. From these spectra it is evident that the fast Alfvén wave strongly interacts with the minority alpha-particles during the linear stage of the MCI, but not with the background deuterons. Specifically, $\delta B_\parallel$ and δn_α show the excitation of the same modes for $kV_a/\Omega_\alpha \geq 8$, whereas δn_D shows a broadband spectrum across the full range of wavenumbers. In contrast, during the nonlinear stage, the two ion species show similar spectra in wavenumber space, indicating that both ion species are interacting with the fast Alfvén wave. Other hybrid simulations with different ξ_α show the same features.

These results demonstrate that the Alfvén wave interacts strongly with only the minority alpha-particles during the linear stage, at frequencies and wavenumbers corresponding to the unstable modes of the linear MCI in the range $\omega = 9\Omega_\alpha$ to $\omega = 12\Omega_\alpha$. There is no interaction visible at the other frequencies and wavenumbers for either δn_D or δn_α.

3.5.3 Energy density

The energy density of the perturbations in the radially-outward propagating parallel magnetic field, $\delta B_\parallel^2 / 2\mu_0$, can be measured in some tokamak experiments that detect ICE. This quantity shows linear scaling with alpha-particle concentration in D-T plasmas in JET and TFTR, and is studied here using hybrid simulations of the MCI. For each hybrid simulations with different alpha-particle concentration ξ_α, we Fourier decompose $\delta B_\parallel$ in frequency and wavenumber space; then, we integrate $\delta B_\parallel^2(k,\omega)$ over the positive wavenumber domain $k > 0$, and keep record of $\delta B_\parallel^2(\omega)$ at
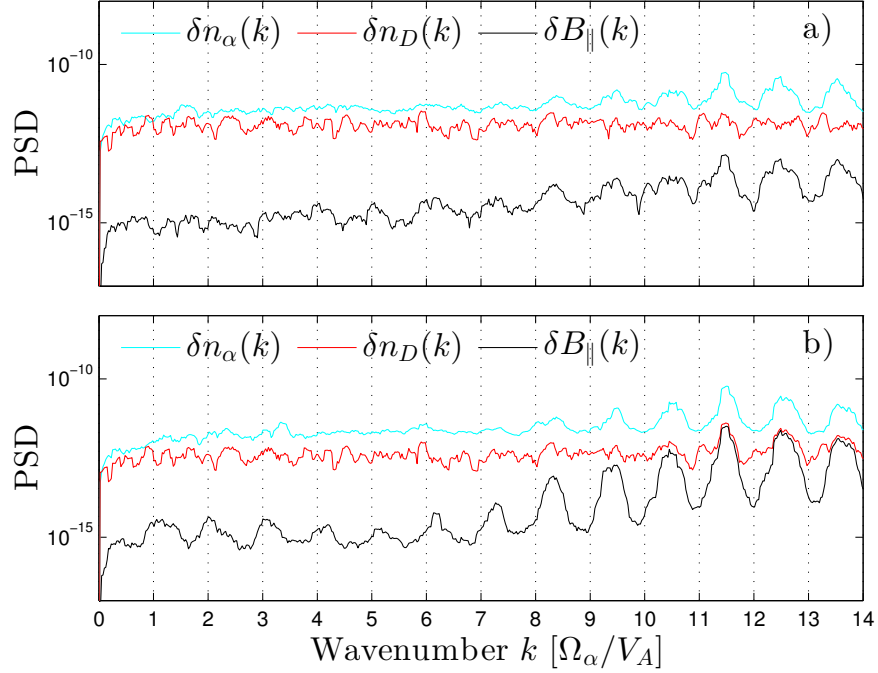
Figure 3.12: Power spectral density (PSD) in wavenumber space of perturbed number densities and magnetic field perturbations for the hybrid simulation with $\xi_\alpha = 1 \times 10^{-3}$. Panel a): Power spectra encompassing the linear stage of the MCI. From bottom to top: perturbed parallel magnetic field $\delta B_\parallel(k)/B_0$ (black), deuteron number density perturbation $\delta n_D(k)$ (red) and alpha-particle number density perturbation $\delta n_\alpha(k)$ (cyan). The excited modes at $kV_A/\Omega_\alpha \approx 8.5, 9.5, 10.5, 11.5$ and 12.5 are the same for $\delta B_\parallel$ and δn_α but not for δn_D. These modes correspond to $\omega/\Omega_\alpha = 8, 9\ 10, 11$ and 12, in the frequency domain (c.f. 3.3). Panel b): same as panel a), but the spectra now include the nonlinear stage of the MCI. Both ion species show similar spectra in wavenumber. Other hybrid simulations with different ξ_α show the same features. A running window average has been used to smooth every PSD trace.

each cyclotron harmonic $\omega = n\Omega_\alpha$, where $n = 7, \ldots, 12$. Next, we fit the perturbed magnetic energy density to the following functional dependence on alpha-particle concentration:

$$\frac{\delta B_\parallel^2(\omega)}{2\mu_0} \sim \xi_\alpha^\eta, \tag{3.9}$$

where μ_0 is the magnetic permeability of vacuum. The left hand side of Eq. (3.9) can be divided by the background magnetic field energy $(B_0^2/2\mu_0)$ in order to use the normalised spectra of Fig. 3.8(a),

$$\frac{\delta B_\parallel^2(\omega)}{B_0^2} \sim \xi_\alpha^\eta. \tag{3.10}$$

The top panel of Fig. 3.13 shows the best fit values of the scaling exponents η in Eq. (3.10) inferred from our simulations for each cyclotron harmonic $\omega = n\Omega_\alpha$, together with their confidence interval. Each exponent η is calculated using a least-squares linear fit of the $\log_{10} - \log_{10}$ plot of the normalized magnetic field energy of Eq. (3.10). The bottom six panels of Fig. 3.13 show the $\log_{10} - \log_{10}$ plots of the normalized magnetic field energy of Eq. (3.10) for each of the spectral peaks at $\omega = n\Omega_\alpha$ (red circles), along with the best linear fit (magenta trace) with its confidence interval (dashed black lines). Here, $n = 7, \dots, 12$. For all six cyclotron harmonics we see that the results are consistent with linear scaling ($\eta = 1$) of the magnetic field energy density with alpha-particle concentration. Preliminary results of hybrid simulations with ten times more particles-per-cell ppc = 2000, and therefore with lower noise levels, show the same linear trend for spectral peaks in the range $\Omega_\alpha \leq \omega \leq 6\Omega_\alpha$.

3.6 The MCI in relation to D-T JET core plasmas

During the DTE1 campaign of JET in 1997, where different mixtures of D-T were used in the NBI heating system, electron and ion heating driven by fusion-born alpha-particles was studied in detail [Thomas et al., 2001; Sharapov et al., 2008]. In these plasmas, instabilities enhanced by energetic alpha-particles such as toroidal Alfvén eigenmodes (TAEs) were not present [Thomas et al., 1998], which made it possible to study in detail the process of trapping and slowing down of alpha-particles born within the core plasma, only in the presence of MHD instabilities. These studies showed efficient electron heating due to fusion-born alpha-particles comparable to JET plasmas where ion-cyclotron resonance heating (ICRH) was used. Furthermore, the observed heating of the majority ions due to fusion-born alpha-particles was three times that of the electrons. This surprisingly efficient heating of the majority ions in the plasma was not observed when ICRH substituted alpha-particle heating. Furthermore, ICE originating at the core plasma in ASDEX-Upgrade, has been observed when parallel NBI is used [D'Inca, 2014]. The above mentioned pose the important question: whether MCI-driven ICE might occur at the core of DTE1 and future D-T JET plasmas, and to what extent this instability provides a channel for energy transfer between the minority fusion-born alpha-particles and the majority ions in these plasmas.
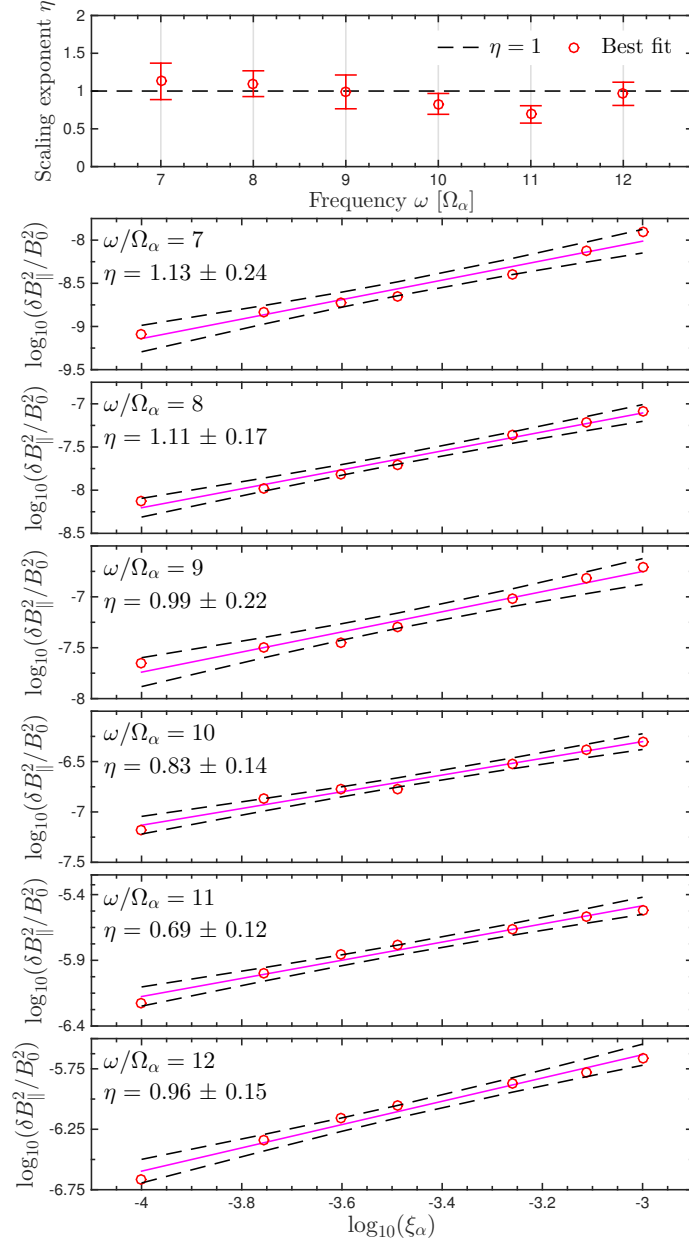
Figure 3.13: Scaling of the normalized perturbed magnetic field energy with alpha-particle concentration ξ_α. Top panel: the circles show the values of the scaling exponent η for each spectral peak of Fig. 3.8(a) obtained using a least-squares linear fit. The error bars show the confidence interval of each fit. Bottom panels: least-squares linear fits for the $\log_{10} - \log_{10}$ plots of the normalized magnetic field energy $\delta B_\parallel^2 / B_0^2$ vs. ξ_α for the cyclotron harmonics $\omega = n\Omega_\alpha$, where $n = 7, \ldots, 12$. The black dashed lines in each of these panels represent the confidence interval of the linear fit (magenta).

In this section, we aim to shed some light into this issue by performing hybrid simulations of the MCI using plasma parameters similar to those of DTE1 JET core plasmas [Thomas et al., 1998]. Additionally, we study the effect on the evolution of the MCI of using two different velocity distributions for the minority alpha-particles in our simulations. This will provide a first precedent for studying ICE originating at the core plasma, if core ICE is detected in future D-T plasmas in JET and ITER.

We perform two hybrid simulations of the MCI with a background magnetic field $B_0 = 3.4$ T, total number density and the electron temperature are $n = 10^{19}$ m^{-3} and $T_e = 10$ keV, respectively, and minority alpha-particle concentration $\xi_\alpha = 10^{-3}$. Initially thermalised background deuterons, which are in thermal equilibrium with the fluid electrons, and the minority alpha-particle population, are uniformly randomly distributed along the simulation domain. For the first simulation, we use an isotropic spherical shell distribution in velocity space for alpha-particles [Dendy et al., 1992], resembling the expected velocity distribution of newly-born alpha-particles [Thomas et al., 2001]

$$f_\alpha(v) = \delta\left(v - u_0\right), \qquad (3.11)$$

where u_0 is the magnitude of the initial velocity of the alpha-particles corresponding to the energy of 3.5 MeV at which alpha-particles are born in D-T fusion reactions. For the second simulation, we use a ring-like distribution of alpha-particles, as detailed in Sec. 3.2. This allows us to measure the effect of different velocity distributions of the alpha-particles on the evolution of the MCI [Dendy et al., 1992, 1993; Cottrell et al., 1993]. For these simulations the simulation domain consists of 4096 equal grid cells, each of length equal to $r_D/\sqrt{2}$, where $r_D = v_{T_D}/\Omega_D$ is the deuteron Larmor radius, $v_{T_D}^2 = k_B T_D/m_D$ is the deuteron thermal velocity, and Ω_D is the deuteron ion cyclotron frequency. For each ion species, we use 400 super-particles per grid cell, and the smoothing parameter is set to $\alpha_s = 10^{-7}$.

Figure 3.14 shows the time evolution in ion energy density and electric and magnetic field energy density. The effect of the two different velocity distributions on ion heating through the MCI for JET core plasmas is evident in this figure; intense ion heating driven by wave-particle interaction of the alpha-particles with the unstable modes of the MCI only is observed when the minority alpha-particles have a ring-like velocity distribution. For the case where the alpha-particles follow the velocity distribution function of Eq. (3.11), the MCI is heavily damped. Importantly, the energy gain of the background deuterons is 2000% larger in the simulation with a ring-like velocity distribution in comparison to the simulation with a shell-like velocity distribution.
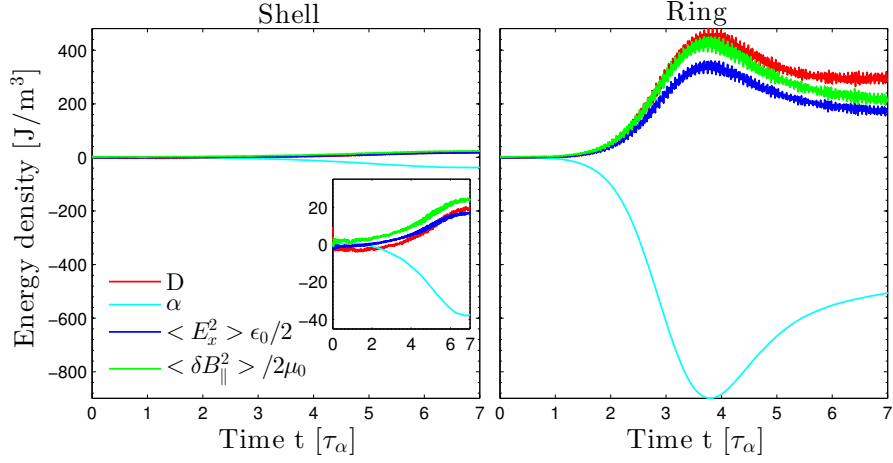
Figure 3.14: Time evolution of the change in particle energy density and field energy density of two simulations of the MCI with different alpha-particle velocity distributions. Left panel: hybrid simulation of the MCI with an isotropic spherical-shell-like velocity distribution for alpha-particles (c.f. Eq. 3.11). The inset in this panel shows a zoom of this panel for careful inspection. As can be seen, by the end of the simulation the MCI saturates and gives way to its nonlinear stage, where re-energisation of alpha-particles occurs. Right panel: hybrid simulation of the MCI with a ring-like velocity distribution for alpha-particles (c.f. Sec. 3.2). In both panels the red (cyan) line shows the change in the kinetic energy density of the deuterons (alpha-particles) along with the energy density of the magnetic field perturbation, $\delta B_\parallel \equiv B_z(x,t) - B_0$, (green line) and the perpendicular electric field E_x (blue line).

Figure. 3.15 shows the power spectra in frequency and wavenumber space of the parallel perturbed magnetic field $\delta B_\parallel$ of the hybrid simulations of the MCI with a shell-like (panels a) and b)) and a ring-like (panels c) and d)) velocity distribution of energetic alpha-particles. As can be seen, unstable modes of the MCI in the range of frequencies $10 \leq \omega/\Omega_\alpha \leq 12$ only are exited in the hybrid simulation using a ring-like velocity distribution of alpha-particles; that is, only when the velocity distribution of the energetic alpha-particles departs considerably from an isotropic velocity distribution, can the MCI occur under conditions of core D-T plasmas in JET. This might be because there is considerable pitch-angle scattering when the alpha-particles have a ring-like distribution function, whereas for a shell-like distribution function pitch-angle scattering loses its efficacy due to the isotropic distribution of alpha-particles in pitch-angle space.
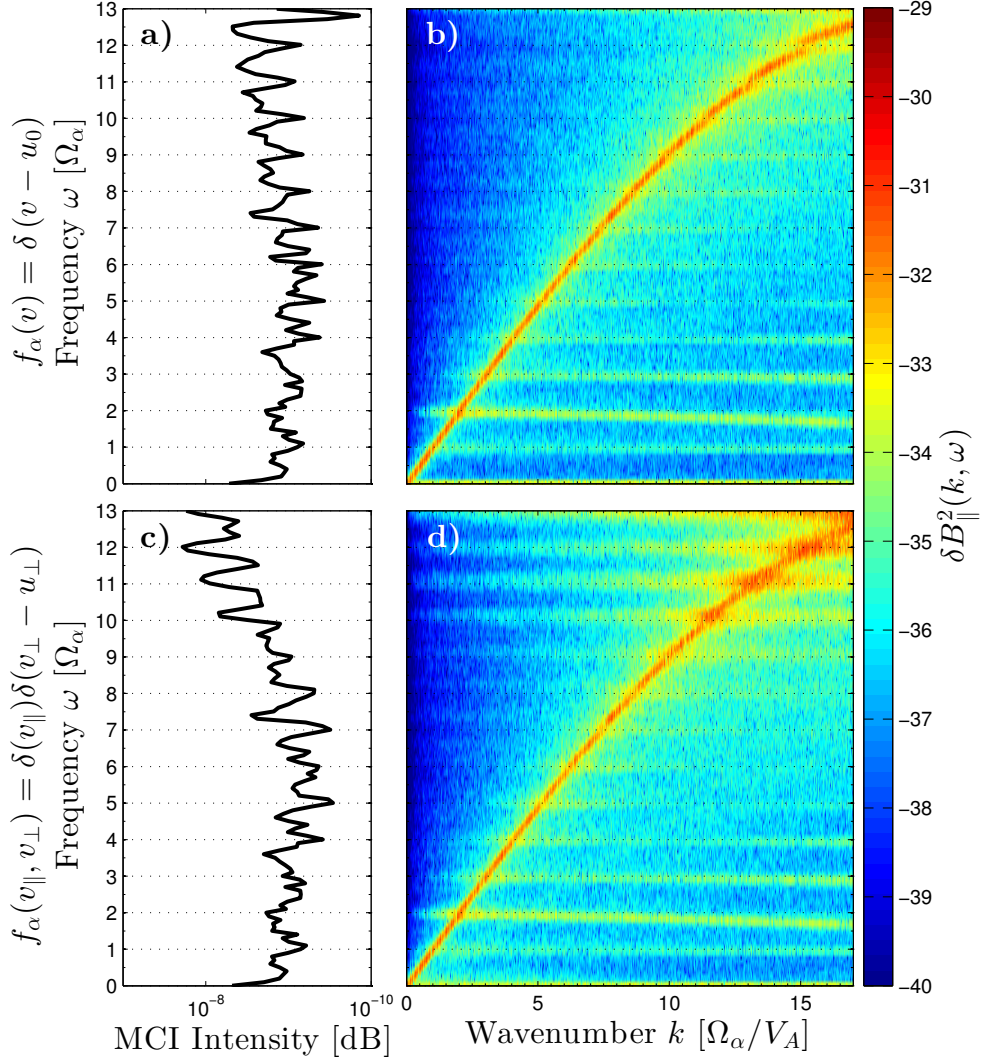
Figure 3.15: Power spectra in frequency and wavenumber space of $\delta B_\parallel$ of the two hybrid simulations of the MCI of Fig. 3.14. Panels a) and b) show the power spectra of the hybrid simulation of the MCI using a spherical shell velocity distribution for alpha-particles. Panels d) and d) show the power spectra of the hybrid simulation of the MCI using a ring-like velocity distribution for alpha-particles. Consistent with Fig. 3.14, the MCI only is excited when a ring-like distribution is used for the minority alpha-particle population. The horizontal lines in each plot show cyclotron harmonics of the alpha-particles $\omega = n\Omega_\alpha$.

3.7 Discussion

In this chapter, we presented the results of hybrid simulations of the MCI that deepen understanding of the links between the physics of this instability and the observational features of ICE from energetic ion populations in tokamak plasmas. Some of these features are known from the analytical linear theory of the MCI [Cauffman et al., 1995; McClements et al., 1996] and from recent fully kinetic particle-in-cell (PIC) simulations [Cook et al., 2013]. The hybrid approximation for the plasma enabled us for the first time to pursue simulations longer in time, and deep into the nonlinear phase of the MCI. We have focused on comparison with the measured ICE signal from D-T plasmas in JET [Cottrell et al., 1993; McClements et al., 1999; Sharapov et al., 2008], which has long been interpreted in terms of the MCI [Dendy et al., 1994a, 1995; McClements et al., 1996; Cook et al., 2013]. In this context, the results presented here link well to prior work that used other approaches and necessarily focused on earlier phases of the MCI, and, even more, show a number of novel phenomena emerging in the nonlinear phase of the MCI.

Our hybrid simulations of the MCI broadly validate the predictions of the linear theory [Dendy et al., 1995]. We observe the excitation of fast Alfvén waves at consecutive ion cyclotron harmonics of the alpha-particles in the range $5 \leq \omega/\Omega_\alpha \leq 12$, which play a key role in the linear stage transferring energy from the alpha-particles to the background deuterons. We also checked the predictions of analytical theory for the magnitude of the growth rates of the unstable modes, as well as their localization in the frequency domain and the magnitudes of their vector field components.

Extending our simulations deep into the nonlinear phase of the MCI, we recover substantial emission at the lowest spectral peaks, lying at the cyclotron harmonics one to three. These are present in the observed ICE signal, but are not predicted to be linearly unstable according to the analytical theory of the MCI. They are not well resolved, if present at all, in PIC simulations that extend over shorter time duration than the present hybrid results. It appears that these lowest spectral peaks arise from nonlinear physics which is captured here for the first time. Specifically, the amplitude of these modes is larger due to wave-wave interaction between higher harmonics localized around $kV_A/\Omega_\alpha \sim 11$ (cf. Fig. 3.6(b)). This is also evident from Fig. 3.4, where a gain of energy density at small wavenumbers is visible in panel (b).

Also, we have identified the novel and unexpected feature of re-energisation of the alpha-particle minority at later times, as a consequence of wave-particle reso-

nance with waves spontaneously excited by the alpha-particle population at earlier times. In addition, we studied the plasma-mediated interaction between the magnetic field perturbations $\delta B_\parallel$ and the perpendicular electric field component E_x, which are excited in the linear stage of the MCI. As the simulation enters the non-linear stage, we observe the self-modulation of the phase shift between the E_x and $\delta B_\parallel$, see for example Fig. 3.5.

We investigated the scaling of the linear growth rates of the MCI, as inferred from the hybrid simulations at early times, with alpha-particle concentration. We find that the linear growth rates of the modes excited at the cyclotron harmonics $\omega = 9\Omega_\alpha$ up to $\omega = 12\Omega_\alpha$ show square root scaling with ξ_α, while the mode at $\omega = 7\Omega_\alpha$ exhibits linear scaling.

A particular focus has been on the scaling of the saturated magnetic field energy density with alpha-particle concentration (Eq. (3.9)). The simulation results show linear scaling with ξ_α for modes of the electromagnetic fields excited at consecutive cyclotron harmonics of the minority alpha-particles from the seventh harmonic up to the twelfth harmonic. These results are in good agreement with observations of ICE intensity in JET and TFTR.

Finally, motivated by observations of ICE originating from core plasmas in the ASDEX-Upgrade tokamak, we performed hybrid simulations of the MCI driven by a minority population of fusion-born alpha-particles for conditions similar to core D-T plasmas in JET. We find that only when the alpha-particle velocity distribution departs significantly from an isotropic spherical-shell-like distribution in velocity space, can the MCI efficiently operate in core D-T JET-like plasmas; thus, representing an efficient channel for energy transfer between the energetic alpha-particles and the background ions. This result represent the first precedent of a numerical study of ICE in core plasmas in JET.

Chapter 4

Hybrid simulations of preferential ion heating due to intermittent magnetic fields in the solar wind

4.1   Introduction

Observations of the solar wind typically show the existence of preferential heating of protons and alpha-particles along the local magnetic field. This preferential ion heating is observed in the reconstructed velocity probability distribution functions of protons and alpha-particles, which have long tails along the local magnetic field [Hundhausen et al., 1967; Gurnett et al., 1979; Marsch et al., 1982a,b; Marsch, 2006]. The occurrence of this anisotropic heating of ions in the fast solar wind appears to be independent of the heliocentric distance at which the solar wind velocity is measured.

Fluctuations in the fast solar wind magnetic field exhibit inverse power-law regions in the frequency domain. At higher frequencies there is an inertial range of fully developed turbulence $\sim f^{-5/3}$ [Marsch and Tu, 1990; Goldstein et al., 1995; Bruno and Carbone, 2013], and at low frequencies a region $\sim 1/f$ whose origin is coronal [Matthaeus and Goldstein, 1986; Bruno et al., 2009; Verdini et al., 2012]. The broadband spectra of coherent waves permeating the solar wind are Alfvénic in nature [Belcher and Leverett, 1971; Belcher and Solodyna, 1975; Bruno et al., 1985; De Pontieu et al., 2007; Bruno and Carbone, 2013].

There is evidence that the inertial range fluctuations incorporate intermittent turbulence [Hnat et al., 2002; Bruno et al., 2007; Chapman and Hnat, 2007; Osman

et al., 2011, 2012; Alexandrova et al., 2013; Wu et al., 2013; Osman et al., 2014]. In addition, intermittency is also seen in fluctuations at lower frequencies in the $1/f$ range [Hnat et al., 2003; Horbury et al., 2005; Nicol et al., 2009]. Here, we refer to intermittency in the most general sense as the occurrence of occasional large-amplitude fluctuations, or bursts, in the time series of the solar wind parameters. As the fast solar wind plasma propagates away from the sun, the intermittent magnetic field evolves, showing both temporal and spatial intermittency [Taylor, 1938; Veltri, 1999].

There has been extensive modelling and simulations of ion heating by fluctuating fields in the solar wind. Ofman [2004] studied the heating of the solar wind using a three-fluid model for the plasma. A broadband spectrum of low-frequency Alfvén waves was used to drive the heating, with initial wave-phases that depended on the latitude at which they were launched from the base of the solar corona. However, a multi-fluid model for the plasma cannot describe in detail the wave-particle interactions, nor their effects on the velocity distributions of the different ion species of the plasma. In Liewer et al. [2001]; Araneda et al. [2008, 2009]; Matteini et al. [2010, 2011], and more recently Maneva et al. [2013], the heating of pure proton and proton-helium plasmas due to parametric decay of a single Alfvén wave, or due to broadband spectra of Alfvén waves, was examined using hybrid simulations of the expanding solar wind plasma in one spatial dimension. In these hybrid simulations, kinetic ion dynamics is resolved in detail. Valentini et al. [2008] and Valentini and Veltri [2009], explored ion heating in solar wind plasmas driven by high-frequency Alfvén waves using hybrid Vlasov-Maxwell simulations. However, alpha-particles were not included in their simulations, which can significantly modify the plasma dynamics despite their low abundance in the solar wind plasma [Maruca et al., 2012]. These studies showed the existence of mechanisms such as nonlinear ion trapping by ion-acoustic waves, resonant interaction of ions with ion cyclotron Alfvén waves, and ion trapping by parallel electric fields due to density or magnetic pressure gradients, which can drive preferential ion heating. Other studies [Nariyuki et al., 2010, 2014] have shown the occurrence of preferential ion heating driven by nonlinear Alfvén wave packets in the expanding solar wind plasma in the absence of parametric instabilities. More recently, in Perrone et al. [2013], the authors showed the occurrence of preferential ion heating of protons and alpha-particles in their simulations of two-dimensional plasma turbulence in the solar wind. Importantly, all these studies provide mechanisms and configurations of solar wind plasmas that might underlie the observed preferential ion heating in the solar wind, but intermittency is not included in their models.

In this chapter we present the first study of preferential ion heating in the fast solar wind at 1 AU that explicitly includes intermittent electromagnetic fields in a self-consistent way. We investigate the effect on preferential ion heating of different levels of intermittency within $1/f^\gamma$ broadband spectra of Alfvén waves. We perform 1.5D hybrid simulations of the relaxation of intermittent broadband spectra of Alfvén waves in a solar wind plasma comprised of protons and alpha-particles. We identify gyrobunching and ion trapping by the electric field as the mechanisms underlying the observed preferential ion heating, and determine the effect of intermittency on the local ion temperature and on the ion temperature anisotropy for protons and alpha-particles. We study the detailed time evolution of the fluctuations of the ion velocity and magnetic field for different scenarios with different levels of intermittency. We find that the level of intermittency of the electromagnetic fields strongly affects the temporal and spatial dynamics of the mechanisms underlying preferential ion heating, as well as temperature anisotropy of both ion species.

4.2   Simulation set-up

We study the effect of different levels of intermittency and different spectral exponents γ of $1/f^\gamma$ broadband spectra of Alfvén waves on preferential ion heating in the fast solar wind. We specify both the amplitude and phase spectra of these waves as an initial condition; they are then left to freely relax in time. We test the sensitivity of simulation results to different values of the spectral exponent γ by choosing $\gamma = 0, 1,$ and $5/3$. In all the hybrid simulations presented here, we use characteristic values of the magnetic field strength, number density and electron temperature of solar wind plasmas as measured at 1 AU [Bruno and Carbone, 2013].

Our simulations are carried out in slab geometry, with the direction of variation parallel to the background magnetic field. The background magnetic field is $\boldsymbol{B}_0 = B_0 \hat{\boldsymbol{x}}$, with $B_0 = 6$ nT. In order to compare our results to those of Maneva et al. [2013], we consider a homogeneous plasma of thermalized majority protons and a minority population of alpha-particles with equal temperatures $T_p = T_\alpha$, where the ion betas $\beta_i = v_{th,i}^2/V_A^2$, defined in terms of the thermal speed of each species $v_{th,i} = \sqrt{2k_b T_i/m_i}$ and the Alfvén speed $V_A = B_0/\sqrt{\mu_0 n m_p}$, are $\beta_\alpha \approx 0.02$ and $\beta_p \approx 0.08$, which correspond to a temperature of $T_p = T_\alpha = 2 \times 10^4$ K. The electron beta is $\beta_e = 2\mu_0 n_e T_e/B_0^2 \approx 0.5$ ($T_e \approx 1.3 \times 10^5$ K). The alpha-particle concentration in all the simulations is $n_\alpha/n_e = 0.05$, which corresponds to the characteristic abundance of alpha-particles in the fast solar wind [Marsch et al., 1982a].

The numerical parameters of the hybrid simulations are chosen so that they properly resolve the ion gyromotion in space and time, together with the fastest mode of the electromagnetic fields included in the hybrid approximation for the plasma [Pritchett, 2000]. The simulation domain consists of 4096 grid cells, which corresponds to length $L = 1024d_p$, where d_p is the ion inertial length. This set-up offers a good trade-off between resolution and computational cost, given that $d_p \approx 3.6r_p$ and $r_p = r_\alpha$, with r_p and r_α the proton and alpha-particle gyro-radius, respectively. For each ion species we use 400 super-particles per grid cell. For all the simulations the smoothing parameter is set to $\alpha_s = 5 \times 10^{-7}$.

4.2.1 Set-up of the intermittent electromagnetic fields

We include intermittency in the initial $1/f^\gamma$ broadband spectrum of Alfvén waves driving the ion heating in our simulations, by initially specifying a non-random phase relationship between these waves. These waves initially satisfy the appropriate dispersion relation of the plasma at $t\Omega_p = 0$, and together contain the same total field energy in all the simulations.

Clear evidence of broadband Alfvénic activity in the solar wind has been observed in early [Belcher and Leverett, 1971; Belcher and Solodyna, 1975; Bruno et al., 1985] and recent [De Pontieu et al., 2007; Bruno and Carbone, 2013] studies of the solar wind, which show strong correlation between the solar wind velocity and the local magnetic field. Outward-propagating Alfvén waves dominate [Belcher and Leverett, 1971]. For this reason, we simplify our study of the solar wind by only considering broadband spectra of transverse Alfvén waves as drivers of the ion heating in the hybrid simulations. These waves, propagating parallel to the background magnetic field, are chosen to belong to the lower branch ($\omega < \Omega_\alpha$) of the dispersion relation of a proton-alpha-particle plasma [Sonnerup, 1967] in the cold approximation:

$$k^2 - \frac{\omega^2}{c^2} + \frac{1}{c^2} \sum_{s=e,p,\alpha} \frac{\omega_{ps}^2 \omega}{\omega - \Omega_s} = 0, \tag{4.1}$$

where c is the speed of light, $\omega_{ps}^2 = n_s(Z_s e)^2/\epsilon_0 m_s$ and $\Omega_s = Z_s e B_0/m_s$ are the plasma and cyclotron frequencies of species s, respectively. Here, e is the magnitude of the electron charge, ϵ_0 is the vacuum permittivity, and Z_s and m_s are the atomic number and mass of ion species s (for the case of the electrons $Z_e = -1$, and $\Omega_e = -eB_0/m_e$).

Following Maneva et al. [2013], the initial configuration of the perturbed magnetic field $\delta\boldsymbol{B}(x)$ consists of $N = 31$ normal modes with wavenumbers and

frequencies in the ranges $k_j d_p \in [0.017, 0.542]$ and $\omega_j/\Omega_p \in [0.015, 0.357]$, where $j = 1, \ldots, N$. Thus, the components of the perturbed magnetic field are

$$
\delta B_y(x) = \sum_{j=1}^{N} B_j \cos(k_j x + \vartheta_j), \tag{4.2}
$$

$$
\delta B_z(x) = \sum_{j=1}^{N} B_j \sin(k_j x + \vartheta_j), \tag{4.3}
$$

where B_j and ϑ_j are the amplitudes and initial wave-phases of the jth mode, respectively. The relationship between the initial wave-phases of the different modes determines the level of intermittency (burstiness) of the magnetic field. Each ϑ_j occurs with uniform probability in the range $[0, \theta^*]$, where θ^* is the spread in phase angles of the ϑ_j. Smaller values of θ^* result in more phase coherent waves, and hence more bursty magnetic fields, along the simulation domain. Conversely the limiting case $\theta^* = 360°$ corresponds to the random-phase approximation for the magnetic field perturbations. In this way, for a fixed power spectral density of Alfvén waves, we can obtain different levels of intermittency. Figure 4.1 shows three examples of magnetic fields with the same spectral density $(1/f)$ but different levels of intermittency (burstiness). Notice that in some regions of the simulation domain the amplitude of the magnetic field perturbations are of the same order as the background magnetic field, which makes possible the existence of coupling between compressional and shear Alfvén waves in our simulations.

The initial velocity distribution of protons and alpha-particles is specified to self-consistently couple the ion dynamics with the spectrum of Alfvén waves defined by Equations (4.2) and (4.3) [Sonnerup, 1967; Maneva et al., 2013]. This is done by introducing the following drift velocities into the initial thermalised velocity distributions of both ion species:

$$
\delta u_{sy}(x) = -\sum_{j=1}^{N} \frac{\omega_j/k_j}{1 - \omega_j/\Omega_s} \frac{B_j}{B_0} \cos(k_j x + \vartheta_j),
$$

$$
\tag{4.4}
$$

$$
\delta u_{sz}(x) = -\sum_{j=1}^{N} \frac{\omega_j/k_j}{1 - \omega_j/\Omega_s} \frac{B_j}{B_0} \sin(k_j x + \vartheta_j),
$$

$$
\tag{4.5}
$$

Here δu_s is the perturbation of the velocity distribution function of either ion species, protons or alpha-particles, $s = p, \alpha$, with respect to the Maxwellian background. In Equations (4.4) and (4.5), the wave frequencies ω_j are calculated using the dispersion relation of Equation (4.1) given the values of the wavenumbers k_j.
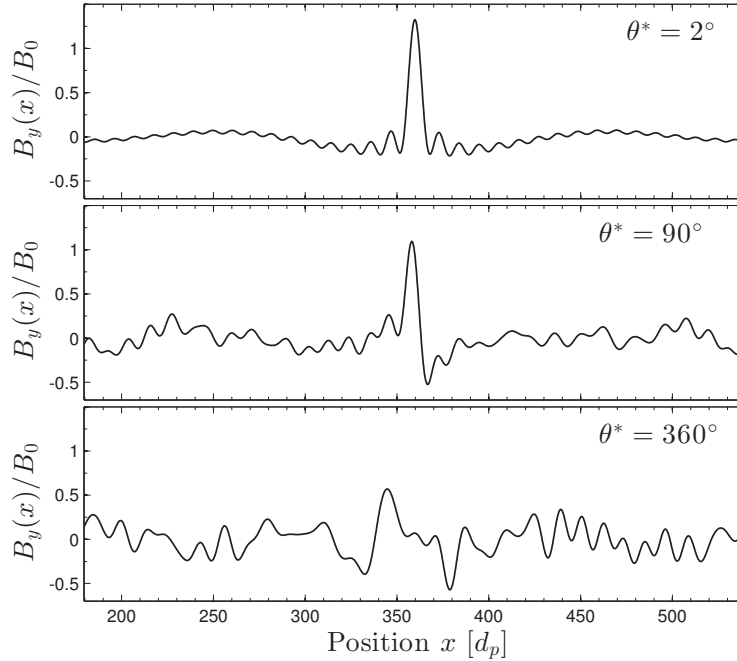
Figure 4.1: Initial condition for magnetic fields with the same power spectral density $1/f$ and three different levels of intermittency (burstiness). Subset of simulation domain shown. For simplicity, only the y component of $\delta \boldsymbol{B}(x)$ (c.f. Equation 4.2) is shown. Three different values of θ^* are used to specify the level of intermittency: $\theta^* = 2°, 90°$ and $360°$. The case with $\theta^* = 2°$ corresponds to the most intermittent magnetic field, whereas $\theta^* = 360°$ corresponds to the random-phase approximation for the magnetic field perturbations. All these magnetic fields contain the same total field energy. Notice that in some regions of the simulation domain the amplitude of the magnetic field perturbations are of the same order as the background magnetic field, which makes possible the existence of coupling between compressional and shear Alfvén waves in our simulations.

In order to compare our results with those of Maneva et al. [2013], where intermittency is not included, we chose the energy of the entire spectrum to be 6.25% of the background magnetic field energy in all our simulations, that is, $|\delta \boldsymbol{B}|^2/B_0^2 = 0.0625$. This corresponds to an effective amplitude of the integrated spectrum which is 25% of the magnitude of the background magnetic field. We now present the results of five hybrid simulations with different levels of intermittency.

4.3 Simulation results

We perform simulations of a $1/f^\gamma$ broadband spectrum of Alfvén waves relaxing in a solar wind plasma using five different values of θ^*: $2°, 90°, 180°, 270°$, and $360°$. We first describe the mechanisms responsible for the ion heating in our simulations. Then we examine the effect of these mechanisms on the local ion temperature, explain the difficulties arising if we wish to define average ion temperatures in our simulations, and discuss the implications for *in situ* observations of the intermittent solar wind. Next we study the dependence of the parallel and perpendicular ion temperature, and of temperature anisotropy, on intermittency. We also study the time evolution of the energy of protons, alpha-particles and electromagnetic fields in each case, in order to infer the effectiveness of the mechanisms driving the ion heating in relation to the intermittency level of the initial magnetic field perturbations. We then compare the results with observations of the solar wind. Finally, we study how the time evolution of the fluctuations of the ion velocity and magnetic field depend on the intermittency levels.

4.3.1 Mechanisms driving ion heating in the hybrid simulations

Reconstructed velocity distribution functions $f(v_\parallel, v_\perp)$ for protons and alpha-particles of the fast solar wind show the occurrence of preferential heating along the ambient magnetic field [Hundhausen et al., 1967; Marsch et al., 1982a,b; Marsch, 2006]. This heating can be seen in velocity space as an elongation of the core of $f(v_\parallel, v_\perp)$ of protons along the perpendicular direction, together with the formation of a small beam of protons streaming approximately parallel to the ambient magnetic field with speeds comparable to the local Alfvén speed $V_A = B_0/\sqrt{\mu_0 n m_p}$. In Figures 4.2 and 4.3 we show $f(v_\parallel, v_{\perp,2})$ for alpha-particles and protons, at three simulation times: $t\Omega_p = 25.07, 629.07$, and, 2000, for the cases with $\theta^* = 2°$, for highly intermittent Alfvén waves, $\theta^* = 360°$, for random-phase Alfvén waves, and $\theta^* = 180°$, for the intermediate case. Here, the parallel and perpendicular components of the ion velocity are defined with respect to the background magnetic field, that is, $v_\parallel = v_x$, $v_{\perp,1} = v_y$ and $v_{\perp,2} = v_z$. In all the hybrid simulations we observed the occurrence of preferential ion heating. However, the detailed features of $f(v_\parallel, v_{\perp,2})$ differ, and have distinct time variation, for simulations that embody different levels of intermittency, suggesting that the mechanisms underlying the ion heating act in different ways [Valentini and Veltri, 2009; Matteini et al., 2010].

By looking at the time evolution of both the parallel velocity $v_\parallel(x, \phi)$ as function of the ion gyro-angle $\phi = \arctan(v_{\perp,2}/v_{\perp,1})$ and the ion distribution function
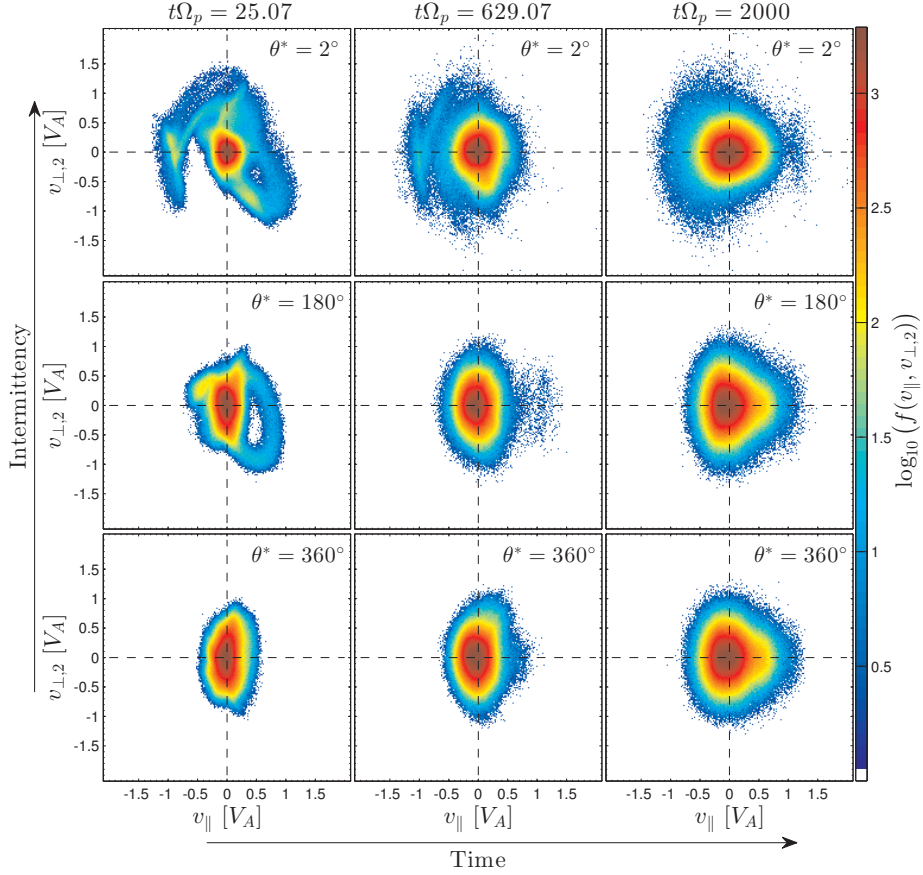
Figure 4.2: Dependence of ion velocity distribution functions on the level of intermittency. Colour shading of $\log_{10}\left(f(v_\parallel, v_{\perp,2})\right)$ of alpha-particles for thee hybrid simulations at different simulation times. The top panels show $f(v_\parallel, v_{\perp,2})$ of alpha-particles for the simulation times, $t\Omega_p = 25.07$, 629.07, and, 2000, for the hybrid simulation in the high-intermittent case $\theta^* = 2°$. Middle and bottom panels show the corresponding $f(v_\parallel, v_{\perp,2})$ for the hybrid simulations with $\theta^* = 180°$ and $\theta^* = 360°$, respectively. The horizontal and vertical dashed lines show $v_{\perp,2} = 0$ and $v_\parallel = 0$, respectively. At the final simulation time $t\Omega_p = 2000$, the alpha-particle $f(v_\parallel, v_{\perp,2})$ for the simulation with $\theta^* = 360$ shows a drift of its core anti-parallel to $\boldsymbol{B}_0$. The core of $f(v_\parallel, v_{\perp,2})$ for the simulation with $\theta^* = 2$ shows elongation along $\boldsymbol{B}_0$. We observe the occurrence of preferential ion heating of alpha-particles for all θ^*, i.e. all levels of intermittency. However, the features of $f(v_\parallel, v_{\perp,2})$ in each case are different, suggesting that the mechanisms underlying the ion heating act in different ways.

in the $xv_\parallel$-plane $f(x, v_\parallel)$, it is possible to identify the mechanisms underlying preferential ion heating in our simulations. Figure 4.4 shows $v_\parallel(x, \phi)$ for alpha-particles in the highly intermittent hybrid simulation with $\theta^* = 2$ at two times: the initial condition $t\Omega_p = 0$, in panel a); and at $t\Omega_p = 25$, in panel b), when heating starts to occur for this simulation. In this figure, dark red and blue colours indicate sig-
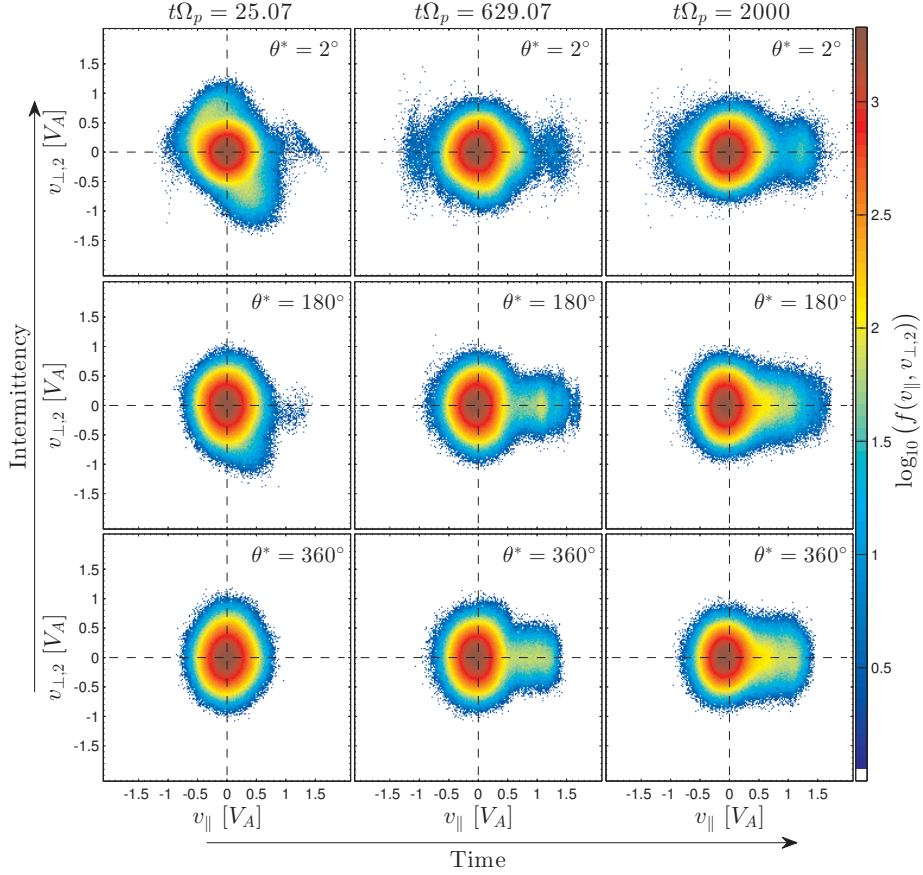
Figure 4.3: Dependence of ion velocity distribution functions on the level of intermittency. Colour shading of $\log_{10}\left(f(v_\parallel, v_{\perp,2})\right)$ of protons for thee hybrid simulations at different simulation times. Same as in Fig. 4.2, but for protons. At the final simulation time, $t\Omega_p = 2000$, the core of the proton $f(v_\parallel, v_{\perp,2})$ shows a drift anti-parallel to $\boldsymbol{B}_0$ in all cases. However, this is more evident for the simulation in the random phase limit $\theta^* = 360$. We observe the occurrence of preferential ion heating of protons for all θ^*, i.e. all levels of intermittency. However, the features of $f(v_\parallel, v_{\perp,2})$ in each case are different, suggesting that the mechanisms underlying the ion heating act in different ways.

nificant bunching of ions in gyro-angle space; that is, populations of alpha-particles that become phase coherent due to wave-particle interactions. Panel c) shows the corresponding $f(x, v_\parallel)$ for the alpha-particles of panel b). We also plot the normalized magnetic pressure $P_B(x) \sim \delta B^2(x)$ to show that the source of accelerated alpha-particles at $x \approx 340 d_p$ and $x \approx 390 d_p$ in panel c) is a region of high magnetic pressure ($x \approx 380 d_p - 390 d_p$). These alpha-particles are accelerated to velocities comparable to the Alfvén speed ($|v_\parallel| \sim V_A$), and can be identified as the populations of gyrobunched alpha-particles of panel b). This generic wave-particle interaction,

previously identified as gyrobunching [Cook et al., 2011], is one of the mechanisms driving ion heating in our simulations. Gyrobunching is also observed for protons, and is present in all our simulations where very intense regions of magnetic pressure occur.

In Figure 4.5 we show $f(x, v_\parallel)$ for the protons (left panels) and alpha-particles (right panels) in three hybrid simulations with different levels of intermittency at the simulation time $t\Omega_p = 25.07$. In this figure we also show the normalized magnetic pressure $P_B(x)$ in dark blue and the normalized total particle density $n(x)/n_e$ in red. Gyrobunching generates perturbations in the ion number density $n(x)/n_e$ in our simulations, which in turn generate intense parallel electric fields $E_x(x)$ through the last term of Eq. (1.20). In this situation, the dynamics of ions streaming along $\boldsymbol{B}_0$ is perturbed in different ways by $E_x(x)$, depending on their kinetic energy: passing through regions of intense electric field if they have sufficiently large kinetic energy, or being trapped or deflected by $E_x(x)$ if their kinetic energy is small compared to the local electric potential energy. We can identify the regions where ion reflection or ion trapping occur by calculating the electric potential $\varphi(x) = \int_{x_0}^{x} E_x(x')dx'$, where x_0 is assumed to be far away from any perturbation. From $\varphi(x)$ we can define a threshold value $v_{cj}(x) = \sqrt{2eZ_j\varphi(x)/m_j}$ for the ion parallel velocity $v_{\parallel j}$ of species j, such that an ion initially streaming along $\boldsymbol{B}_0$ with $\mid v_{\parallel j} \mid < v_c$ will be deflected or trapped by $E_x(x)$. However, ions with $\mid v_{\parallel j} \mid > v_c$ will continue streaming along $\boldsymbol{B}_0$ without being significantly perturbed by the parallel electric field. In Figure 4.5 we show v_c, for ions initially streaming parallel to $\boldsymbol{B}_0$, and $-v_c$, for ions initially streaming anti-parallel to $\boldsymbol{B}_0$. In panels a) and b) we see that protons are deflected by the intense electric field around $x \approx 350d_p$, whereas alpha-particles previously accelerated through gyrobunching (c.f. Figure 4.4) have acquired enough kinetic energy to pass through the region of intense $E_x(x)$ around $x \approx 350d_p$. When intense parallel electric fields occur in two contiguous regions, an ion trapping region forms. In panels c) to f) of Figure 4.5, we indicate with arrows some regions where ion trapping occurs. For all the values of θ^* considered, ion trapping by the electric field is observed; this mechanism seems to be more effective for Alfvén waves with initial random phases, e.g. panel e) of Figure 4.5.

Together, the quantities $v_\parallel(x, \phi)$, $f(x, v_\parallel)$, $P_B(x)$, $n(x)$ and $v_c(x)$, enable us to identify gyrobunching and ion trapping by the electric field as the mechanisms driving the preferential ion heating in our hybrid simulations of the solar wind. How these mechanisms operate to heat the plasma can be summarized as follows. At early times, protons and alpha-particles are accelerated along the background magnetic field due to gyrobunching in the regions of high magnetic pressure along the
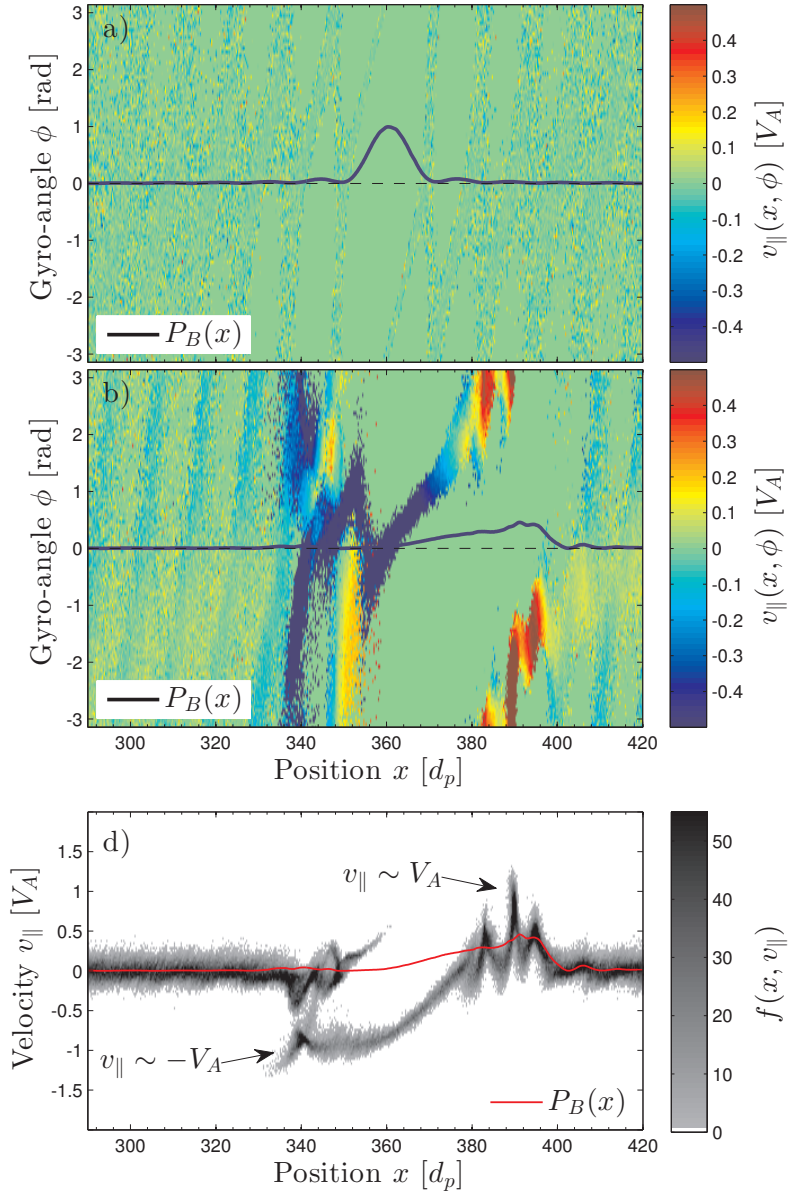
Figure 4.4: Alpha-particle acceleration due to gyrobunching in the hybrid simulation where $\theta^* = 2°$. Panels a) and b) show the colour shading of the parallel velocity $v_\parallel(x, \phi)$, where $\phi = \arctan(v_{\perp,2}/v_{\perp,1})$ is the ion gyro-angle, for the initial condition $t\Omega_p = 0$ and $t\Omega_p = 25.07$, respectively. Dark red and blue colours indicate significant bunching of ions in gyro-angle space. Panel c) shows $f(x, v_\parallel)$ for panel b). Alpha-particles accelerated to velocities $|v_\parallel| \sim V_A$ around regions of high magnetic pressure ($x \approx 380 d_p$), can be identified as the alpha-particle populations bunched in gyro-angle space in panel b). Gyrobunching for protons and alpha-particles is seen in all the simulations.

simulation domain, as shown in Figure 4.4. This acceleration produces significant fluctuations in the plasma number density $n(x)$, which at the same time generates
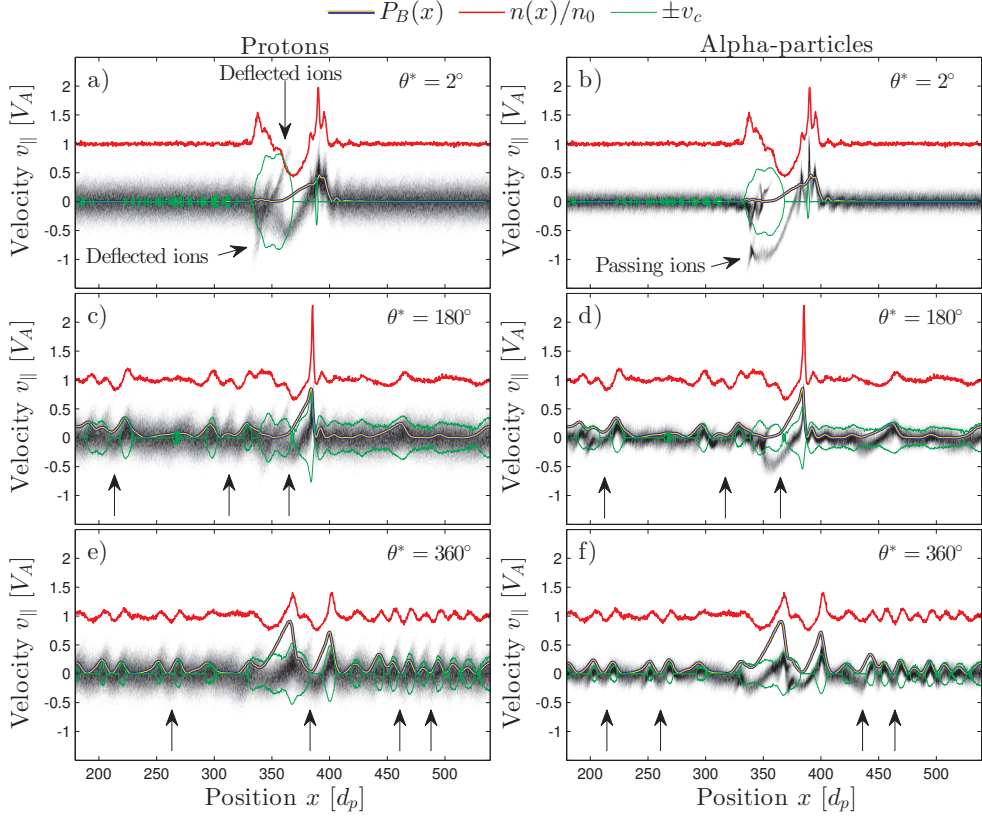
Figure 4.5: Grey scale plot of the ion distribution function $f(v_\parallel, x)$ of protons (left column) and alpha-particles (right column) at $t\Omega_p = 25.07$. Darker areas in each panel represent larger $f(v_\parallel, x)$. Along with $f(v_\parallel, x)$ we show the normalized magnetic pressure $P_B(x) \sim B^2(x)$ in dark blue, the normalized particle density $n(x)/n_e$ in red, and the critical ion velocity $\pm v_c$ in green. The magnetic pressure $P_B(x)$ is normalized to one. These quantities allow us to identify gyrobunching and ion trapping by the electric field, notably in the regions marked by arrows in panels c) to f), as the mechanisms which drive the ion heating in all the simulations. Gyrobunching and ion trapping work together, accelerating protons and alpha-particles in all the simulations shown, independent of the intermittency level of the magnetic fields. However, the specific dynamics of these mechanisms do depend on the levels of intermittency.

parallel electric fields $E_x(x)$ that can trap ions. This process repeats during the simulation, eventually providing the ions with enough kinetic energy so they can escape the trapping regions and form the ion beams observed in Figs. 4.2 and 4.3.

4.3.2 Ion energisation

Gyrobunching and ion trapping work together to accelerate protons and alpha-particles along the background magnetic field in the hybrid simulations, regardless of the level of intermittency of the broadband spectra of Alfvén waves driving the ion heating. Different levels of intermittency of the magnetic field fluctuations produce spatially inhomogeneous heating along $\boldsymbol{B}_0$, which is different in each case. Figure 4.6 shows the normalised local proton and alpha-particle parallel temperatures $T_{s\parallel}(x,t) = m_s \langle \delta v_{s\parallel}^2 \rangle / m_p V_A^2$ at $t\Omega_p = 25.07$, panels a) to c), and at the final simulation time $t\Omega_p = 2000$, panels d) to f). In order to calculate the local $T_{s\parallel}(x,t)$, we divide the entire simulation domain into M bins, and calculate the local temperature of species s at each bin as the second statistical moment of the fluctuations of the parallel ion velocity $\delta v_{s\parallel} = v_{s\parallel}(x) - \langle v_{s\parallel}(x) \rangle$, $\langle \delta v_{s\parallel}^2 \rangle$, where $\langle \rangle$ is an ensemble average only over ions within each bin. For all our calculations of $T_{s\parallel}(x,t)$ we use $M = 4096$. As the burstiness of the magnetic field perturbations increases as we vary θ^* from $360°$ to $2°$, we can see from Figure 4.6 that the heating of both ion species becomes more intense and localised. In panel a) of Figure 4.6, corresponding to the most intermittent case in our simulations, intense localised ion heating can also be seen in the region between $x \approx 330 d_p$ and $x \approx 400 d_p$, while in the rest of the simulation domain there are only a few other regions where ion heating occurs. In contrast, in panel c) of the same figure, corresponding to the non-intermittent case or random phase approximation for the magnetic perturbations, less intense and more spatially homogeneous heating occurs. For the case of intense localised heating, it is not possible to meaningfully define simulation average heating rates and total temperatures at early times, because the variations of the calculated total temperatures are of the same order of magnitude as their mean values. In Karimabadi et al. [2013] are found similar results of intense localised heating of electrons and ions due to coherent structures in the form of current sheets in their 2D and 3D kinetic simulations of collisionless dissipation of energy in decaying turbulence in high-temperature plasmas.

By the end of the hybrid simulations, the ion temperature becomes spatially homogeneous, and it is then possible to meaningfully define total temperatures. In Table 4.1, we present a summary of the final parallel and perpendicular ion temperatures of protons and alpha-particles for all the hybrid simulations with different values of the power spectral exponent γ and levels of intermittency.

In Figure 4.7 we plot these results for the simulation with $\gamma = 1$. Panel a) shows the parallel $(T_{p\parallel})$ and perpendicular $(T_{p\perp})$ proton temperatures at the final simulation time $(t\Omega_p = 2000)$ as functions of θ^*. We see that $T_{p\parallel}$ decreases with
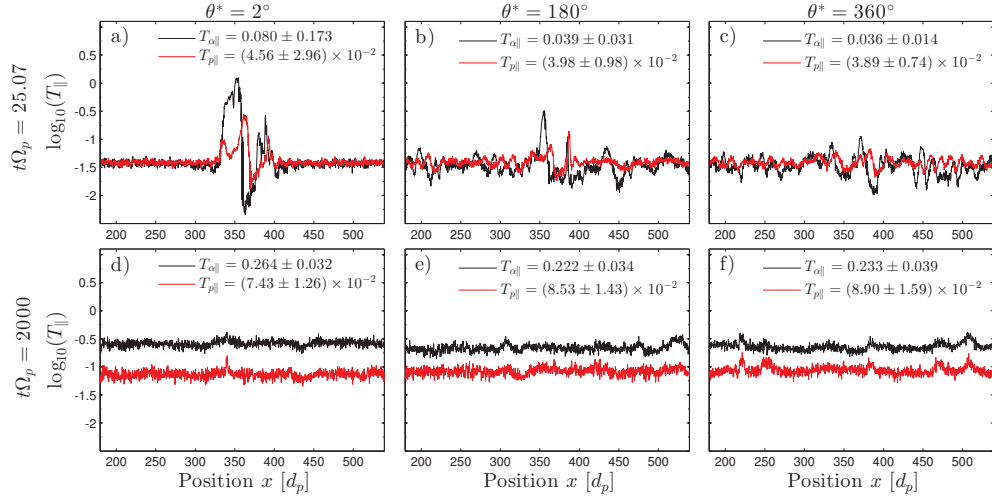
Figure 4.6: Normalised local parallel ion temperature $T_\parallel$ of protons and alpha-particles, plotted as a function of position at early and late times, for three different levels of intermittency. Panels a) to c) show the ion parallel temperatures at the early time $t\Omega_p = 25.07$ from the hybrid simulations with $\theta^* = 2°, 180°$ and $360°$. Intense localised heating occurs for the simulations with high levels of intermittency. Panels d) to f) show the corresponding ion parallel temperatures at final simulation time $t\Omega_p = 2000$; by this time, the heating has become homogeneous, so that average ion temperatures can be defined. The averaged proton and alpha-particle temperatures are calculated for each simulation along with their standard deviations. Large deviations from the mean value of $T_\parallel$ are visible at early times in all the hybrid simulations. By the end of each simulation, the ion temperatures have become more homogeneous in space.

increasing intermittency level. In contrast, $T_{p\perp}$ does not vary significantly when θ^* is changed. Panel b) shows the corresponding case for alpha-particles. We see that $T_{\alpha\parallel}$ increases with increasing intermittency levels, whereas $T_{\alpha\perp}$ decreases. These trends are the same for different values of γ. These variations in the temperatures arise from different levels of intermittency, and this changes the values of the temperature anisotropy $T_\perp/T_\parallel$ for each ion species. This anisotropy is a measurable quantity in the solar wind, which can be used to compare the effects of intermittency on the preferential ion heating. In panels c) and d) of Figure 4.7, we show the corresponding values of $T_\perp/T_\parallel$ for protons and alpha-particles. In these hybrid simulations, the temperature anisotropy for protons $T_{p\perp}/T_{p\parallel} < 1$ always, increasing in value with increasing levels of intermittency. This is shown in Figure 4.7(c). The behaviour of the alpha-particles is different; for the hybrid simulations using $\theta^* = 2°$ we obtained $T_{\alpha\perp}/T_{\alpha\parallel} \approx 1$, independent of the value of the spectral exponent γ (inset of Figure 4.7(b)). For larger values of θ^* the temperature anisotropy takes values larger than one for all the values of the spectral exponent γ, that is, $T_{\alpha\perp}/T_{\alpha\parallel} > 1$.

Table 4.1: Final parallel and perpendicular temperatures of protons and alpha-particles for hybrid simulations in which ion heating is driven by broadband Alfvén wave populations that have different intermittency levels θ^* and spectral exponent γ.

θ^*	Spectral exponent γ $(1/f^\gamma)$	$T_{p\parallel}$ $[m_p V_A^2]$	$T_{p\perp}$ $[m_p V_A^2]$	$T_{\alpha\parallel}$ $[m_p V_A^2]$	$T_{\alpha\perp}$ $[m_p V_A^2]$	$T_{p\perp}/T_{p\parallel}$	$T_{\alpha\perp}/T_{\alpha\parallel}$
2	0	0.090	0.063	0.325	0.325	0.700	1.000
2	1	0.076	0.062	0.270	0.258	0.816	0.956
2	5/3	0.075	0.063	0.267	0.260	0.840	0.974
90	1	0.079	0.063	0.236	0.301	0.798	1.275
180	0	0.098	0.061	0.282	0.371	0.622	1.316
180	1	0.086	0.062	0.223	0.308	0.721	1.381
180	5/3	0.082	0.061	0.213	0.308	0.744	1.446
270	1	0.086	0.061	0.230	0.359	0.709	1.561
360	0	0.097	0.061	0.305	0.414	0.629	1.357
360	1	0.090	0.060	0.234	0.317	0.667	1.354
360	5/3	0.082	0.062	0.198	0.302	0.756	1.525

This is shown in Figure 4.7(d). Observations of the fast solar wind at about 1 AU by the Helios Solar Probes (c.f. Figure 6 of Marsch et al. [1982a]) and by Wind spacecraft (c.f. Figure 2 of Maruca et al. [2012]) show typical values of $T_{\alpha\perp}/T_{\alpha\parallel} \approx 1$; this is only observed in our hybrid simulations for the cases where highly intermittent magnetic field perturbations drive the ion heating. This strongly suggests that the observed values of $T_{\alpha\perp}/T_{\alpha\parallel}$ in the fast solar wind at 1 AU reflect a significant degree of intermittency in the waves driving the ion heating.

In Figure 4.8 we plot the time evolution of the change in energy density of protons, alpha-particles and the magnetic field, for three simulations with $\gamma = 1$. This gives an indication of how strong the wave-particle interactions are in each case. The change in energy density for each ion species and the magnetic field is defined as:

$$\Delta \mathcal{E}_B \;=\; \left\langle \frac{B^2(x,t)}{2\mu_0} \right\rangle_x - \left\langle \frac{B^2(x,0)}{2\mu_0} \right\rangle_x, \tag{4.6}$$

$$\Delta \mathcal{E}_{K_s} \;=\; \frac{1}{L}\left[\left\langle \frac{1}{2} m_s v_s^2(t) \right\rangle_f - \left\langle \frac{1}{2} m_s v_s^2(0) \right\rangle_f \right], \tag{4.7}$$

Here μ_0 is the vacuum permeability, L is the simulation domain length, and $\langle \rangle_x$
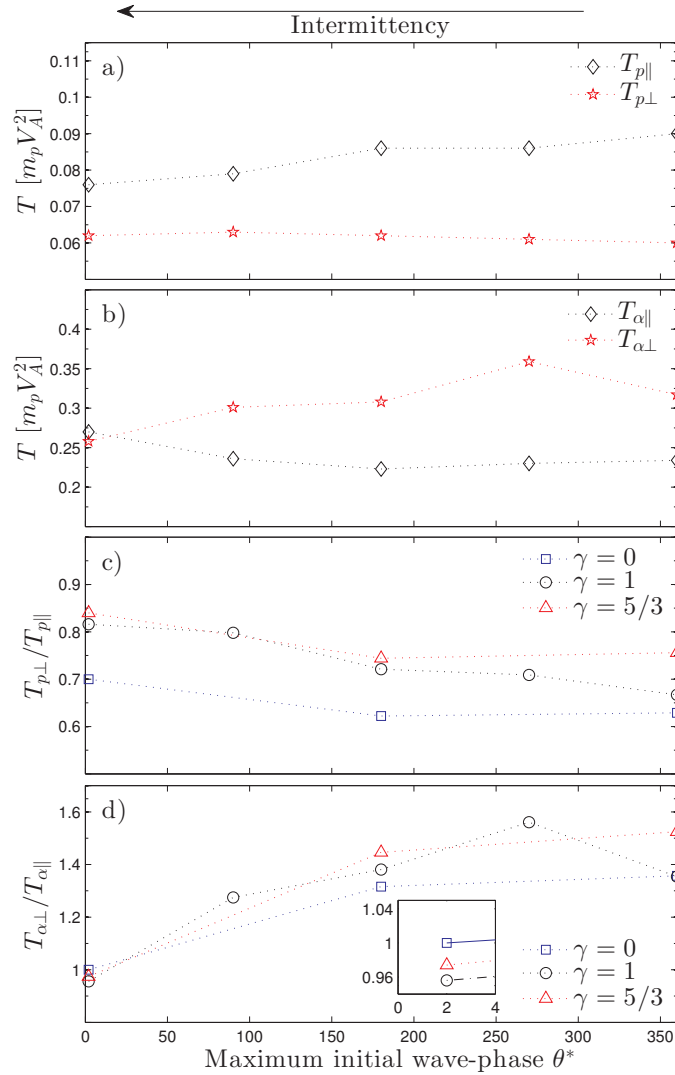
Figure 4.7: Final proton and alpha-particle temperature for different values of θ^* and γ. Panel a): final parallel (black) and perpendicular (red) proton temperature for hybrid simulations with $\gamma = 1$. Panel b): same as panel a) for alpha-particles. Panel c): proton temperature anisotropy. For protons, $T_{p\perp}/T_{p\parallel} < 1$ is always observed in our simulations, and this agrees with observations of the solar wind. Panel d): alpha-particle temperature anisotropy. For alpha-particles, the trend seen in solar wind observations is $T_{\alpha\perp}/T_{\alpha\parallel} \approx 1$; this is only observed for the hybrid simulation with $\theta^* = 2°$, independent of the value of the spectral exponent γ. The inset in this panel shows this.

and $\langle\rangle_f$ refer to averages along the simulation domain and over the ion distribution functions, respectively.

All the simulations show the same qualitative trend: at early times, the alpha-particles transfer some energy to the protons through wave-particle interac-
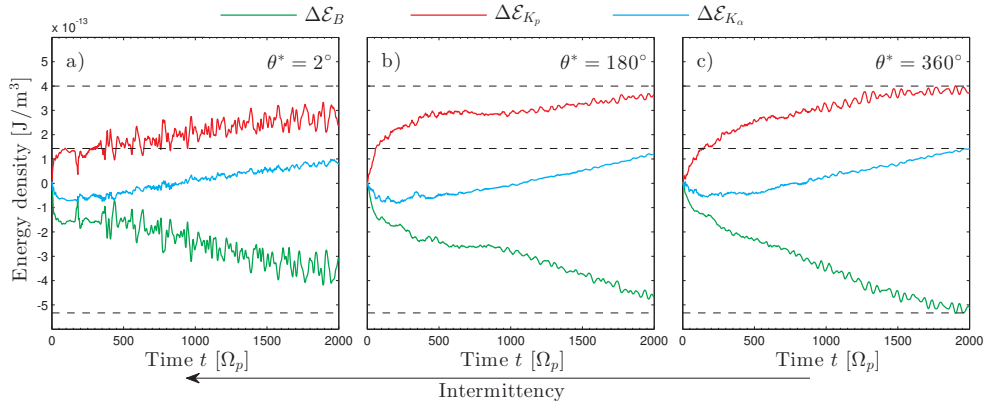
Figure 4.8: Time evolution of change in ion energy density and magnetic field energy density for hybrid simulations, all with an initial $1/f$ broadband spectrum of Alfvén waves, but with different levels of intermittency. From top to bottom: the change in proton energy density $\Delta\mathcal{E}_{K_p}$ (red), the change in alpha-particle energy density $\Delta\mathcal{E}_{K_\alpha}$ (cyan), and the change in magnetic field energy density $\Delta\mathcal{E}_B$ (green). The horizontal dashed lines are plotted only to assist comparison of $\mathcal{E}_{K_p}$, $\Delta\mathcal{E}_{K_\alpha}$ and $\Delta\mathcal{E}_B$ across the different hybrid simulations. All the simulations show the same qualitative trends. At early times, the alpha-particles transfer some energy to the protons through wave-particle interactions. Thereafter there is re-energization of the alpha-particles, while the protons continue to be energized, but at a slower rate. $\Delta\mathcal{E}_{K_p}$ saturates by the end of the simulation time. There is a regular decline in magnetic field energy density.

tions. Then a re-energization of the alpha-particles occurs, while the protons are still being energized, although at a slower rate than at early times. By the end of the simulation that has initially random wave-phases ($\theta^* = 360°$), $\Delta\mathcal{E}_{K_p}$ saturates, that is, the protons are not energized further. However, the alpha-particles continue to gain energy. In the other hybrid simulations, which have non-zero initial intermittency, the saturation of $\Delta\mathcal{E}_{K_p}$ is not observed. The energy density of the electric field, which is of the order of magnitude of 10^{-21} J/m^3, decreases over time in all the hybrid simulations. Shown in Figure 4.8, all the simulations give rise to a similar final energy density of alpha-particles. The case where the initial wave-phases are random ($\theta^* = 360°$) shows the biggest decrease in magnetic field energy, together with the largest proton energy density at the end of the simulation. Conversely, the simulation with highly intermittent Alfvén waves ($\theta^* = 2°$) shows the smallest decrease in magnetic field energy and the smallest proton energy density increase. This implies that, in the former case, the alpha-particles are energised by extracting energy mostly from the magnetic field; whereas, in the latter case, the alpha-particles extract energy from the magnetic field and protons. This is observed consistently across simulations with different values of spectral exponent γ.

Summarizing, we find that different levels of intermittency lead to different temporal and spatial dynamics of the two mechanisms driving preferential ion heating in our simulations: specifically, gyrobunching and ion trapping by the electric field. Also, the ion temperature anisotropy of protons and alpha-particles shows a strong dependence on intermittency levels. We find that intermittency does not allow a meaningful determination of average temperatures and heating rates at early times in our simulations. The net effect of random-phase Alfvén waves in our simulations is to provide a more efficient channel for energy transfer between ions and electromagnetic fields through wave-particle interactions. There are two possible factors for this: first, the wave-particle interactions that energise ions unfold faster for random-phase Alfvén waves than for highly intermittent Alfvén waves; and second, for the same total field energy, the random-phase Alfvén waves fill the simulation domain from early times, whereas the highly intermittent Alfvén wave field generates isolated regions of heating.

4.3.3 Correlation between ion velocity and magnetic field fluctuations

In this section we explore the role of intermittency in the time evolution of the magnetic perturbations in the hybrid simulations. *In situ* observations of the solar wind show that the waves permeating the solar wind are mostly of Alfvénic nature [Belcher and Leverett, 1971; Belcher and Solodyna, 1975; Bruno et al., 1985; Bruno and Carbone, 2013]. That is, the ion velocity fluctuations $\boldsymbol{U}_i$ and magnetic field fluctuations $\delta\boldsymbol{B}$ are correlated, and satisfy Walen's relation $\boldsymbol{U}_i = \pm C_A \delta\boldsymbol{B}$, where $C_A \approx (\mu_0 n m_p)^{-1/2}$. Here the minus (plus) sign refers to pure Alfvénic waves propagating parallel (anti-parallel) to the background magnetic field. Initially, the fluctuations of the magnetic field and ion velocity in the hybrid simulations are purely Alfvénic. Then, as the plasma evolves, there can be parametric decay of the initial Alfvén waves [Araneda et al., 2008; Matteini et al., 2010, 2011], giving way to the excitation of non-Alfvénic waves that interact with the ions in different ways. We study this by calculating the time evolution of the spatial correlation of δB_y and U_{iy}, defined by

$$C(\delta B_y, U_{iy})(t) = C_0 \int_L \delta B_y(x',t) U_{iy}(x',t) dx' \; . \qquad (4.8)$$

Here, the integral is over the entire simulation domain L, and C_0 is a constant that normalizes the correlation values between -1 and 1.

Figure 4.9 shows $C(\delta B_y, U_{iy})$ for the hybrid simulations that generated Fig-

ure 4.8. For all cases $C(\delta B_y, U_{iy}) \approx -1$ at $t\Omega_p = 0$, consistent with the initial condition of pure Alfvén waves propagating parallel to $\boldsymbol{B}_0$. For the simulation with initial random wave-phases (black), the magnetic and ion bulk velocity perturbations become uncorrelated, $C(\delta B_y, U_{iy}) \to 0$. In general, this might happen for two reasons [Bruno and Carbone, 2013]: i) the excitation of non-Alfvénic waves, or ii) the excitation of backscattered Alfvén waves, that is, Alfvén waves propagating anti-parallel to $\boldsymbol{B}_0$ with similar amplitude to those propagating parallel to $\boldsymbol{B}_0$. In our hybrid simulation with initial random wave-phases $C(\delta B_y, U_{iy}) \to 0$ due to the excitation of backscattered left-handed Alfvén waves. This is confirmed by decomposing the magnetic and ion bulk velocity fluctuations into their helicity components [Winske and Omidi, 1993]; we observe Alfvén waves with opposite helicity and similar amplitude. Conversely, in the simulation with initially highly intermittent Alfvén waves (blue), these remain mostly Alfvénic during the simulation; that is, $C(\delta B_y, U_{iy})$ does not departs significantly from -1.
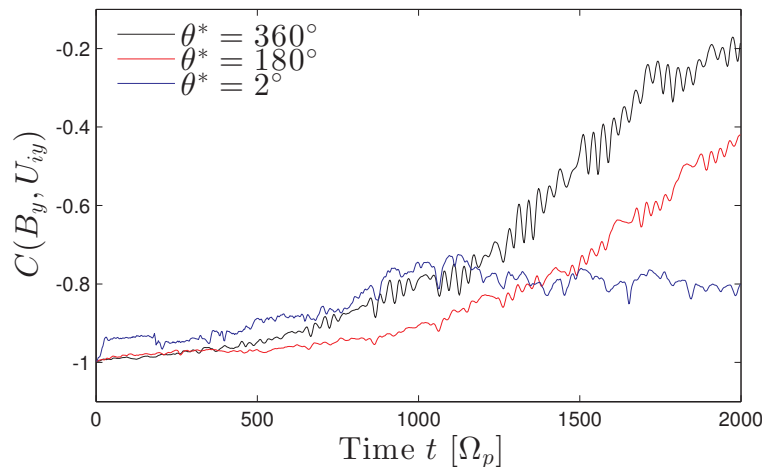
Figure 4.9: Time evolution of the spatial correlation between the ion velocity and magnetic field fluctuations in the hybrid simulations of the solar wind. Initially, $C(\delta B_y, U_{iy}) \approx -1$, consistent with the initial condition of pure Alfvén waves propagating parallel to $\boldsymbol{B}_0$. For the case where the initial wave-phases are random (black): $\theta^* = 360°$ the broadband spectrum of Alfvén waves decay into backscattered Alfvénic waves, that is, Alfvén waves propagating anti-parallel to $\boldsymbol{B}_0$ with similar amplitude to those propagating parallel to $\boldsymbol{B}_0$, which reduce the correlation $C(\delta B_y, U_{iy}) \to 0$. In the case with highly intermittent Alfvén waves (blue): $\theta^* = 2°$ the plasma waves remain mostly Alfvénic throughout the simulation.

Summarizing, we find that the dynamics of the ion bulk velocity and magnetic field fluctuations depend on intermittency levels of the electromagnetic fields. Large amplitude backscattered Alfvén waves only are excited in the simulation with non-intermittent Alfvén waves.

4.3.4 Local intermittency measure of magnetic field fluctuations

In this section we study the dynamics of intermittency in our hybrid simulations of preferential ion heating in the solar wind. Intermittency in the solar wind can be studied using statistical methods such as structure functions (SF) [Hnat et al., 2007; Kiyani et al., 2007; Leonardis et al., 2013] and probability distribution functions (PDFs) [Hnat et al., 2002, 2003; Nicol et al., 2009; Wu et al., 2013; Subedi et al., 2014] of the fluctuations of the solar wind parameters. These methods allow us to characterise intermittency in the solar wind, provided that we have large data sets of the solar wind parameters to obtain reliable estimates of these statistical quantities.

Here, we use the local intermittency measure (LIM) to study intermittency in the magnetic field in our hybrid simulations. The LIM is based on wavelet analysis, which allow us to identify intermittent (bursty) behavior of the magnetic field at different spatial scales, and to follow in space and time intermittent structures of the magnetic field. In our case, the LIM uses wavelet analysis to decompose the magnetic field into contributions of both space and scale at different simulation times; for a complete review of wavelet analysis see Torrence and Compo [1998]. The LIM, contrary to SF and PDFs methods, can be used to study intermittency in scenarios where no large data sets of the solar wind parameters exist. This method was first introduced in Farge [1992] to study the dynamics of coherent (bursty) structures in the solar wind, and to measure their contribution to the energy spectrum. More recently, the LIM has been used in Dinkelaker and MacKinnon [2013a,b] to study cascade and reverse-cascade (avalanche) processes in solar flares.

To calculate the LIM of the magnetic field in our simulations, we first perform a wavelet transformation of either magnetic field component B_y, or B_z along the simulation domain (the x-axis in our simulations). Here, we only show the results for B_y, given that the LIM of B_z shows the same features. Following Farge [1992] and Dinkelaker and MacKinnon [2013a], we use the 4th-order Paul wavelet function in our definition of the LIM. We define the LIM at position x and spatial scale l for a given simulation time t as:

$$\mathrm{LIM}(x,l,t) = \frac{|\hat{w}(x,l,t)|^2}{\langle |\hat{w}(x,l,t)|^2 \rangle_x}. \tag{4.9}$$

Here, the average $\langle \rangle_x$ is over all the simulation domain, and $\hat{w}(x,l,t)$ is the Paul wavelet coefficient of B_y at position x and spatial scale l given by:

$$\hat{w}(x,l,t) = \int_L B_y(x',t) \Psi_m^* \left(\frac{x'-x}{l} \right) dx', \tag{4.10}$$

where the integral is calculated over the entire simulation domain L, and $\Psi_m^*(x)$ is the complex conjugate of the Paul wavelet function of order m defined as:

$$\Psi_m(x) = \Gamma(m+1)\frac{\left(\sqrt{-1}\right)^m}{\left(1 - \sqrt{-1}x\right)^{m+1}}. \tag{4.11}$$

Here, $\mathrm{LIM}(x,l) = 1$ for all x and l means that there is no intermittent behavior of the magnetic field; that is, the magnetic field energy of B_y is homogeneously distributed along all the simulation domain for all spatial scales l. On the contrary, $LIM(x,l) = 10$ means that at position x and spatial scale l the magnetic field energy of B_y is 10 times larger than its mean value along the simulation domain.

Following Dinkelaker and MacKinnon [2013a], we use LIM^2 as an estimate of the kurtosis of the fluctuations of B_y. As shown in Bruno et al. [1999], the threshold value $\mathrm{LIM}^2 > 3$, indicates large fluctuations of the magnetic field that yield to intermittent behavior. Figure 4.10 show LIM^2 of the magnetic field component B_y for the hybrid simulations with $\theta^* = 2°, 180°$ and $360°$. We only show the region $180d_p \leq x \leq 540d_p$ of the simulation domain; we observe similar behavior in the rest of the simulation domain. In this figure blue (red) colour indicates small (large) intermittent structures of the magnetic field at position x and spatial scale l. Only values of $\mathrm{LIM}^2 > 3$ are shown in colours.

As is seen in Fig. 4.10, the LIM^2 shows different intermittent behavior of B_y depending on the value of θ^*. At early times, we observe intermittent structures with $\mathrm{LIM}^2 \geq 40$ for all l at $x \approx 350d_p$ in the simulation with $\theta^* = 2°$. At later times, intermittent structures with $\mathrm{LIM}^2 < 15$ develop along all the simulation domain at scales $l \leq 400d_p$. By the end of the simulation more intermittent structures with $\mathrm{LIM}^2 < 15$ develop at larger scales $400d_p < l < 700d_p$. In the case of initially random phase Alfvén waves $\theta^* = 360$, the LIM shows the existence of less intense and more homogeneously distributed intermittent structures at early times. Also, we observe intermittent structures with $\mathrm{LIM}^2 \geq 40$ only for $l \geq 600d_p$ at $x \approx 350d_p$, and less intense intermittent structures with $\mathrm{LIM}^2 < 15$ in some other regions of the simulation domain for $l < 600d_p$. At later times, intermittent structures with $\mathrm{LIM}^2 < 15$ develop at scales $l \leq 200d_p$; at the same time, fewer but more intense intermittent structures with $\mathrm{LIM}^2 > 15$ develop at scales $200d_p < l < 800d_p$. By the end of the simulation we observe intermittent structures mainly with $\mathrm{LIM}^2 < 15$ along the simulation domain at scales $l < 600d_p$, and few intermittent structures with $\mathrm{LIM}^2 < 5$ at larger spatial scales $l > 600d_p$.

We observe good correlation between local parallel ion heating (c.f. Fig. 4.6) and intermittent structures of the magnetic field with $\mathrm{LIM}^2 \geq 15$ at scales $l \geq 200d_p$.

We also observe good correlation between these intermittent structures and the regions in the simulation domain where the ions are accelerated by gyrobunching and ion trapping by the electric field (c.f. Fig. 4.5).

Summarising, different values of θ^* lead to different temporal and spatial dynamics of intermittent structures of the magnetic field in our simulations. Furthermore, we find good correlation between localised intense intermittent structures of the magnetic field and the occurrence of ion heating along the background magnetic field.
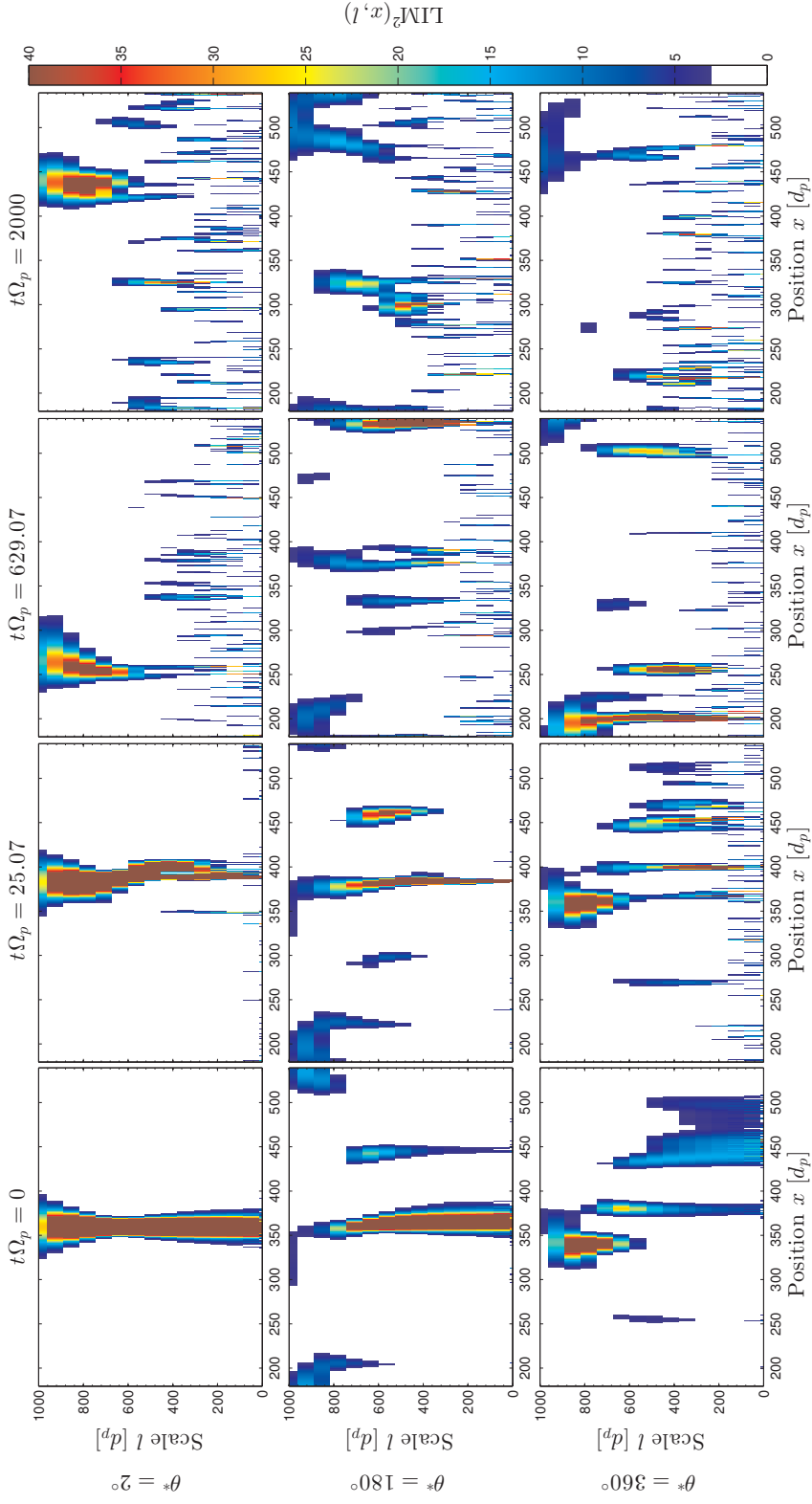
Figure 4.10: Local intermittency measure of the magnetic field component B_y for three hybrid simulations with different levels of intermittency. Panels from top to bottom: the top panels show $LIM^2(x,l)$ of B_y for the simulation with $\theta^* = 2°$ at the simulation times $t\Omega_p = 0, 25.07, 629.07$ and 2000. The middle and bottom panels show the corresponding $LIM^2(x,l)$ of B_y for the simulations with $\theta^* = 180°$ and $360°$, respectively. The spatial and temporal dynamics of intermittent structures of the magnetic field component B_y are different in each case. The LIM of B_z shows the same features.

104

4.4 Discussion

In this chapter we presented the results of the first study of preferential ion heating driven by $1/f^\gamma$ broadband spectra of Alfvén waves that have different levels of intermittency for a given value of the spectral exponent γ. Intermittency is incorporated in our model through non-random phase relationships between the modes which together comprise an initial $1/f^\gamma$ spectrum of Alfvén waves. Our hybrid simulations resolve the full kinetic dynamics of ions, allowing us to study in detail the effects of intermittency on the mechanisms that might be responsible for the observed preferential ion heating in the fast solar wind.

We find that:

- Gyrobunching and ion trapping by the electric field are the two mechanisms underlying preferential ion heating in our simulations (Figures 4.4 and 4.5).

- Different levels of intermittency for a given broadband spectrum of Alfvén waves lead to different temporal and spatial dynamics of the mechanisms underlying preferential ion heating (Figures 4.2 and 4.3).

- The proton and alpha-particle temperature anisotropy $T_\perp/T_\parallel$ shows strong dependence on the level of intermittency of the electromagnetic fields. We find $T_{p\perp}/T_{p\parallel} < 1$ in all our simulations, increasing in value as the intermittency level increases; and $T_{\alpha\perp}/T_{\alpha\parallel} > 1$ for all the values of θ^* except for the most intermittent case $\theta^* = 2°$. This result, $T_{\alpha\perp}/T_{\alpha\parallel} \approx 1$, is consistent with what is typically seen in observations [Marsch et al., 1982a,b; Maruca et al., 2012; Maruca, 2012].

- The net effect of random-phase, hence non-intermittent, Alfvén waves in our simulations is to provide a more efficient channel for energy transfer between ions and electromagnetic fields through wave-particle interactions. This may result from the fast time scales at which the wave-particle interactions that energise ions unfold; and from how the random-phase Alfvén waves fill the simulation domain at early times. On the other hand, highly intermittent Alfvén waves generate isolated regions of heating, and this seems to favour energy transfer from protons to alpha-particles (Figure 4.8).

- The dynamics of the velocity and magnetic field fluctuations depend on the initial level of intermittency of the broadband spectrum of Alfvén waves driving the heating. Large amplitude backscattered Alfvén waves only are excited in the simulation with non-intermittent Alfvén waves.

- Intermittent Alfvén waves produce strong localised heating (Figure 4.6), and in consequence we cannot meaningfully define average heating rates and total temperatures at early times in our simulations. This suggests that in the intermittent solar wind similar localised heating might occur, making it difficult to obtain good estimates of mean ion temperatures and ion heating rates, which later are used in theoretical and numerical modelling of the solar wind.

- Our results do not in general show any trend with different spectral exponents γ, consistent with Maneva et al. [2013]. The only clear trend, as expected, relates to the energy transfer between the magnetic field and the alpha-particles, which is found to be larger (smaller) for $\gamma = 0$ ($\gamma = 5/3$). This follows from the fact that for $\gamma = 0$ ($\gamma = 5/3$) there is more (less) energy available at modes close to ion cyclotron resonance, that is, $\omega \sim \Omega_\alpha$.

- The spatial and temporal dynamics of intermittent structures of the magnetic field strongly depend on the initial level of intermittency of the magnetic field. Furthermore, we find good correlation between localised intense intermittent structures of the magnetic field and the occurrence of ion heating along the background magnetic field (Figs. 4.6 and 4.10).

There is good agreement between our results and Maneva et al. [2013] for the case where the broadband spectrum of Alfvén waves is random-phase. They found that if solar wind expansion is included in the simulations, the value of $T_{\alpha\perp}/T_{\alpha\parallel}$ decreases. This suggests that simulations that include both intermittency and solar wind expansion, might lead to values of $T_{\alpha\perp}/T_{\alpha\parallel}$ closer to their typical observed values.

Chapter 5

Conclusions

In this thesis we studied in detail the dynamics of energetic ions in scenarios relevant to magnetic confinement fusion (MCF) plasmas and solar wind plasmas. An adequate level of description for the plasma for this purpose was the hybrid approximation for the plasma, which treats ions as kinetic particles and electrons as a charge-neutralising massless fluid. Our simulations of MCF plasmas effectively reproduced the observations of ion cyclotron emission (ICE) in JET, a radiative instability driven by fusion-born alpha-particles in deuterium-tritium plasmas, and provided fresh insights into the underlying physics of this instability in its linear and nonlinear stage. This gives further support to ICE to being used as a non-perturbative diagnostic of fusion-born alpha-particles in future thermonuclear fusion reactors. Similarly, we took a step forward in the study of preferential ion heating in solar wind, observed as the formation of ion beams along the local magnetic field of the solar wind, by performing, for the first time, simulations of preferential ion heating driven by broadband spectra of Alfvén waves including intermittency in a self-consistent way. Our results showed that intermittency can significantly modify the mechanisms underlying preferential heating in solar wind.

In Chapter 1, the most frequently used levels of description for the plasma for studying MCF plasmas and solar wind plasmas were presented, with special emphasis on the hybrid approximation for the plasma. Later, perturbative and non-perturbative instabilities in MCF plasmas, which are used to diagnose some plasma parameters, were discussed. In this context, we introduced ICE as observed in deuterium-tritium fusion plasmas, together with the magnetoacoustic cyclotron instability (MCI), the leading instability underlying ICE in JET and TFTR. In this chapter we also presented a brief but complete description of the solar wind through remote and *in situ* observations of the solar wind made during the last four

decades. We highlighted three features of the solar wind, namely, power laws of the solar wind fluctuations, intermittency, and preferential ion heating in the solar wind. These solar wind observations are put together in our simulations of preferential ion heating driven by broadband spectra of intermittent Alfvén waves in Chapter 4.

In Chapter 2 we introduced PROMETHEUS++, a new code that uses the hybrid approximation for the plasma to study MCF plasmas and solar wind plasmas. In this chapter the programming paradigms and numerical schemes used in PROMETHEUS++ were explained in detail. Three well known problems in plasma physics were used to benchmark the code: the warm plasma dispersion relation, the resonant electromagnetic ion-ion instability, and the electromagnetic ion cyclotron beam anisotropy. The results of these tests showed that PROMETHEUS++ is robust with good energy conservation, and allows us to perform plasma simulations with good resolution and accuracy over a wide range of plasma configurations.

5.1 Results on the hybrid simulations of the MCI in relation to ICE in D-T JET plasmas

In Chapter 3, the ion cyclotron emission (ICE) was studied through hybrid simulations of the magnetoacoustic cyclotron instability (MCI) in the context of deuterium-tritium (D-T) plasmas in JET [Cottrell et al., 1993; McClements et al., 1999]. The hybrid approximation for the plasma enabled us to pursue simulations of the MCI longer in time and deep into the nonlinear phase of the MCI with respect to previous fully kinetic simulations of the MCI [Cook et al., 2013]. Through our hybrid simulations of the MCI, we recovered some features of the measured ICE in JET, and confirmed some predictions of the linear theory of the MCI [Dendy et al., 1995], namely, the excitation of fast Alfvén waves at simultaneous cyclotron harmonics of the alpha-particles in the range $5\Omega_\alpha \leq \omega \leq 12\Omega_\alpha$, in the linear stage of the MCI (c.f. Fig. 3.1). Importantly, by going deep into the nonlinear stage of the MCI we recovered the lower spectral peaks in the range of frequencies $\omega = \Omega_\alpha$ to $\omega = 3\Omega_\alpha$, which are not predicted to be linearly unstable according to the analytical theory of the MCI, but are present in the measured ICE intensity in JET. These lower spectral peaks are driven by nonlinear interactions between higher harmonics localized around $\omega = 11\Omega_\alpha$ (c.f. Figs. 3.3 and 3.6). Also in the nonlinear stage of the MCI, we observed re-energisation of the minority alpha-particle population driven by waves excited early on in the simulations by the alpha-particles. Furthermore, a correlation analysis between the parallel magnetic field $\delta B_\parallel$ and the perpendicular electric field E_x components revealed that self-modulation of the phase shift between these

components of the electromagnetic fields occurs as the hybrid simulations enter the nonlinear stage of the MCI (c.f. Fig. 3.5).

We studied the scaling properties of the MCI with alpha-particle concentration, yielding a good match to the scaling of ICE intensity that is measured in JET and TFTR. First, the scaling of the linear growth rates of the MCI, as inferred from the hybrid simulations at early times, with alpha-particle concentration was investigated (c.f. Fig. 3.11). We found that the linear growth rates of the modes excited at the cyclotron harmonics from $\omega = 9\Omega_\alpha$ up to $\omega = 12\Omega_\alpha$ show square root scaling with ξ_α, while the mode at $\omega = 7\Omega_\alpha$ exhibits linear scaling. Next, the scaling of the magnetic field energy density with alpha-particle concentration was studied in detail. The simulation results showed linear scaling with ξ_α for the modes of the electromagnetic fields excited at consecutive cyclotron harmonics of the minority alpha-particles from the seventh harmonic up to the twelfth harmonic. These results are in clear agreement with observations of ICE intensity in JET and TFTR.

Finally, we performed the first hybrid simulations of the MCI for conditions relevant to core D-T plasmas in JET. We found that the MCI can efficiently operate in core D-T JET-like plasmas only when the alpha-particle velocity distribution significantly departs from an isotropic spherical-shell-like distribution in velocity space. These simulations represent the first precedent of a numerical study of ICE in JET core plasmas.

We infer that it is very probable that the plasma physics process underlying ICE is the MCI. This was strongly suggested by the original analysis of JET and TFTR D-T plasma observations of ICE, in terms of the linear analytical theory of the MCI, and appears to be confirmed by the first principles large scale numerical simulations using PIC [Cook et al., 2013] and, here, hybrid codes. This study strengthens our understanding of the emission mechanism and provides further support to ICE for being exploited as a diagnostic of confined and lost fusion alpha-particles in future D-T plasmas in JET and ITER, as has been proposed [Dendy and McClements, 2015; McClements et al., 2015].

5.1.1 Limitations and future work

Our study of ICE through hybrid simulations of the MCI is limited by the current capabilities of PROMETHEUS++. Future work will include the extension of this study to the more computationally intensive full three-dimensional case, so as to incorporate realistic tokamak spatial and magnetic field geometry. This will allow us to study in detail the relationships between parallel and perpendicular propagating

electromagnetic waves excited by the MCI. Also, new settings of our simulations including sources and replenishment of energetic alpha-particles are desirable.

5.2 Results on hybrid simulations of preferential ion heating due to intermittent magnetic fields in the solar wind

In Chapter 4 we carried out the first study of preferential ion heating driven by $1/f^{\gamma}$ broadband spectra of Alfvén waves with different levels of intermittency, which were incorporated through non-random phase relationships between the modes comprising the broadband spectra of Alfvén waves. All the hybrid simulations had the same initial electromagnetic energy related to the broadband spectrum of intermittent Alfvén waves, and the same initial condition for thermal protons and alpha-particles. Therefore, the only variable in our simulations was the intermittency level of the electromagnetic fields, as explained in Sec. 4.2.1. The plasma parameters used in our simulations were chosen to be those of the fast solar wind as measured at 1 AU.

First, we studied the mechanisms underlying preferential ion heating in our hybrid simulations. We found that different levels of intermittency for a given broadband spectrum of Alfvén waves lead to different temporal and spatial dynamics of the mechanisms underlying preferential ion heating, namely, gyrobunching and ion trapping by the electric field. (Figs. 4.2 to 4.5). These mechanisms initially produced strong localised heating of protons and alpha-particles (Figure 4.6), and consequently we could not meaningfully define average heating rates and total temperatures at early times in our simulations. Should this strong localised heating occur in the intermittent solar wind, this would make it difficult to obtain good estimates of mean ion temperatures and ion heating rates. By the end of the simulation, however, the protons and alpha-particles temperature became spatially homogeneous; then we could meaningfully define total temperatures in order to study the temperature anisotropy $T_{\perp}/T_{\parallel}$ in our simulations. We found that $T_{\perp}/T_{\parallel}$ shows strong dependence on the level of intermittency of the electromagnetic fields (c.f. Fig. 4.7). $T_{p\perp}/T_{p\parallel} < 1$ is found in all our simulations, consistent with observations [Marsch et al., 1982b; Maruca et al., 2012; Maruca, 2012] and previous studies [Maneva et al., 2013] of preferential ion heating in solar wind. Only when highly intermittent Alfvén waves were used, we observed $T_{\alpha\perp}/T_{\alpha\parallel} \approx 1$, which is consistent with observations of the fast solar wind at 1 AU [Marsch et al., 1982a; Maruca, 2012].

All the other simulations with less intermittent Alfvén waves exhibited $T_{\alpha\perp}/T_{\alpha\parallel} > 1$.

Next, we studied the energy transfer between ions and electromagnetic fields. We observed that this was strongly affected by the different levels of intermittency. The net effect of random-phase, hence non-intermittent, Alfvén waves in our simulations was to provide a more efficient channel for energy transfer between ions and electromagnetic fields through wave-particle interactions; whereas highly intermittent Alfvén waves favoured energy transfer from protons to alpha-particles (Figure 4.8).

Then, we moved to the study of the dynamics of the velocity and magnetic field fluctuations. This showed that the dynamics of these fluctuations depend on the initial level of intermittency of the broadband spectrum of Alfvén waves driving the heating. Large amplitude backscattered Alfvén waves, that is, Alfvén waves propagating anti-parallel to the background magnetic field with opposite helicity and similar amplitude to those propagating parallel to the background magnetic field, were observed to be excited only for the simulation with initial non-intermittent Alfvén waves. Conversely, in the simulation with initially highly intermittent Alfvén waves neither backscattered Alfvén waves nor non-Alfvénic waves were excited during the simulation.

Finally, we studied the evolution of intermittency in our hybrid simulations of preferential ion heating in the solar wind using the local intermittency measure (LIM). The spatial and temporal dynamics of intermittent structures of the magnetic field showed strong dependence on the initial level of intermittency of the magnetic field. Furthermore, we found a correlation between localised intense intermittent structures of the magnetic field and the occurrence of ion heating along the background magnetic field (Figs. 4.6 and 4.10).

Importantly, our results did not show any trend with different spectral exponents γ, consistent with previous studies that used different spectral exponents γ for the broadband spectrum of waves driving the ion heating [Maneva et al., 2013].

5.2.1 Limitations and future work

The present study represents the first attempt to investigate the role of intermittency in the heating of the solar wind. We have not attempted to capture specific intermittency properties of the observed solar wind. Future work might include the use of more realistic models of intermittency to generate the broadband spectra of Alfvén waves to drive the heating [Subedi et al., 2014].

List of Tables

List of Figures

114

119

121

Bibliography

K. Akimoto, D. Winske, T. G. Onsager, M. F. Thomsen, and S. P. Gary. Steepening of Parallel Propagation Hydromagnetic Waves Into Magnetic Pulsations: A Simulation Study. *Journal of Geophysical Research*, 96(A10):17599, 1991. 8

O. Alexandrova, C. H K Chen, L. Sorriso-Valvo, T. S. Horbury, and S. D. Bale. Solar wind turbulence and the role of ion instabilities. *Space Science Reviews*, 178:101–139, 2013. ISSN 00386308. 24, 83

J. Araneda, Y. Maneva, and E. Marsch. Preferential Heating and Acceleration of α Particles by Alfvén-Cyclotron Waves. *Physical Review Letters*, 102(17):175001, Apr 2009. ISSN 0031-9007. 8, 83

J. A.. Araneda, E. Marsch, and A. F.-Viñas. Proton core heating and beam formation via parametrically unstable Alfvén-cyclotron waves. *Physical Review Letters*, 100(12):125003, Mar 2008. ISSN 0031-9007. 83, 99

A. Y. Aydemir. A unified Monte Carlo interpretation of particle simulations and applications to non-neutral plasmas. *Physics of Plasmas*, 1(4):822, 1994. 67, 68

M.A. Barnes. *Trinity: A Unified Treatment of Turbulence, Transport, and Heating in Magnetized Plasmas.* PhD, University of Maryland, College Park, 2009. 6

J. W. Belcher and D. Jr. Leverett. Large-Amplitude Alfvén Waves in the Interplanetary Medium, 2. *Journal of Geophysical Research*, 76(16):3534, 1971. 21, 22, 82, 85, 99

J. W. Belcher and C. V. Solodyna. Alfvén waves and directional discontinuities in the interplanetary medium. *Journal of Geophysical Research*, 80(I):181, 1975. 21, 22, 82, 85, 99, 114

V. S. Belikov and Y. I. Kolesnichenko. Magnetoacoustic cyclotron instability in a thermonuclear plasma. *Sov. Phys. Tech. Phys., Engl. Transl.*, 20:1146, 1976. 16, 54

C. K. Birdsall and A. B. Langdon. *Plasma Physics via Computer Simulation*. Series in Plasma Physics and Fluid Dynamics. Taylor & Francis, 2004. ISBN 9780750310253. 67

A. Bottino, A. G. Peeters, R. Hatzky, S. Jolliet, B. F. McMillan, T. M. Tran, and L. Villard. Nonlinear low noise particle-in-cell simulations of electron temperature gradient driven turbulence. *Physics of Plasmas*, 14(1):1–4, 2007. 68

R. Bruno and V. Carbone. The Solar Wind as a Turbulence Laboratory. *Living Reviews in Solar Physics*, 2:4, 2013. ISSN 1614-4961. 19, 21, 23, 24, 82, 84, 85, 99, 100, 114

R. Bruno, B. Bavassano, and U. Villante. Evidence for long period Alfvén waves in the inner solar system. *Journal of Geophysical Research A: Space Physics*, 90(4): 4373–4377, 1985. 21, 82, 85, 99

R. Bruno, B. Bavassano, E. Pietropaolo, V. Carbone, and P. Veltri. Effects of intermittency on interplanetary velocity and magnetic field fluctuations anisotropy. *Geophysical Research Letters*, 26(20):3185–3188, 1999. 23, 102

R. Bruno, V. Carbone, S. Chapman, B. Hnat, A. Noullez, and L. Sorriso-Valvo. Intermittent character of interplanetary magnetic field fluctuations. *Physics of Plasmas*, 14(3):032901, 2007. 24, 82

R. Bruno, V. Carbone, Z. Vörös, R. DAmicis, B. Bavassano, M. B. Cattaneo, A. Mura, A. Milillo, S. Orsini, P. Veltri, L. Sorriso-Valvo, T. Zhang, H. Biernat, H. Rucker, W. Baumjohann, D. Jankovičová, and P. Kovács. Coordinated Study on Solar Wind Turbulence During the Venus-Express, ACE and Ulysses Alignment of August 2007. *Earth, Moon, and Planets*, 104(1-4):101–104, Dec 2009. ISSN 0167-9295. 23, 82

O. Buneman. TRISTAN: The 3-D electromagnetic particle code. In H. Matsumoto and Y Omura, editors, *Computer Space Plasma Physics: Simulations and Software*, pages 67–84. Terra, Tokyo, 1993. 36

L. F. Burlaga. Intermittent turbulence in the solar wind. *Journal of Geophysical Research*, 96(A4):5847–5851, 1991. 25

L. Carbajal, S. C. Chapman, R. O. Dendy, J. W. S. Cook, and B. Reman. PROMETHEUS++ code, 2013. www2.warwick.ac.uk/fac/sci/physics/research/cfsa/people/\carbajal_gomez/plasma_modelling. 31

L. Carbajal, R. O. Dendy, S. C. Chapman, and J. W. S. Cook. Linear and nonlinear physics of the magnetoacoustic cyclotron instability of fusion-born ions in relation to ion cyclotron emission. *Physics of Plasmas*, 21(1):012106, 2014. 8, 66, 70

S. Cauffman, R. Majeski, K. G. McClements, and R. O. Dendy. Alfvenic behaviour of alpha particle driven ion cyclotron emission in TFTR. *Nuclear Fusion*, 35(12): 1597, 1995. 15, 53, 58, 80

B. Chapman, G. Jost, and R. van der Pas. *Using OpenMP: Portable Shared Memory Parallel Programming*. Scientific and engineering computation. MIT Press, 2008. ISBN 9780262033770. 33

S. C. Chapman and B. Hnat. Quantifying scaling in the velocity field of the anisotropic turbulent solar wind. *Geophysical Research Letters*, 34:L17103, 2007. 24, 82

S. E. Clark, D. Winske, D. B. Schaeffer, E. T. Everson, a. S. Bondarenko, C. G. Constantin, and C. Niemann. Hybrid simulation of shock formation for super-Alfvenic expansion of laser ablated debris through an ambient, magnetized plasma. *Physics of Plasmas*, 20:082129, 2013a. 8

S. E. Clark, D. Winske, D. B. Schaeffer, E. T. Everson, A. S. Bondarenko, C. G. Constantin, and C. Niemann. Hybrid simulation of shock formation for super-Alfvénic expansion of laser ablated debris through an ambient, magnetized plasma. *Physics of Plasmas*, 20(8):082129, 2013b. 8

J. W. S. Cook, R. O. Dendy, and S. C. Chapman. Gyrobunching and waveparticle resonance in the lower hybrid drift instability. *Plasma Physics and Controlled Fusion*, 53(7):074019, Jul 2011. ISSN 0741-3335. 91

J. W. S. Cook, R. O. Dendy, and S. C. Chapman. Particle-in-cell simulations of the magnetoacoustic cyclotron instability of fusion-born alpha-particles in tokamak plasmas. *Plasma Physics and Controlled Fusion*, 55(6):065003, 2013. 54, 55, 58, 63, 70, 80, 108, 109

G. A. Cottrell and R. O. Dendy. Superthermal radiation from fusion products in JET. *Phys. Rev. Lett.*, 60:33–36, Jan 1988. 14, 15, 53, 63, 113

G. A. Cottrell, V. P. Bhatnagar, O. Da Costa, R. O. Dendy, J. Jacquinot, K. G. McClements, D. C. McCune, M. F. F. Nave, P. Smeulders, and D. F. H. Start. Ion cyclotron emission measurements during JET deuterium-tritium experiments. *Nuclear Fusion*, 33(9):1365, 1993. 15, 17, 53, 54, 56, 63, 66, 72, 77, 80, 108

B. De Pontieu, S. W. Mcintosh, M. Carlsson, V. H. Hansteen, T. D. Tarbell, C. J. Schrijver, A. M. Title, R. A. Shine, S. Tsuneta, Y. Katsukawa, K. Ichimoto, Y. Suematsu, T. Shimizu, and S. Nagata. Chromospheric Alfven waves trong enough to power the solar wind. *Science*, 318(5856):1574–1577, 2007. 21, 82, 85

R. O. Dendy and K. G. Mcclements. Ion cyclotron wave emission at the quasi-perpendicular bow shock. *Journal of Geophysical Research*, 98:15531, 1993. 18

R. O. Dendy and K. G. McClements. Ion cyclotron emission from fusion-born ions in large tokamak plasmas: a brief review from JET and TFTR to ITER. *Plasma Physics and Controlled Fusion*, 57:044002, 2015. 109

R. O. Dendy, C. N. LashmoreDavies, and K. F. Kam. A possible excitation mechanism for observed superthermal ion cyclotron emission from tokamak plasmas. *Physics of Fluids B: Plasma Physics*, 4(12):3996–4006, 1992. 16, 54, 71, 72, 77

R. O. Dendy, C. N. LashmoreDavies, and K. F. Kam. The magnetoacoustic cyclotron instability of an extended shell distribution of energetic ions. *Physics of Fluids B: Plasma Physics*, 5(7):1937, 1993. 16, 54, 77

R. O. Dendy, C. N. Lashmore-Davies, K. G. McClements, and G. A. Cottrell. The excitation of obliquely propagating fast Alfvén waves at fusion ion cyclotron harmonics. *Physics of Plasmas*, 1(6):1918–1928, 1994a. 80

R. O. Dendy, K. G. McClements, C. N. Lashmore-Davies, R. Majeski, and S. Cauffman. A mechanism for beam-driven excitation of ion cyclotron harmonic waves in the Tokamak Fusion Test Reactor. *Physics of Plasmas*, 1(10):3407–3413, 1994b. 16, 54, 63

R. O. Dendy, K. G. McClements, C. N. Lashmore-Davies, G. A. Cottrell, R. Majeski, and S. Cauffman. Ion cyclotron emission due to collective instability of fusion products and beam ions in TFTR and JET. *Nuclear Fusion*, 35(12):1733, 1995. 15, 16, 17, 53, 54, 56, 57, 63, 66, 70, 80, 108, 113, 118

R. D'Inca. Ion cyclotron emission on ASDEX upgrade. Dec 2014. 15, 54, 75

R. D'Inca, M. Garcia-Munoz, G. Tardini, and J.-M. Noterdaeme. *Proc. 38th EPS Conf. on Plasma Phys. (Strasbourg, France)*, page P1.053, 2011. 15, 54

A. N. Dinkelaker and A. L. MacKinnon. Wavelets, Intermittency and Solar Flare Hard X-rays 1. Local Intermittency Measure in Cascade and Avalanche Scenarios. *Solar Physics*, 282(2):471–481, Nov 2013a. 101, 102

A. N. Dinkelaker and A. L. MacKinnon. Wavelets, Intermittency and Solar Flare Hard X-rays 2. LIM Analysis of High Time Resolution BATSE Data. *Solar Physics*, 282(2):483–501, Nov 2013b. 101

M Farge. Wavelet Transforms And Their Applications To Turbulence. *Annual Review of Fluid Mechanics*, 24(1):395–457, Jan 1992. 26, 101

U. Frisch. *Turbulence: The Legacy of A. N. Kolmogorov.* Cambridge University Press, 1995. ISBN 9780521457132. 24, 25

T. Fülöp and M. Lisak. Ion cyclotron emission from fusion products and beam ions in the tokamak fusion test reactor. *Nuclear Fusion*, 38(5):761–773, 1998. 16, 54

G. Gilboa. A Spectral Approach to Total Variation. In A. Kuijper, K. Bredies, T. Pock, and H. Bischof, editors, *Scale Space and Variational Methods in Computer Vision: 4th International Conference, SSVM 2013, Schloss Seggau, Leibnitz, Austria, June 2-6, 2013. Proceedings*, LNCS sublibrary: Image processing, computer vision, pattern recognition, and graphics, pages 36–47. Springer Berlin Heidelberg, 2013. ISBN 9783642382673. 42

P. W. Gingell, S. C. Chapman, R. O. Dendy, and C. S. Brady. Transport and evolution of ion gyro-scale plasma blobs in perpendicular magnetic fields. *Plasma Physics and Controlled Fusion*, 54(6):065005, 2012. 8

P. W. Gingell, S. C. Chapman, and R. O. Dendy. Plasma heating by ion gyro-scale blobs in the kinetic and fluid regimes. *Plasma Physics and Controlled Fusion*, 55: 055010, 2013. 8

P. W. Gingell, S. C. Chapman, and R. O. Dendy. Plasma blob formation by ion kinetic KelvinHelmholtz and interchange instabilities. *Plasma Physics and Controlled Fusion*, 56:035012, 2014. 8

B. E. Goldstein, E. J. Smith, A. Balogh, T. S. Horbury, M. L. Goldstein, and D. A. Roberts. Properties of magnetohydrodynamic turbulence in the solar wind as observed by Ulysses at high heliographic latitutes. *Geophysical Research Letters*, 22(23):3393–3396, 1995. 23, 82

R. J. Goldston and P. H. Rutherford. *Introduction to Plasma Physics.* CRC Press, 1995. ISBN 9781439822074. 43

W. Gropp, E. Lusk, and A. Skjellum. *Using MPI: Portable Parallel Programming with the Message-Passing Interface.* Scientific and Engineering Computation. MIT Press, 2014. ISBN 9780262326612. 33

D. A. Gurnett, E. Marsch, W. Pilipp, R. Schwenn, and H. Rosenbauer. Ion acoustic waves and related plasma observations in the solar wind. *Journal of Geophysical Research*, 84(A5):2029–2038, 1979. 26, 82

R. Hatzky, A. Ko, and A. Mishchenko. Electromagnetic gyrokinetic PIC simulation with an adjustable control variates method. *Journal of Computational Physics*, 225:568–590, 2007. 6

W. W. Heidbrink, M. E. Austin, R. K. Fisher, M. Garca-Muoz, G. Matsunaga, G. R. McKee, R. A. Moyer, C. M. Muscatello, M. Okabayashi, D. C. Pace, K. Shinohara, W. M. Solomon, E. J. Strait, M. A. Van Zeeland, and Y. B. Zhu. Characterization of off-axis fishbones. *Plasma Physics and Controlled Fusion*, 53(8):085028, 2011. 15, 54

W.W. Heidbrink and G. J. Sadler. The behaviour of fast ions in tokamak experiments. *Nuclear Fusion*, 34(4):535, 1994. 14, 53, 63

B. Hnat, S. C. Chapman, G. Rowlands, N. W. Watkins, and W. M. Farrell. Finite size scaling in the solar wind magnetic field energy density as seen by WIND. *Geophysical research Letters*, 29(10):86, 2002. 24, 25, 82, 101

B. Hnat, S. C. Chapman, and G. Rowlands. Intermittency, scaling, and the Fokker-Planck approach to fluctuations of the solar wind bulk plasma parameters as seen by the WIND spacecraft. *Physical Review E*, 67(5):056404, May 2003. ISSN 1063-651X. 24, 25, 83, 101

B. Hnat, S. C. Chapman, K. Kiyani, G. Rowlands, and N. W. Watkins. On the fractal nature of the magnetic field energy density in the solar wind. *Geophysical Research Letters*, 34(15):L15108, Aug 2007. 24, 101

R. W. Hockney and J. W. Eastwood. *Computer Simulation Using Particles*. Adam Hilger, Bristol and New York, 1989. 37, 38, 39, 67, 116

C. Holland, G. R. Tynan, P. H. Diamond, R. A. Moyer, and M. J. Burin. Evidence for Reynolds-stress driven shear flows using bispectral analysis: theory and experiment. *Plasma Physics and Controlled Fusion*, 44(5A):A453, 2002. 63

M. W. Hopcroft and S. C. Chapman. 2D hybrid simulations of the solar wind interaction with a small scale comet in high Mach number flows. *Geophysical Research Letters*, 28(6):1115–1118, 2001. 8

T. S. Horbury and A. Balogh. Structure function measurements of the intermittent MHD turbulent cascade. *Nonlinear Processes in Geophysics*, 4:185–199, 1997. 25

T. S. Horbury, A. Balogh, R. J. Forsyth, and E. J. Smith. The rate of turbulent evolution over the Sun's poles. *Astronomy and Astrophysics*, 316:333–341, 1996. 23

T S Horbury, M a Forman, and S Oughton. Spacecraft observations of solar wind turbulence: an overview. *Plasma Physics and Controlled Fusion*, 47:B703–B717, 2005. ISSN 0741-3335. 24, 83

A. J. Hundhausen, J. R. Asbridge, S. J. Bame, and I. B. Strong. Vela Satellite Observations of Solar Wind Ions. *Journal of Geophysical Research*, 72(7):1979, 1967. 26, 82, 88

M. Ichimura, H. Higaki, S. Kakimoto, Y. Yamaguchi, K. Nemoto, M. Katano, M. Ishikawa, S. Moriyama, and T. Suzuki. Observation of spontaneously excited waves in the ion cyclotron frequency range on JT-60U. *Nuclear Fusion*, 48 (3):035012, 2008. 15, 54

H. Karimabadi, V. Roytershteyn, M. Wan, W. H. Matthaeus, W. Daughton, P. Wu, M. Shay, B. Loring, J. Borovsky, E. Leonardis, S. C. Chapman, and T. K. M. Nakamura. Coherent structures, intermittent turbulence, and dissipation in high-temperature plasmas. *Physics of Plasmas*, 20(1):012303, 2013. ISSN 1070664X. 94

Y. C. Kim, J. M. Beall, E. J. Powers, and R. W. Miksad. Bispectrum and nonlinear wave coupling. *Physics of Fluids (1958-1988)*, 23(2):258–263, 1980. 63

K. Kiyani, S. C. Chapman, B. Hnat, and R. M. Nicol. Self-Similar Signature of the Active Solar Corona within the Inertial Range of Solar-Wind Turbulence. *Physical Review Letters*, 98(21):211101, May 2007. 24, 101

D. Koga, A. C.-L. Chian, R. A. Miranda, and E. L. Rempel. Intermittent nature of solar wind turbulence near the Earth's bow shock: Phase coherence and non-Gaussianity. *Physical Review E - Statistical, Nonlinear, and Soft Matter Physics*, 75(4):046401, 2007. 25

R. H. Kraichnan. Inertial-Range Spectrum of Hydromagnetic Turbulence. *Physics of Fluids*, 8:1385, 1965. 25

D. Krauss-Varban and N. Omidi. Large-scale hybrid simulations of the magnetotail during reconnection. *Geophysical Research Letters*, 22(23):3271–3274, 1995. 8

E. Leonardis, S. C. Chapman, W. Daughton, V. Roytershteyn, and H. Karimabadi. Identification of Intermittent Multifractal Turbulence in Fully Kinetic Simulations of Magnetic Reconnection. *Physical Review Letters*, 110(20):205002, May 2013. 24, 101

P. C. Liewer, M. Velli, and B. E. Goldstein. Alfven wave propagation and ion cyclotron interactions in the expanding solar wind : One-dimensional hybrid simulations. *Journal of Geophysical Research*, 106(A12):261–281, 2001. 8, 83

Y. Lin, X. Y. Wang, L. Chen, X. Lu, and W. Kong. An improved gyrokinetic electron and fully kinetic ion particle simulation scheme: benchmark with a linear tearing mode. *Plasma Physics and Controlled Fusion*, 53:054013, 2011. 7

Y. G. Maneva, A. F. Viñas, and L. Ofman. Turbulent heating and acceleration of He ++ ions by spectra of Alfvén-cyclotron waves in the expanding solar wind: 1.5-D hybrid simulations. *Journal of Geophysical Research: Space Physics*, 118 (6):2842–2853, Jun 2013. ISSN 21699380. 8, 83, 84, 85, 86, 87, 106, 110, 111

A. Mankofsky, R. N. Sudan, and J. Denavit. Hybrid Simulation of Ion Beams in Background Plasma. *Journal of Computational Physics*, 70:89–116, 1987. 8

E. Marsch. Kinetic Physics of the Solar Corona and Solar Wind. *Living Reviews in Solar Physics*, 3:1, 2006. 19, 26, 30, 82, 88

E. Marsch and C.-Y. Tu. On the Radial Evolution of MHD Turbulence in the Inner Heliosphere. *Journal of Geophysical Research*, 95(89):8211–8229, 1990. 23, 82

E. Marsch and C.-Y. Tu. Intermittency, non-Gaussian statistics and fractal scaling of MHD fluctuations in the solar wind. *Nonlinear Processes in Geophysics*, 4: 101–124, 1997. 25

E. Marsch, K.-H. Muhlhauser, R. Schwenn, H. Rosenbauer, and F. M. Neubauer. Solar Wind Helium Ions : Observations of the Helios Solar Probes Between 0.3 and 1 AU. *Journal of Geophysical Research*, 87(1):35–51, 1982a. 26, 29, 30, 82, 84, 88, 96, 105, 110, 115

E. Marsch, K.-H. Muhlhauser, R. Schwenn, H. Rosenbauer, W. Pilipp, and F. M. Neubauer. Solar Wind Protons: Three-Dimensional Velocity Distributions and Derived Plasma Parameters Measured Between 0.3 and 1 AU. *Journal of Geophysical Research*, 87(1):52–72, 1982b. 26, 28, 30, 82, 88, 105, 110, 115

B. A. Maruca. *Instability-Driven Limits on Ion Temperature Anisotropy in the Solar Wind : Observations and Linear Vlasov Theory.* PhD, Harvard University, 2012. 30, 105, 110, 115

B. A. Maruca, J. C. Kasper, and S. P. Gary. Instability-Driven Limits on Helium Temperature Anisotropy in the Solar Wind: Observations and Linear Vlasov Analysis. *The Astrophysical Journal*, 748(2):137, Apr 2012. ISSN 0004-637X. 83, 96, 105, 110

L. Matteini, S. Landi, M. Velli, and P. Hellinger. Kinetics of parametric instabilities of Alfvén waves: Evolution of ion distribution functions. *Journal of Geophysical Research*, 115(A9):A09106, Sep 2010. ISSN 0148-0227. 83, 88, 99

L. Matteini, P. Hellinger, S. Landi, P. M. Trávníček, and M. Velli. Ion Kinetics in the Solar Wind: Coupling Global Expansion to Local Microphysics. *Space Science Reviews*, 172(1-4):373–396, Apr 2011. ISSN 0038-6308. 8, 30, 83, 99

H. Matthaeus and M. L. Goldstein. Low-Frequency 1/f Noise in the Interplanetary Magnetic Field. *Physical Review Letters*, 57(4):495, 1986. 23, 82

K. G. Mcclements and R. O. Dendy. Ion cyclotron harmonic wave generation by ring protons in space plasmas. *Journal of Geophysical Research*, 98:11689, 1993. 18

K. G. McClements, R. O. Dendy, C. N. Lashmore-Davies, G. A. Cottrell, S. Cauffman, and R. Majeski. Interpretation of ion cyclotron emission from sub-Alfvénic fusion products in the Tokamak Fusion Test Reactor. *Physics of Plasmas*, 3(2): 543–553, 1996. 15, 54, 55, 57, 58, 63, 66, 70, 80

K. G. McClements, C. Hunt, R. O. Dendy, and G. A. Cottrell. Ion cyclotron emission from JET D-T plasmas. *Phys. Rev. Lett.*, 82:2099–2102, Mar 1999. 15, 53, 63, 70, 80, 108

K. G. McClements, R. O. Dendy, L. Carbajal, S. C. Chapman, J. W. S. Cook, R. D'Inca, R. W. Harvey, W. W. Heidbrink, and S. D Pinches. Fast particle-driven ion cyclotron emission (ICE) in tokamak plasmas and the case for an ICE diagnostic in ITER. *25th IAEA Fusion Energy Conference*, (TH/P3-28), 2014. 15, 54

K. G. McClements, R. D'Inca, R. O. Dendy, L. Carbajal, S. C. Chapman, J. W. S. Cook, R. W. Harvey, W. W. Heidbrink, and S. D. Pinches. Fast particle-driven ion

cyclotron emission (ICE) in tokamak plasmas and the case for an ICE diagnostic in ITER. *Nuclear Fusion*, 55:043013, 2015. 14, 15, 53, 54, 109

D. J. McComas, H. A. Elliot, N. A. Schwadron, J. T. Gosling, R. M. Skoug, and B. E Goldstein. The three-dimensional solar wind around solar maximum. *Geophysical Research Letters*, 30(10):24, 2003. 20, 114

J. A. Merrifield, W. Müller, S. C. Chapman, and R. O. Dendy. The scaling properties of dissipation in incompressible isotropic three-dimensional magnetohydrodynamic turbulence. *Physics of Plasmas*, 12:022301, 2005. 25

J. A. Merrifield, T. D. Arber, S. C. Chapman, and R. O. Dendy. The scaling properties of two-dimensional compressible magnetohydrodynamic turbulence. *Physics of Plasmas*, 13:012305, 2006. 25

J. A. Merrifield, S. C. Chapman, and R. O. Dendy. Intermittency, dissipation, and scaling in two-dimensional magnetohydrodynamic turbulence. *Physics of Plasmas*, 14:012301, 2007. 25

A. Mishchenko, A. Könies, T. Fehér, R. Kleiber, M. Borchardt, J. Riemann, R. Hatzky, J. Geiger, and Yu. Turkin. Global hybrid-gyrokinetic simulations of fast-particle effects on Alfvén Eigenmodes in stellarators. *Nuclear Fusion*, 54: 104003, 2014. 7

R. A. Moyer, G. R. Tynan, C. Holland, and M. J. Burin. Increased nonlinear coupling between turbulence and low-frequency fluctuations at the L-H transition. *Phys. Rev. Lett.*, 87:135001, Sep 2001. 63

J. Müller, S. Simon, U. Motschmann, J. Schüle, K.-H. Glassmeier, and G. J. Pringle. A.I.K.E.F.: Adaptive hybrid model for space plasma simulations. *Computer Physics Communications*, 182(4):946 – 966, 2011. 42

M. S. Nakamura and M. Fujimoto. A three-dimensional hybrid simulation of magnetic reconnection. *Geophysical Research Letters*, 25(15):2917–2920, 1998. 8

Y. Nariyuki, T. Hada, and K. Tsubouchi. Heating and acceleration of ions in nonresonant Alfvenic turbulence. *Physics of Plasmas*, 17(7):072301, 2010. ISSN 1070664X. 83

Y. Nariyuki, T. Umeda, T. K. Suzuki, and T. Hada. Ion acceleration by parallel propagating nonlinear Alfvén wave packets in a radially expanding plasma. *Nonlinear Processes in Geophysics*, 21(1):339–346, Feb 2014. ISSN 1607-7946. 83

R. Nazikian, G. J. Kramer, C. Z. Cheng, N. N. Gorelenkov, H. L. Berk, and S. E. Sharapov. New interpretation of alpha-particle-driven instabilities in deuterium-tritium experiments on the Tokamak Fusion Test Reactor. *Physical review letters*, 91(Sep):125003, 2003. 13

R. M. Nicol, S. C. Chapman, and R. O. Dendy. QUANTIFYING THE ANISOTROPY AND SOLAR CYCLE DEPENDENCE OF 1/ f SOLAR WIND FLUCTUATIONS OBSERVED BY ADVANCED COMPOSITION EX-PLORER. *The Astrophysical Journal*, 703(2):2138–2151, Oct 2009. ISSN 0004-637X. 25, 83, 101

L. Ofman. Three-fluid model of the heating and acceleration of the fast solar wind. *Journal of Geophysical Research*, 109(A7):A07102, 2004. ISSN 0148-0227. 83

L. Ofman. Wave Modeling of the Solar Wind. *Living Reviews in Solar Physics*, 7: 4, 2010. 7

K. T. Osman, W. H. Matthaeus, A. Greco, and S. Servidio. Evidence for Inhomo-geneous Heating in the Solar Wind. *The Astrophysical Journal*, 727(1):L11, Jan 2011. ISSN 2041-8205. 25, 82

K. T. Osman, W. H. Matthaeus, M. Wan, and A. F. Rappazzo. Intermittency and Local Heating in the Solar Wind. *Physical Review Letters*, 108(26):261102, Jun 2012. ISSN 0031-9007. 24, 83

K. T. Osman, K. H. Kiyani, S. C. Chapman, and B. Hnat. Anisotropic Intermittency of Magnetohydrodynamic Turbulence. *The Astrophysical Journal Letters*, 783(2): L27, Mar 2014. ISSN 2041-8205. 25, 83

D. Perrone, F. Valentini, S. Servidio, S. Dalena, and P. Veltri. Vlasov Simulations of Multi-Ion Plasma Turbulence in the Solar Wind. *The Astrophysical Journal*, 762(2):99, Jan 2013. ISSN 0004-637X. 83

W.H. Press. *Numerical Recipes 3rd Edition: The Art of Scientific Computing*. Cam-bridge University Press, 2007. ISBN 9780521880688. 39

P. L. Pritchett. Particle-in-Cell Simulations of Magnetosphere Electrodynamics. *IEEE Transactions on plasma science*, 28(6):1976–1990, 2000. 39, 85

V. L. Rekaa, S. C. Chapman, and R. O. Dendy. Ion pre-acceleration in fully self-consistent particle-in-cell simulations of supercritical perpendicular reform-ing shocks in multiple ion species plasmas. *The Astrophysical Journal*, 791(1):26, 2014. 18

C. Salem, a. Mangeney, S. D. Bale, and P. Veltri. Solar Wind Magnetohydrodynamics Turbulence: Anomalous Scaling and Role of Intermittency. *The Astrophysical Journal*, 702:537–553, 2009. 23, 26, 115

S. Sato, M. Ichimura, Y. Yamaguchi, M. Katano, Y. Imai, T. Murakami, Y. Miyake, T. Yokoyama, S. Moriyama, T. Kobayashi, A. Kojima, K. Shinohara, Y. Sakamoto, T. Watanabe, H. Hojo, and T. Imai. Observation of ion cyclotron emission owing to dd fusion product h ions in JT-60U. *Plasma and fusion research*, 5:S2067, 2010. 15, 54

P. Schild, G. A. Cottrell, and R. O. Dendy. Sawtooth oscillations in ion cyclotron emission from JET. *Nuclear Fusion*, 29(5):834, 1989. 14, 15, 53, 54, 63

N. A. Schwadron and D. J. McComas. Solar wind scaling law. *The Astrophysical Journal*, 599:1395–1403, 2003. 20

S E Sharapov, L.-G. Eriksson, A Fasoli, G Gorini, J. Kallne, V G Kiptily, A A Korotkov, A Murari, S D Pinches, D S Testa, and P R Thomas. CHAPTER 5 BURNING PLASMA STUDIES AT JET. *Fusion Science and technology*, 54(4): 989, 2008. 75, 80

S.E. Sharapov, B. Alper, H.L. Berk, D.N. Borba, B.N. Breizman, C.D. Challis, I.G.J. Classen, E.M. Edlund, J. Eriksson, A. Fasoli, E.D. Fredrickson, G.Y. Fu, M. Garcia-Munoz, T. Gassner, K. Ghantous, V. Goloborodko, N.N. Gorelenkov, M.P. Gryaznevich, S. Hacquin, W.W. Heidbrink, C. Hellesen, V.G. Kiptily, G.J. Kramer, P. Lauber, M.K. Lilley, M. Lisak, F. Nabais, R. Nazikian, R. Nyqvist, M. Osakabe, C. Perez von Thun, S.D. Pinches, M. Podesta, M. Porkolab, K. Shinohara, K. Schoepf, Y. Todo, K. Toi, M.A. Van Zeeland, I. Voitsekhovich, R.B. White, and V. Yavorskij. Energetic particle instabilities in fusion plasmas. *Nuclear Fusion*, 53(10):104022, Oct 2013. 12, 13, 113

J. E. Sharer and A. W. Trivelpiece. Cyclotron wave instabilities in a plasma. *Physics of Fluids*, 10:591, 1967. 45

B. U. Ö. Sonnerup. Large Amplitude Whistler Waves in a Hot Collision-Free Plasma. *Physics of Fluids*, 10(2):462, 1967. ISSN 00319171. 85, 86

L. Sorriso-Valvo, V. Carbone, P. Giuliani, P. Veltri, R. Bruno, V. Antoni, and E. Martines. Intermittency in plasma turbulence. *Planetary and Space Science*, 49:1193–1200, 2001. 27, 115

K. Stasiewicz, P. K. Shukla, G. Gustafsson, S. Buchert, B. Lavraud, B. Thidé, and Z. Klos. Slow magnetosonic solitons detected by the cluster spacecraft. *Physical review letters*, 90(8):085002, 2003. 25

T. H. Stix. *Waves in Plasmas.* American Inst. of Physics, 1992. ISBN 9780883188590. 43

P. Subedi, R. Chhiber, J. A. Tessein, M. Wan, and W. H. Matthaeus. Generating Synthetic Magnetic Field Intermittency Using a Minimal Multiscale Lagrangian Mapping Approach. *The Astrophysical Journal*, 796(2):97, Nov 2014. ISSN 1538-4357. 25, 101, 111

R. D. Sydora. Low-noise electromagnetic and relativistic particle-in-cell plasma simulation models. *Journal of Computational and Applied Mathematics*, 109(1-2):243–259, 1999. 69

G. I. Taylor. The Spectrum of Turbulence. *Proceedings of the Royal Society A: Mathematical, Physical and Engineering Sciences*, 164(919):476–490, Feb 1938. ISSN 1364-5021. 83

T. Terasawa, M. Hoshino, J.-I. Sakai, and T. Hada. Decay Instability of Finite-Amplitude Circular Polarized Alfven Waves: A Numerical Simulation of Stimulated Brillouin Scattering. *Journal of Geophysical Research*, 91(A4):4171–4187, 1986. 41

P. Thomas, P. Andrew, B. Balet, D. Bartlett, J. Bull, B. de Esch, a. Gibson, C. Gowers, H. Guo, G. Huysmans, T. Jones, M. Keilhacker, R. Koenig, M. Lennholm, P. Lomas, a. Maas, F. Marcus, F. Nave, V. Parail, F. Rimini, J. Strachan, K-D. Zastrow, and N. Zornig. Observation of Alpha Heating in JET DT Plasmas. *Physical Review Letters*, 80(25):5548–5551, Jun 1998. 13, 75, 77

P. Thomas, C. Giroud, P. Lomas, P. Stubberfield, S. Sharapov, D. Testa, and DTE1 Experimental Team. HEATING OF THERMAL IONS BY ALPHAS IN THE JET DT EXPERIMENT. *28th EPS Conference on Controlled Fusion and Plasma Physics*, 25A(Jun):929–932, 2001. 13, 75, 77

V A Thomas, D Winske, and N Omidi. Re-forming Supercritical Quasi-Parallel Shocks 1. One- and Two-Dimensional Simulations. *Journal of Geophysical Research*, 95(A11):18809, 1990. 8

C. Torrence and G. P. Compo. A Practical Guide to Wavelet Analysis. *Bulleting of the American Meteorological Society*, 79(1):61, 1998. 26, 101

C.-Y. Tu, C. Zhou, E. Marsch, L.-D. Xia, L. Zhao, J.-X. Wang, K. Wilhelm, Chuan-yi Tu, Cheng Zhou, Eckart Marsch, and Li-dong Xia. Solar Wind Origin in Coronal Funnels. *Science*, 308(5721):519–523, 2015. 20

F. Valentini and P. Veltri. Electrostatic Short-Scale Termination of Solar-Wind Turbulence. *Physical Review Letters*, 102(22):225001, Jun 2009. ISSN 0031-9007. 83, 88

F. Valentini, P. Veltri, F. Califano, and A. Mangeney. Cross-Scale Effects in Solar-Wind Turbulence. *Physical Review Letters*, 101(2):025006, Jul 2008. ISSN 0031-9007. 83

P. Veltri. MHD turbulence in the solar wind: self-similarity, intermittency and coherent structures. *Plasma Physics and Controlled Fusion*, 41:A787, 1999. 83

A. Verdini, R. Grappin, R. Pinto, and M. Velli. Spectrum in the Solar Wind Magnetic Field. *The Astrophysical Journal*, 750:L33, 2012. ISSN 2041-8205. 23, 82

G. Watson and W. W. Heidbrink. Density interferometer using the fast Alfvén wave. *Review of Scientific Instruments*, 74(3):1605, 2003. ISSN 00346748. 15, 54

D. Winske and M. M. Leroy. Diffusive ions produced by electromagnetic ion beam instabilties. *Journal of Geophysical Research*, 89(A5):2673–2688, 1984. 8, 46

D. Winske and N. Omidi. Electromagnetic Ion/Ion Cyclotron Instability: Theory and Simulations. *Journal of Geophysical Research*, 97(A10):14779, 1992. 8

D. Winske and N. Omidi. Hybrid codes: Methods and applications. In H. Matsumoto and Y Omura, editors, *Computer Space Plasma Physics: Simulations and Software*, pages 103–160. Terra, Tokyo, 1993. 6, 35, 39, 46, 47, 50, 100, 117

D. Winske and N. Omidi. A nonspecialist's guide to kinetic simulations of space plasmas. *Journal of Geophysical Research: Space Physics*, 101(A8):17287–17303, 1996. 8

D. Winske, L. Yin, N. Omidi, H. Karimabadi, and K. Quest. Hybrid Simulation Codes: Past, Present and Future – A Tutorial. In Jörg Büchner, Manfred Scholer, and Christian T. Dum, editors, *Space Plasma Simulation*, volume 615 of *Lecture Notes in Physics*, pages 136–165. Springer Berlin Heidelberg, 2003. 6, 41

P. Wu, S. Perri, K. Osman, M. Wan, W. H. Matthaeus, M. a. Shay, M. L. Goldstein, H. Karimabadi, and S. C. Chapman. Intermittent Heating in Solar Wind and

Kinetic Simulations. *The Astrophysical Journal Letters*, 763(2):L30, Feb 2013. ISSN 2041-8205. 24, 25, 83, 101

T. Yamada, S.-I. Itoh, T. Maruta, N. Kasuya, Y. Nagashima, S. Shinohara, K. Terasaka, M. Yagi, S. Inagaki, Y. Kawai, A. Fujisawa, and K. Itoh. Anatomy of plasma turbulence. *Nat. Phys.*, 4:721, 2008. 63

K. S. Yee. Numerical Solution of Initial Boundary Value Problems Involving Maxwell's Equations in Isotropic Media. *IEEE Trans. Antennas Propag.*, 14(8): 302–307, 1966. 36

L. Yin and D. Winske. Plasma pressure tensor effects on reconnection : Hybrid and Hall- magnetohydrodynamics simulations. *Physics of Plasmas*, 10(5):1595, 2012. 8